Buffer-gas cooling and magnetic trapping of CrH and MnH molecules

D i s s e r t a t i o n

zur Erlangung des akademischen Grades

d o c t o r   r e r u m   n a t u r a l i u m

(Dr. rer. nat.)

im Fach Physik

eingereicht an der

Mathematisch-Naturwissenschaftlichen Fakultät I

der Humboldt-Universität zu Berlin

von

Dipl.-Phys. Michael Stoll
geboren am 26.12.1974 in Weiden i.d.Opf.

Präsident der Humboldt-Universität zu Berlin
Prof. Dr. Christoph Markschies

Dekan der Mathematisch-Naturwissenschaftlichen Fakultät I
Prof. Dr. Lutz-Helmut Schön

Gutachter: 1. Prof. Dr. Gerard J.M. Meijer
                                       2. Prof. Achim Peters, PhD
                                       3. Prof. John M. Doyle, PhD

Tag der mündlichen Prüfung: 24.6.2008

Buffer-gas cooling and magnetic trapping of CrH and MnH molecules

Dissertation

eingereicht von

Michael Stoll

Mai 2008

Thesis advisor: Prof. Achim Peters, PhD
Humboldt-Universität zu Berlin
Co-advisor: Prof. Dr. Gerard J.M. Meijer
Fritz-Haber-Institut
der Max-Planck-Gesellschaft, Berlin

Manuscript referees: Prof. Achim Peters, PhD
Prof. Dr. Gerard J.M. Meijer

Prof. John M. Doyle, PhD
Harvard University, Cambridge, USA

Für meine Eltern, meine Frau Mona und unseren Sohn Oskar.

Danksagung

Zu diesem Projekt haben außer mir auch sehr viele andere Menschen einen entscheidenden Beitrag geleistet, denen ich auf diesem Weg gerne danken möchte.

Zunächst einmal danke ich Achim Peters und Gerard Meijer dafür, daß Sie mir die Chance gegeben haben, an einem so spannenden und abwechslungsreichen Projekt mitzuwirken. Ihre Gedanken und Vorschläge ergaben immer wichtige Impulse in allen Stadien des Experiments. Darüber hinaus möchte ich mich bei Beiden für die unglaublich tolle und offene Arbeitsatmosphäre innerhalb der Gruppe(n) bedanken, die ich sehr geschätzt habe.

Besonderer Dank gilt Joost Bakker, mit dem ich das Vergnügen hatte, in der ersten Hälfte des Projekts zusammenarbeiten zu dürfen. Er hat mir beigebracht ein besserer Physiker zu werden und Bruce Springsteen wirklich wertschätzen zu lernen. Ich schulde ihm viel Dank, gerade hinsichtlich der vielen Zeit, die er immer bereit war für mich zu opfern.

I also like to thank John Doyle for his tremendous support. The time he spent in Berlin was a great pleasure and the fruitful discussions with him and his co-workers Wes Campbell, Scott Nguyen, Nathaniel Brahms and Rob deCarvalho have contributed a lot for becoming acquainted with the difficulties and the possibilities of this experiment.

For teaching me molecular spectroscopy and his collaboration is something I would like to thank Tim Steimle for. I felt more than welcome in his group and the work that was done by him and his co-workers Jamie Gengler and Jinhai Chen added an important part to my project.

Ich möchte auch meinen beiden Vorgängern Dennis Weise und Oliver Vogelsang für die Zeit danken, die sie am Anfang des Projekts investiert haben, um Joost und mich mit dem Versuchsaufbau vertraut zu machen.

Evgeny Kovalchuk war eine große Hilfe beim Finetuning des Diodenlasers.

Besonderer Dank gilt meinen Eltern, die mich während meiner gesamten Studienzeit unterstützt haben. Ohne ihre Hilfe hätte ich es niemals geschafft so viel in meinem Leben zu erreichen. Dies gilt insbesondere auch für meine Frau Mona, deren unermüdliche Unterstützung und Liebe gerade in schwierigen Zeiten des Projekts besonders wichtig war.

Michael Stoll

Contents

Chapter 1

Introduction

1.1 Cold molecules

Over the last centuries, it has been realized that atoms and molecules are the building blocks of life and the world surrounding us. This awareness led to the development of molecular physics as one of the key research fields to investigate *e.g.* chemical interactions, the role of molecules in biological systems, and large scale astrophysical processes in the universe. To understand these often extremely complex mechanisms, it is crucial to have a complete picture of the inherent properties and interactions of the atoms and molecules involved. These properties can be precisely studied using gas-phase samples, since any interactions between the particles and their environment are then absent.

Room-temperature molecules and atoms in the gas-phase, however, move around with very high velocities on the order of a few 100 ms^{-1}. In a very simple picture, one can argue that if an object moves very fast, its details are not accessible and thus remain hidden. Likewise, objects that are slowed down can be studied in much higher detail. The equivalent to slowing down molecules and atoms is to cool them to a lower temperature. To translate this into physics terms, a higher measurement sensitivity can be achieved by increasing the interaction time of the particles with the probing system, for instance, with a laser beam.

The quality of a measurement can be even further increased by confining particles in a trapping field after cooling, allowing for the longest possible measurement times.

Since the development of laser cooling in the 1970s, the field of atomic and molecular physics has experienced a remarkable growth. Over the years, mature methods to manipulate the motional degrees of freedom have been developed which led to a large new field of research studying the rich physics of cold particle interactions. Among these phenomena, Bose-Einstein-Condensation (BEC) can be regarded as one of the milestones of this new field. Such a BEC can be formed when the wave functions of single particles start to overlap at decreasing temperatures and increasing phase-space densities. As a result, macroscopic signatures of quantum phenomena become visible, an effect that was first observed in 1995 by three independent research groups [1, 2, 3], and has been rewarded with the Nobel price in physics in 2001. Soon after this, further breakthroughs have been reached like the achievement of Fermi degeneracy in atomic vapors [4] or the realization of atom lasers [5,6,7,8].

For a long time, most of the work in this field was restricted to atoms only, since a general and efficient cooling mechanism, equivalent to laser cooling, was lacking for molecules. Since molecules have a more complex inner structure, closed transitions - a premise for laser cooling - are hard to find. However, it is exactly this complexity of molecules that offers the perspectives to study new and exciting effects that are much harder to address or are even absent in atoms [9, 10, 11]. As a consequence, studies of cold molecules have moved more and more into the focus of modern research, a trend which also led to the development of suitable cooling mechanisms. Some of the prospects that cold molecules offer shall be briefly depicted here.

High resolution spectroscopy

The resolution in a spectroscopic experiment can greatly benefit from the enhanced interaction times available in trapped molecule samples. While this is important for detailed studies into molecular structure, it is also promising for the use of cold molecules in metrology experiments. As an example, the large electric fields within a polar molecule provides an optimal environment to measure the possible electric dipole moment

of an electron (EDM), an effect which has been predicted in theoretical descriptions beyond the standard model of particle physics [12,13]. Cold molecules therefore can be used to test these new theories. The molecules YbF and PbO are particularly well suited for these studies [14,15]. Other questions of fundamental physics for which the use of cold molecules could be of importance include tests of the symmetrization postulate with homonuclear molecules [16], the time-dependence of fundamental constants [17] and the CP violation in chiral molecules [18].

Lifetime measurements of excited states

In addition to experiments regarding such fundamental questions, long storage times also offer the benefit of direct measurements of the lifetimes of long lived electronically or vibrationally excited states; so far, this has already been accomplished for OH and NH [19, 20]. Such measurements can have significant impact on astrophysical or atmospheric observations, since they can serve as benchmarks for theoretical models, as measurements of such important input parameters are scarce.

Degenerate molecular Bose and Fermi gases

In degenerate Bose and Fermi gases, a macroscopic part of the particle ensemble occupies the absolute quantum mechanical ground state. As mentioned above, such exotic states already have been prepared for many different atomic species. However, when going to molecules, which have an enhanced number of internal degrees of freedom, the resulting quantum gases are expected to show special properties as a consequence of the rich rotational and vibrational structure and non-spherical symmetry of the constituents. In late 2003, the first observation of a molecular BEC was reported by three groups [21, 22, 23]. One interesting property of molecular BECs arises from the interaction between the permanent electric dipole moments of the molecules, a property missing in atoms. Recently the magnetic dipole-dipole interaction has been observed, as it determines the macroscopic shape of a chromium BEC [24, 25].

5

Ultracold chemistry

Collisions at very low temperatures allow fundamental insight into many aspects of particle interactions, and interesting effects are predicted to occur for low collision energies. The elastic and inelastic collision cross sections, for example, show sharp resonances in this energy regime [26]. This might lead to the formation of unusual states when the colliding molecules begin to rotate after the collision event. As a consequence, the translational energy might be insufficient to overcome their van-der-Waals attraction, and the molecules stay bound together. If the collision energy can be controlled, like for example with the use of Stark decelerated molecular beams, the scattering properties of two species can be studied in unprecedented detail. In first experiments, the transition probabilities for inelastic scattering of Stark decelerated OH radicals with Xe atoms were successfully measured as a function of the collision energy [27]. Furthermore, cooling molecules to very low temperatures gives access to an exotic regime for chemical reactivity, governed by quantum tunnelling and resonances [28, 29]

Quantum computing

Much more than atoms, molecules provide the conditions needed to realize the complex entangled systems required for large scale quantum computing. Aligned molecular dipoles in a 1D array could for instance serve as qubits, which are coupled via the long-range electric dipole-dipole interaction, unique to molecules [30, 31, 32].

1.2 Production of cold molecules

Over the last decade several techniques to produce samples of cold molecules have been developed. Some of the most important and successful methods are described in the following sections.

1.2.1 Molecule formation from cold atoms

The difficulties in direct laser cooling of molecules can be circumvented if molecules can be formed by association of laser cooled cold atoms. For-

mation of molecules from atoms can be done by *photo-association*, where a photon is used to promote two adjacent atoms into a vibrationally excited state of a bound molecule. This method was first successfully developed for the production of homonuclear molecules [33, 34] and has later been extended to heteronuclear molecules like RbCs [35], NaCs [36] and KRb [37, 38]. Recently, the formation of LiCs molecules has been reported [39]. Molecules produced by this method are translationally cold, but in a high vibrationally excited state and, as a consequence, they have a rather limited lifetime. To obtain stable molecules, they have to be transferred into the vibrational ground state. This can be done using stimulated emission with a second photon, as has recently been demonstrated for photo-associated RbCs molecules [40].

A second method of producing cold molecules from cold atoms is given by magnetically tuning close to or through a *Feshbach resonance*. This is a scattering resonance where two (unbound) colliding atoms couple to a molecular bound state. Since the magnetic moments of the atomic and the molecular states are different, their energies can be matched by applying an external magnetic field. Molecules can be formed by either adiabatically tuning over the resonance, or by tuning close to the resonance. The latter method exploits the strongly enhanced three body recombination close to the resonance that can lead to molecule formation if the atom densities are sufficiently high. As mentioned above, this technique allowed for the first creation of molecular BECs from degenerate Fermi gases in 2003 [21, 22, 23]. Similar to the case of photo-associated molecules such samples are created in highly vibrationally excited states.

1.2.2 Direct cooling of molecules using beam techniques

Polar molecules can be efficiently slowed down with time-varying inhomogeneous electric fields in a Stark decelerator. After pre-cooling the molecules in a supersonic expansion, creating a molecular beam, the particles are already rather cold (a few Kelvins) in the moving frame of this beam. However, the molecular packets themselves travel with a speed of several hundreds of meters per second. These packets are then

entering the Stark decelerator which consists of an array of high-voltage electrodes. Molecules that possess an electric dipole moment and that are in the appropriate quantum state will exchange kinetic energy for Stark energy upon entering an electric field. When the electric field is quickly switched off before the molecules leave this field region, they will not regain the lost kinetic energy. In this way, the translational energy can be reduced at each electrode stage and the molecules can be brought to a standstill at the end of the decelerator.

This technique was first demonstrated in 1999 by decelerating a beam of metastable CO molecules in the low-field-seeking state [41]. In recent years, several other low-field seeking molecules have been decelerated, namely ammonia [42, 43], OH [44, 45], formaldehyde [46], metastable NH [47] and SO_2 [48]. Among these NH, OH and CO have subsequently been loaded into an electrostatic trap. Stark-decelerated ND_3 molecules have also been loaded both into an electrostatic ring as well as into the next generation of this device, which can be regarded as a *molecular synchrotron* [49, 50, 51]. In these machines, low-field seeking molecule packets revolve inside electrostatic hexapole electrodes bent into a ring.

In recent years, methods have been developed to extend this technique to high-field seeking molecules. However, since the highest fields are at the electrodes, this is much more difficult and involves alternate gradient focusing techniques. Using this technique, deceleration has been shown so far for CO [52], OH [53], and heavy polar molecules like YbF [54] and benzonitrile [55].

Velocity filtering of a molecular beam is a technique that has been developed in the Rempe group [56]. It relies on extracting low velocity polar molecules from the thermal Maxwell-Boltzmann distribution using a curved electrostatic guide. This is done directly after the nozzle of an effusive beam source, leading to guiding of a very small fraction of molecules that are already translationally cold. Using this technique, a number of molecules have been velocity-filtered, and filtered ammonia molecules have been successively confined in a two-dimensional trap [57].

1.2.3 Buffer-gas cooling

In the buffer-gas cooling technique, the species of interest is injected into a vapor of cryogenically cooled helium atoms for thermalization

via elastic collisions. The use of an inert noble gas in conjunction with cryogenic techniques offers several advantages. First, chemical reactions with the buffer-gas are strongly suppressed, so that buffer-gas loading should be applicable to a wide variety of different particles, including rather large molecules. In addition, the large cooling powers available in modern cryostats offer the perspective to achieve high initial particle numbers and densities of the injected species. However, if the cooling is to be combined with magnetic trapping of the (paramagnetic) species, the universality is limited due to inelastic collisions with the helium gas atoms that potentially transfer the molecules into untrappable states. Buffer-gas cooling in conjunction with magnetic trapping was the first method used to successfully cool and subsequently trap large samples of molecules in 1998 [58]. This technique is employed in the experiments described in this thesis and will be treated in detail in Chapter 2.

1.3 Traps

As mentioned previously, cooling of particles considerably enhances the resolution of a measurement. Confining them in a trapping field subsequent to cooling can enhance the quality of a measurement further, and it also allows for advanced manipulation of the trapped ensemble. Many different types of traps have been developed over the years; the most important ones for confinement of neutral atoms and molecules are briefly described here.

Trapping can be established in a field configuration, in which the individual particles lose kinetic and gain potential energy when they move away from the confinement center. Many traps for neutral particles exploit either the *Stark* or the *Zeeman effect*. In the first case, the electric field leads to a splitting of the energy levels via interaction of the field with the electric dipole moment of the particle, whereas a magnetic field leads to a similar splitting via interaction with the magnetic dipole moment.

For particles in states whose energy increases with increasing field strength, it is energetically favorable to be in a lower field region, and they are therefore driven to the field minima. These particles are referred to as *low-field seekers*, while particles in states whose energy decreases

with increasing field strength are attracted to higher field regions. These are referred to as *high-field seekers*.

1.3.1 Traps for low-field seekers

To trap molecules in low-field seeking states, a local field minimum is required. Such a minimum can be created by means of electrostatic or magnetostatic fields.

Electrostatic traps

As mentioned above, electrostatic traps exploit the interaction between the electric-dipole-moment and external electric fields, which induces a splitting of the energy levels; this effect is known as the *Stark effect*. The lack of such a dipole moment in electronic ground state atoms, however, restricts the applicability of this technique to polar molecules or atoms in highly polarizable Rydberg states.

Electrostatic trapping was first demonstrated for ammonia molecules in 2000 [42]. In more recent experiments, OH [45], metastable NH [47], as well as metastable CO molecules [59] have been electrostatically trapped. Trap depths obtained using this technique depend on the dipole moment of the particles, but typical values are on the order of 500 mK.

Magnetostatic traps

In analogy to electrostatic traps, magnetostatic traps confine *low-field seeking* particles in a local field minimum in space via the magnetic dipole interaction. Since all paramagnetic particles possess such magnetic dipole moments, this trapping method is suitable not only for paramagnetic molecules, but also for trapping of about 60 % of the atoms in the periodic table.

This method has been successfully applied to a broad range of atomic species like chromium [60], europium [61], molybdenum [62] and several other rare earth atoms [63]. Moreover, application of this technique resulted in the first trapping of a molecule with reasonable size samples (CaH) [58]. All trapping experiments described in this thesis were conducted in a magnetostatic trap; its details are elaborated upon in Section

2.3.

Magnetoelectrostatic traps

Particles can also be confined using a combination of static magnetic and static electric fields. This recently has been demonstrated on ground state OH molecules [64]. Magnetic trapping of cold polar molecules under adjustable electric fields may enable study of low energy dipolar interactions.

1.3.2 Traps for high-field seekers

To trap particles in high-field seeking states, a local field maximum is necessary. However, Earnshaw's theorem states that such a maximum in free space cannot be produced by static electromagnetic fields [65,66]. Using electrodynamic fields, this constraint can be circumvented, and traps for high-field seekers can be realized. One of the big advantages of trapping particles in such states is that the absolute ground state - which is typically high-field seeking - can be confined. This implies that decay to lower lying states, which can lead to trap loss in static traps, can be prevented.

Optical dipole traps

Any polarizable particle can, in principle, be confined through the ac Stark effect. This confinement relies on dipole moments that are induced in the particles via the polarization of their charge distribution by means of strong electric field amplitudes in intense laser fields. To avoid optical excitation of the atoms or molecules, the light is tuned far away from any optical resonances. The induced dipoles can then in return interact with the electric fields of the laser via the Stark effect. This effect is used in optical dipole traps that have found widespread application in ultracold atom experiments [67,68]. This technique has also been successfully used to trap cesium molecules [69]. Unfortunately most particles are difficult to polarize and as a consequence typical trap depths produced by means of focusing state-of-the-art CO_2 laser beams are only on the order of 1 mK [68]. Another constraint of these types of traps is that they only offer

11

a very small trapping volume of a few hundred μm, therefore confining only a small number of atoms or molecules.

Microwave traps

Similar to optical dipole traps, microwave traps use ac coupling of permanent or induced dipole moments to a standing-wave electromagnetic field in a cavity for confinement. Using this technique, trapping can be established both via electric and magnetic dipole forces. Microwave storage was first demonstrated for cesium atoms, where a comparatively low trap depth of 0.1 mK was achieved via coupling of the induced electric dipole moment to the ac electric field [70]. However, by using polar molecules, significantly higher trap depths exceeding 1 K should in principle be obtainable [71].

AC electric traps

In ac electric traps, the electric field produced by several electrodes, has a saddle-point shape. In other words, it has a field-maximum in one direction and a field-minimum in another direction which results in a focusing and de-focusing force for high-field seeking molecules. In a second voltage configuration of the electrodes, a different saddle-point geometry with reversed maxima and minima can be created. By switching between these two fields with an appropriate frequency, a net focusing force in three-dimensional space can be generated.

For ground-state ammonia molecules, ac electric traps with a depth of several millikelvins have been demonstrated [72, 73, 74]. In addition to particles with permanent dipole moments, any ground-state atom or nonpolar molecule can be confined in an ac electric trap via an induced dipole moment, by means of applying external electric fields. In this way, trapping of rubidium atoms in a macroscopic ac electric trap with a depth of 10 μK was recently demonstrated [75]. In addition, ground-state Sr atoms have been trapped using a microstructured ac trap on a chip [76].

1.4 This thesis

This thesis presents the investigation into the general applicability of buffer-gas loading and subsequent magnetic trapping to a broad range of molecule species. Cooling and storing of atoms and molecules via buffer-gas loading of a magnetic trap was first suggested by Doyle and co-workers [77]. Since then, it has been successfully applied to a broad range of high spin atomic species like chromium [60], molybdenum [62], europium [61], and several other rare earth atoms [63]. In these experiments, typical densities on the order of $\sim 10^{11}\,\mathrm{cm}^{-3}$ and storage times of tens of seconds at temperatures of a few hundred mK were observed. Such large densities serve as an ideal starting point for evaporative cooling, a method that has been successfully applied to atomic chromium [78], molybdenum [62] and metastable helium [79].

The technique has been extended to molecules like CaH [58] and NH as well as ND [80], which have all been trapped at several hundred mK with densities of $\sim 10^8\,\mathrm{cm}^{-3}$, allowing for a direct measurement of the lifetime of the first vibrationally excited state of NH [20]. An attempt was made to buffer-gas cool and trap VO molecules, but confinement of this species was prevented for unknown reasons [81]. By including a technique to rapidly remove the buffer-gas after cooling, longer lifetimes can be obtained for the confined species, as results from atomic chromium indicate [82].

Unfortunately, the promise of general applicability of this trapping technique to all paramagnetic species seems to be severely restricted due to a large trap loss channel given by inelastic collisions with the helium buffer-gas atoms. Such collisions potentially transform molecules from low- to high-field-seeking states, and thus can lead to severe limitations on the achievable trapping times. This is, of course, a big problem, since a large-density helium gas is required for cooling the initially hot molecules to temperatures below the trap depth. Investigating these processes and their impact on the possibility to trap a broader range of molecules using this technique is the main goal of this work.

Although spin-flip collisions seem to constitute a major limitation for this technique, the increased interest in the field of cold molecules also led to an increase in theoretical work regarding these processes at conditions typical for cryogenic buffer-gas cooling and subsequent mag-

netic trapping [83, 84, 85]. Even though this theoretical work, so far, only addressed low-spin ground state molecules, a deeper insight into the molecular characteristics leading to unfavorable collision properties has been established. Using this knowledge, we wanted to investigate the potential to magnetically trap high-spin ground state molecules using a buffer-gas loading approach. To do this, we study the effects of inelastic collisions on the dynamics of the particles as they diffuse through a cold helium gas in the presence of a magnetic trapping field.

The two molecules CrH and MnH have been identified as ideal candidate systems for this. Due to their high-spin ground state, they both possess large magnetic moments, which make them amenable for magnetic trapping at our available magnetic field strengths. At the same time, their relatively small spin-spin and spin-rotation coupling constants combined with a large rotational constant indicate that they might possess favorable collision properties allowing for long trapping times. If buffer-gas cooling and subsequent magnetic trapping is to be extended to other high-spin ground state molecules, trapping of the two simple molecules CrH and MnH must be feasible.

To check the performance of our experimental setup, chromium atoms are buffer-gas cooled and magnetically trapped. For monitoring CrH and MnH in the trapping field, it is crucial to know the Zeeman tuning of the ground and the excited states. This tuning is measured and all necessary spectroscopic parameters are determined. Following these experiments, the potential to confine and store CrH and MnH molecules is investigated. Both species have been trapped, however, severe limitations on the storing times are given by inelastic collision-induced Zeeman relaxation with the buffer-gas atoms. These processes are investigated using a simulation of the cooling and trapping dynamics of the molecule ensemble. By fitting this simulation to our measurements, inelastic collision cross sections for both molecules are determined, and the details and limitations of cooling and trapping both molecules using this technique are studied.

1.5 Outline

This thesis is organized as follows:

- Chapter 2 starts with a discussion of the main principles as well as the limitations of the technique of buffer-gas cooling and subsequent magnetic trapping. CrH and MnH are identified as appropriate candidates for cooling and trapping in our system.

- The experimental realization of this technique is presented in Chapter 3. It gives an overview of the central parts of the technological infrastructure, which includes the dilution refrigerator, the buffer-gas cell as well as the superconducting quadrupole magnet.

- Cooling and trapping of atomic chromium served as a test of our system. The results from these experiments are summarized in Chapter 4.

- In Chapter 5 the numerical simulation used to describe cooling and trapping, is detailed. This program is extensively used in the investigation of the trapping dynamics in Chapter 6 as well as for the illustration of the principles and limitations of this technique in Chapter 2.

- Chapter 6 treats the buffer-gas cooling and trapping experiments on CrH and MnH molecules. The molecule dynamics are investigated, and the collision properties of CrH and MnH are deduced.

- In Chapter 7 the main results of the work presented in this thesis are summarized. Chapter 8 is the german version of this summary.

- The numerical program used for extraction of the number density and the temperature information from the data of trapped atomic chromium is described in Appendix A.

- The Zeeman spectroscopy experiments to determine the tuning of the ground and excited states of CrH in the magnetic trapping field are described in Appendix B. This information is needed for monitoring the molecules in our magnetostatic trap.

Chapter 2

Buffer-gas cooling and magnetic trapping

2.1   Introduction

Buffer-gas cooling is a powerful technique, since it only relies on thermalization of the species to be cooled with a cold background gas. As a consequence it is applicable to virtually all atomic and molecular species. When He is used as a buffer-gas, it also offers the benefit of potentially producing large samples at sub-Kelvin temperatures with high densities. However, if the particles are to be loaded into a magnetic trap, the general applicability is severely limited due to inelastic collision processes that can lead to trap loss. In this chapter, the details and limitations of buffer-gas cooling and subsequent magnetic trapping are discussed.

This chapter begins with a brief overview of the principle of buffer-gas cooling and magnetic trapping. This is followed by a section on the crucial role that collisions play for this method as well as by an overview of the physical processes leading to trap loss via Zeeman relaxation. Next, the various steps within the experiment are described, starting with a section on the production of the atoms and molecules of interest via laser ablation. After a discussion on the buffer-gas choice, the thermalization and trapping process is investigated. To illustrate these processes, we
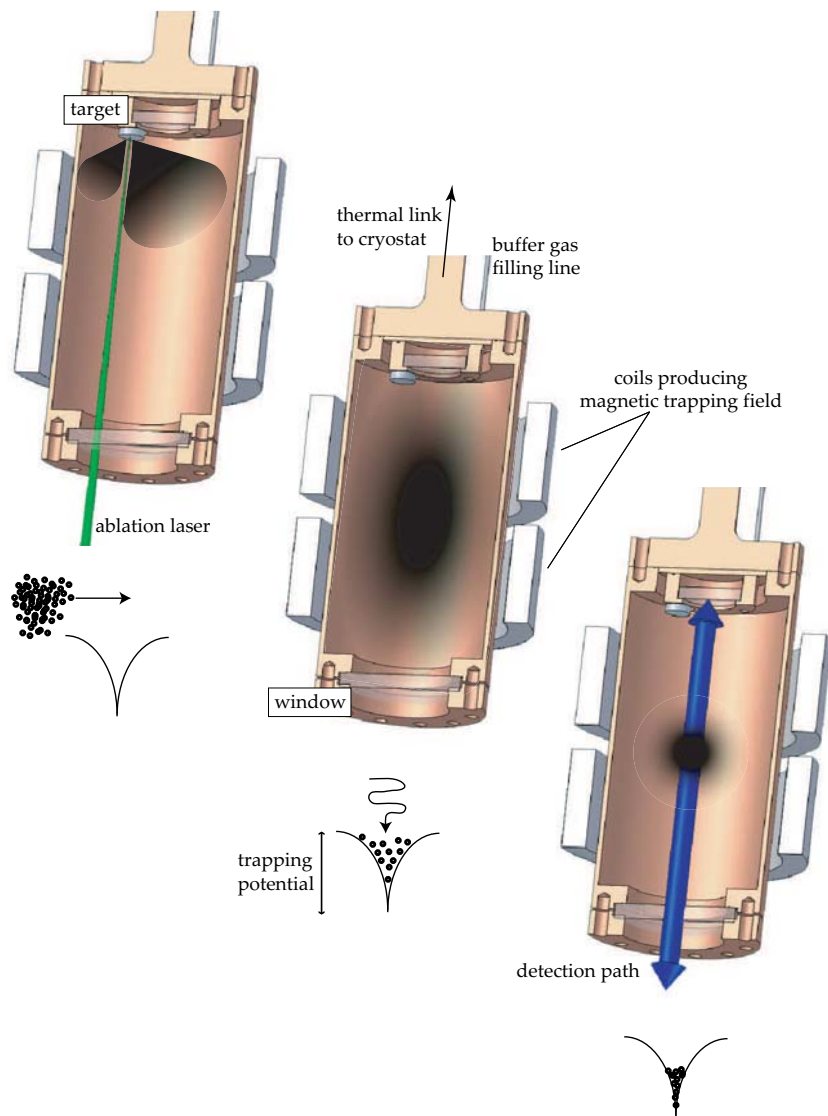
use the numerical simulations described in Chapter 5 to simulate the motion of a 1 Bohr magneton particle (with a mass similar to that of the species we study in this project) under various experimental conditions. After a discussion of trap loss by evaporation, the effects of inelastic collisions on the storage times are investigated. This chapter ends with a section on the search for the most appropriate molecular candidates for a cooling and trapping experiment in our system.

2.2 Overview of the technique

The method of buffer-gas cooling and subsequent magnetic trapping starts by injecting initially hot, paramagnetic atoms or molecules into a cold gas. Via elastic collisions, the particles are cooled as they thermalize with the buffer-gas to the temperature of the cell walls. If this cooling process is quick enough to reduce the particle's energy to below that of the trap depth of the present magnetic trapping field (see Equation 2.10) before they are lost to the cell boundaries, they will be confined and stored. Subsequent extraction of the buffer-gas allows for studying clean and isolated trapped atom or molecule samples.

The technique has been realized here with the help of a helium-filled copper cell, attached to a dilution refrigerator. This cell is surrounded by a superconducting magnet in anti-Helmholtz configuration, producing a trapping field with a local field minimum in the center of the cell. It is a natural thing to use helium as a buffer-gas, since it is the only species with a large enough equilibrium number density (see Figure 2.4) to provide enough collisions for cooling the particles to temperatures below the producible trap depths that are on the order of a few Kelvins (see Section 2.3.2). While offering a large enough trapping volume, the immense magnetic fields necessary for creating such deep traps can only be generated by superconducting magnets. Since such devices need to be cooled to cryogenic temperatures, it is ideal to combine them with liquid ^{4}He cryostats. In any case, it is necessary to use a cryostat for housing the dilution refrigerator needed to reach the sub-Kelvin temperature regime.

The subsequent steps in the experiment are illustrated in Figure 2.1. We start with the creation of gas-phase atoms or molecules via laser

target

thermal link
to cryostat

buffer gas
filling line

coils producing
magnetic trapping field

ablation laser

window

trapping
potential

detection path

18

Figure 2.1: Scheme of the subsequent steps in a buffer-gas loading and magnetic trapping experiment. Initially, hot paramagnetic particles produced via laser ablation, enter a cell volume filled with buffer-gas (left). Via elastic collisions with helium atoms the particles are thermalized (middle) and then confined in a local field minimum, produced by coils in anti-Helmholtz configuration, where they can be spectroscopically studied (right).

ablation from a solid precursor within the copper cell (Figure 2.1 (left)). A hot plume of particles enters the cell volume, cools (middle), and if the magnet is switched on, they diffuse to the trapping center where they are confined and can be spectroscopically studied (right). When long storing times of several seconds can be reached, it is possible to freeze the helium gas to the cell walls by lowering the cell temperature.

2.3 Magnetic trapping

Magnetic trapping allows spatial confinement of paramagnetic particles via the interaction of the magnetic field $\boldsymbol{B}$ with the magnetic moment $\boldsymbol{\mu}$ that results in an energy shift

$$\Delta E = -\boldsymbol{\mu} \cdot \boldsymbol{B} \tag{2.1}$$

of the atomic or molecular state via the Zeeman effect.

2.3.1 Atoms and molecules in external magnetic fields

The magnetic moment $\boldsymbol{\mu}$ of a particle originates from its internal angular momenta. In the case of an atom with no nuclear spin (*e.g.*, the ^{52}Cr isotope), the total angular momentum $\boldsymbol{J}$ can be composed of the orbital angular momenta of the electrons $\boldsymbol{L}$ and the electron spins $\boldsymbol{S}$. For most lighter atoms (atomic number $Z < 60$), the individual angular momenta of the electrons are coupled via Russel-Saunders-coupling. In this case, the total angular momentum $\boldsymbol{J}$ is given by $\boldsymbol{J} = \boldsymbol{L} + \boldsymbol{S} = \sum_i \boldsymbol{l}_i + \sum_i \boldsymbol{s}_i$, where $\boldsymbol{l}_i$ and $\boldsymbol{s}_i$ are the orbital and spin angular momenta of the individual electrons. If a nuclear spin $\boldsymbol{I}$ has to be taken into account, the total angular momentum $\boldsymbol{F}$ is given by $\boldsymbol{F} = \boldsymbol{J} + \boldsymbol{I}$.

The corresponding magnetic moment in the absence of nuclear spin $\boldsymbol{\mu}_J$ is given by [86]

$$\boldsymbol{\mu}_J = -g_J\mu_B\frac{\boldsymbol{J}}{\hbar}, \tag{2.2}$$

where g_J is the corresponding Landé factor and $\mu_B = e\hbar/2m_e$ is the Bohr magneton; $\hbar$ is the Planck constant divided by 2π, e is the elementary charge and m_e is the rest mass of the electron.

The resulting energy shift in an externally applied magnetic field is then given by

$$\Delta E = -\boldsymbol{\mu}_J \cdot \boldsymbol{B} = g_J m_J \mu_B B \tag{2.3}$$

Equations (2.2) and (2.3) are, however, only correct in the weak field limit, where the energy shift ΔE is small compared to the energy splitting arising from spin-orbit coupling. In this regime, the energy splitting due to the interaction of the magnetic moment with an external magnetic field is known as the *Zeeman-effect*. At higher fields, the internal angular momenta decouple and interact individually with the magnetic field. In the strong field limit, the resulting energy splitting is known as the *Paschen-Back-effect*. In this case, the resulting energy shift is given by [86]

$$\Delta E = \mu_B(m_L + 2m_S)B, \tag{2.4}$$

where m_L and m_S are the projections of the orbital angular momentum and the spin angular momentum on the quantization axis.

Between the Zeeman and the Paschen-Back regime, the energy shift cannot be calculated with the help of simple expression like (2.3) or (2.4). In this case, the problem has to be treated by setting up an appropriate Hamiltonian that contains all the relevant coupling terms. The energy shifts can then be calculated by solving the Schrödinger equation for a specific basis set of wave functions.

For molecules, the situation is more complex due to the additional rotational angular momentum as well as internal quantization axes. For linear moelcules, the influence of rotational and electronic motion on each other and the different possibilities how the angular momenta couple to each other is described by the *Hund's coupling cases*. Choosing an appropriate case for describing a specific molecular system also defines the adequate quantum numbers for specifying its energy states.

Let's consider a Hund's coupling case a), where $\boldsymbol{L}$ and $\boldsymbol{S}$ both couple to the molecular exis. In this case $\boldsymbol{L}$ and $\boldsymbol{S}$ precess around the molecular axis with projections Λ and Σ onto this axis in the molecule fixed reference frame. The corresponding magnetic moment along this axis is then given by [87]

$$\mu_\Omega = (\Lambda + 2\Sigma)\mu_B \qquad (2.5)$$

If the molecule rotates, the molecular axis precesses around the angular momentum $\boldsymbol{J}$ leading to a time averaged magnetic moment $\langle \mu_J \rangle$ along $\boldsymbol{J}$. If now an external magnetic field $\boldsymbol{B}$ is applied, $\boldsymbol{J}$ starts to precess around the direction of $\boldsymbol{B}$. This results in an effective magnetic moment μ_{eff} along the external magnetic field which is then given by [87]

$$\mu_{eff} = \langle \mu_J \rangle \cos(\boldsymbol{J}, \boldsymbol{B}) = \frac{(\Lambda + 2\Sigma)(\Lambda + \Sigma)M}{J(J+1)}\mu_B, \qquad (2.6)$$

where $(\boldsymbol{J}, \boldsymbol{B})$ is the angle between $\boldsymbol{J}$ and $\boldsymbol{B}$ and where $M\hbar$ is the projection of $\boldsymbol{J}$ onto $\boldsymbol{B}$. The corresponding Zeeman splitting of the energy levels can then be calculated according to the relative simple expression

$$\Delta E = \mu_{eff} \cdot B = \frac{(\Lambda + 2\Sigma)(\Lambda + \Sigma)M}{J(J+1)}\mu_B B. \qquad (2.7)$$

However, in reality molecules hardly can be described by pure Hund's cases, but as a mixture of these. In addition, Equation (2.7) can only give a good description of the magnetic-field-induced energy shifts if these are small with respect to the coupling strength of the angular momenta (*i.e.* in the low field limit). Generally, the energy levels have to be calculated by solving the Schrödinger equation for an effective Hamiltonian. As mentioned above, such a Hamiltonian needs to contain all the relevant coupling terms for an adequate description of the interaction of the particle with the magnetic field. The corresponding energy shifts can then be calculated by diagonalization of the effective Hamiltonian matrix, expressed in a specific basis set of wave functions $\Psi_{\text{case a)/b)/c)/d)}}$ - corresponding to the Hund's coupling cases a), b), c) and d) -, suited

for describing the couplings between the momenta. The energy shifts can then be calculated according to

$$H_{Zeeman}\, \Psi_{\text{case a)/b)/c)/d)}} = \Delta E\, \Psi_{\text{case a)/b)/c)/d)}}. \qquad (2.8)$$

The eigenenergies of such a Zeeman Hamiltonian depend on the particular properties of the species, but typically degenerate angular momentum states are split into multiple energy levels. A detailed description of a specific effective Hamiltonian and how relevant coupling terms are determined for the CrH molecule can be found in Appendix B.

2.3.2 The magnetic trapping field

The magnetic quadrupole is probably the most simple configuration generating a local field minimum in free space. It consists of two axial coils that allow for creation of two counter propagating current loops as shown in Figure 2.2.

The magnetic fields produced by each coil can be calculated using Biot-Savart's law. The coils produce two cylindrically symmetric fields, $\mathbf{B}_1$ and $\mathbf{B}_2$, with opposite signs that cancel in the center. This way a local field minimum in space is created that defines the trapping center for paramagnetic atoms or molecules.

In this field, particles in thermal equilibrium are distributed according to a Boltzmann distribution, given by

$$N(B(r,z)) = N_0 e^{-\frac{\mu B(r,z)}{k_B T}}, \qquad (2.9)$$

where N_0 is the particle density at the trap center, μ is the magnetic moment, T is the temperature and k_B the Boltzmann constant. For confinement, the particles therefore have to be cooled to temperatures below the trap depth, which is given by

$$T_{trap} = \frac{\mu B_{max}}{k_B}. \qquad (2.10)$$

Typical field strengths, producible in state-of-the art (superconducting) magnets, are on the order of a few Tesla. For a particle with $\mu = \mu_B$ and a maximum trapping field of 1 T, the corresponding trap depth is
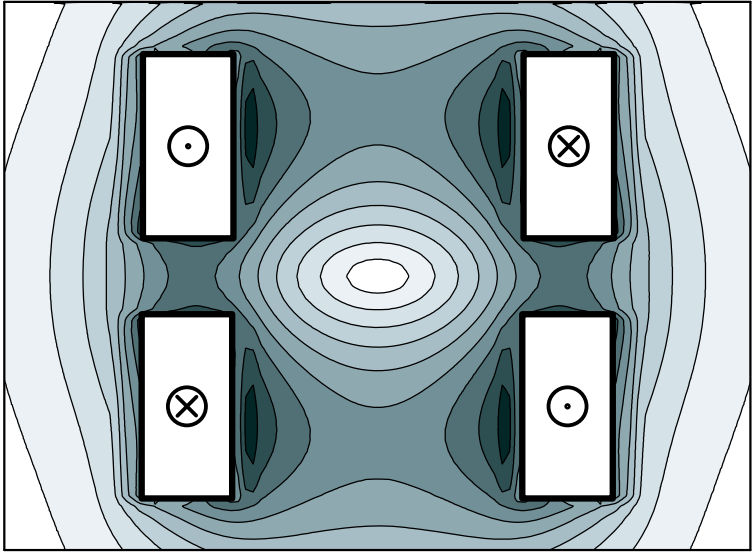
Figure 2.2: Trapping field generated by two coils in an anti-Helmholtz configuration (indicated by the top and bottom white rectangles), creating a local field minimum in free space.

~ 0.7 K. To trap particles with low magnetic moments, temperatures below 1 K are therefore necessary. A refrigerator system that provides sufficient cooling power to reach these temperature regimes is a dilution refrigerator. Since such a system needs a liquid helium cryostat for precooling, a superconducting quadrupole magnet can be integrated.

2.4 Collisions

2.4.1 Elastic and inelastic collisions

As already mentioned, the technique of buffer-gas cooling relies on thermalization of the injected particles with a gas that is cooled by a cryogenic refrigerator. This cooling process relies on elastic collisions that do not change the internal energy states of the injected atoms or molecules.

A detailed treatment of this thermalization process is given in Section 2.6.2.

As cooling is done by elastic collisions, this method is largely independent of the inner structure of the particles and thus should be applicable to most atoms and molecules. However, trapping relies on the interaction between the effective magnetic moment and the field strength. Since the magnetic moment depends on the internal state of the particle, we rely on stability regarding the internal energy states. Inelastic collisions that per definition change these, potentially make particles high field seeking and can therefore severely limit the general applicability of this trapping technique in connection with buffer-gas cooling.

2.4.2 Physical mechanisms of inelastic collision

Several different channels through which inelastic collision-induced Zeeman relaxation can occur, do exist. The following section gives an overview of the underlying physical mechanisms that lead to Zeeman relaxation-induced trap loss, starting with the dominant mechanisms for atomic species. All those mechanisms do exist in molecules as well, but molecular trap loss is predicted to be completely dominated by additional loss channels involving the rotational motion. This is a mechanism unique to molecules and is discussed at the end of this section.

Spin exchange

In spin exchange collisions, the spin of a particle is changed on the expense of the spin of the collision partner. One of the mechanisms inducing this is the coupling of the momenta of the two colliding particles through the van der Waals interaction in close proximity. For two particles $|s_1, m_1\rangle$ and $|s_2, m_2\rangle$ with spins s_1, s_2 and projections m_1, m_2 onto the quantization axes, this can symbolically be written as

$$|s_1, m_1\rangle|s_2, m_2\rangle \rightarrow |s_1, m_1 \pm 1\rangle|s_2, m_2 \mp 1\rangle. \qquad (2.11)$$

It is important to note, that if both particles are in the maximum polarized state with $|m| = s$, the final and initial states of the particles have to be the same and no angular momentum can be exchanged. Due to the lack of spin, this process has no impact on collisions with ground-state

^{4}He, but the ^{3}He nuclear spin can potentially participate. However, corresponding cross sections for alkali atom-^{3}He collisions are typically 10^9 times smaller than the elastic collisions cross sections [88] and similar values can be expected for molecule-^{3}He collisions [89].

However, typical spin exchange collision rates for collisions *between trapped atoms* below $1\,\mathrm{K}$ are on the order of $10^{-11}\,\mathrm{cm}^3\mathrm{s}^{-1}$ [90, 91, 92]. This is rather high and can lead to a self purification of the trapped atom ensemble, since all particles that are not in the maximum polarized state (*i.e.* $|m| \neq s$) can potentially be transferred to untrappable states via such spin exchange events.

Spin-exchange can also happen between magnetically trapped molecules, but since the observed densities are typically several orders of magnitude lower than for atomic species, this mechanism is of little importance.

Dipolar relaxation

During a collision event in close proximity, the magnetic dipole moments of the particles interact with each other. This leads to a coupling of the magnetic moments and the relative motion of the particles through which the electron spins of the particles can relax. The resulting loss rates are strongly dependent on the particle's scattering properties. For alkali atoms and atomic hydrogen typical rates lie in the range of $10^{-16}\,\mathrm{cm}^3\mathrm{s}^{-1}$ to $10^{-14}\,\mathrm{cm}^3\mathrm{s}^{-1}$ [90, 93, 94]. Again, because of the low densities of molecules in the trap, this loss channel is presumably not important for molecular species.

Shape resonances

An enhancement of the probability for spin-flip collisions can be induced by shape resonances, *e.g.* when during a collision event a quasi-bound particle-helium complex is formed. The lifetimes of these states are longer than the duration of a typical collision. In such a long-lived state, the particles orbit each other and the Zeeman relaxation rate of the species of interest is enhanced via perturbations induced by the helium atom. The probability for this process has a resonance for the case that

the kinetic energy of the particles is equal to the energy of the quasi-bound state.

Spin relaxation induced by anisotropy in the electron cloud

Another mechanism for changing the Zeeman state of a paramagnetic atom or molecule can be induced by an anisotropy in the particle's electron cloud. For an atom or molecule to be non-spherical, it must have non-zero orbital angular momentum and it therefore must have different orientations of the orbital angular momentum relative to the collision axis; as a result the energy can be shifted by different amounts. This results in a precession of the orbital angular momentum, which in turn can cause a change in the Zeeman state via the spin-orbit coupling [95]. As a consequence, buffer-gas cooling and magnetic trapping is preferably applied to electronic S ground state atoms and molecules with Σ ground states, although trapping experiments on several rare earth atoms indicate that anisotropy-induced Zeeman relaxation can be reduced by shielding of the valence electron shell by outer filled s-orbitals [96, 63]. No similar behavior, however, has yet been observed for molecules.

Molecular spin-rotation interaction

An additional Zeeman relaxation channel, unique to molecules, is given by the coupling of the spins to the rotational motion of the molecule. For the reasons given above, Σ ground state molecules are the preferable species for buffer-gas loading into a magnetic trap. The most simple paramagnetic molecules with a total angular momentum of $L = 0$ have a ground state of $^2\Sigma$. Because rotationally excited molecules are quickly cooled to the rotational ground state, we always trap the $N = 0$ state, for which spin-rotation coupling cannot lead to Zeeman relaxation. However, it has been predicted that Zeeman relaxation can get induced via spin-rotational coupling between the rotational ground state and rotationally excited states that get mixed into the rotational ground state during a collision event [84]. Calculations for CaF and CaH molecules have shown that Zeeman relaxation rates for these species strongly increase with an increasing spin-rotation interaction constant γ_{sr} and decrease with the energy separation between rotational states. The ex-

perimental data available for these molecules confirm this, and ratios of elastic to inelastic collisions of $> 10^4$ have been found [58, 97]. Since this ratio is rather small, Zeeman relaxation induced by spin-rotation interaction seems to constitute a huge trap loss channel for $^2\Sigma$ ground state molecules.

Molecular spin-spin interaction

The spin-rotation-induced Zeeman relaxation mechanism described above will also be present in $^3\Sigma$ molecules. It is, however, predicted that the Zeeman relaxation rates are considerably higher due to the presence of another relaxation channel. In $^3\Sigma$ states, the spin-spin interaction mixes some $N = 2$ character into the rotational $N = 0$ ground state that in turn leads to Zeeman relaxation. The amount of $N = 2$ admixture depends on the ratio λ_{ss}/B and as a consequence, the spin-spin interaction parameter λ_{ss} should be relatively small and the rotational constant large to successfully trap molecules [84]. For the NH ($^3\Sigma^-$) radical, a favorable ratio of elastic to inelastic collisions of $7 \cdot 10^4$ has been found [80]. This value is in agreement with predicted values [98, 85].

2.5 Sample production

2.5.1 Laser ablation

Among the various techniques available to produce a gas-phase sample of the species of interest for subsequent cooling and trapping, laser ablation from a solid precursor material has been found to be especially suitable for buffer-gas loading in a cryogenic environment [99, 58, 63]. Particularly appealing is the fact that an implementation of this technique only requires a simple experimental cell with optical access. Laser ablation is a powerful tool, as it provides an easy way of producing gas-phase particles and is applicable to many species, especially atoms. Moreover, both molecules that we have used in this work, chromium hydride and manganese hydride, can be produced via this technique. A brief overview of other available injection methods is given in the next section.

A laser pulse, loosely focused on this target, is partially absorbed and the deposited energy results in melting, evaporation and plasma

formation. In a very complex process, all kinds of different species are formed and are ejected in a hot plume of several hundred degrees Kelvin. The physical details of laser ablation are not well understood, so that the optimum experimental conditions to maximize the yield and avoid the production of unwanted species is determined by trial and error. A frequency Nd:YAG laser is a suitable source for laser ablation. Typical pulse energies used are between 10 and 20 mJ for pulse durations of around 10 ns at a wavelength of 532 nm.

Unfortunately, large shot-to-shot signal fluctuations induced by variations in the amount of produced particles in the ablation plume, require the acquisition of many data points to reduce the statistical error. This can be a problem, since a constant base temperature of the experimental cell is crucial and thus the repetition rate of the experiment is limited by the cooling power of the cryogenic system. To avoid an intolerable increase of the helium buffer-gas temperature, this base temperature should in addition be kept as low as possible. In practise, this limits the repetition rate in most of our experiments to ~ 0.3 Hz.

The heat transferred to the dilution unit of the cryostat must not increase the temperature of the mixing chamber above a threshold of ~ 1 K, since this would result in a significant drop in the cooling power of the system [100]. The thermal contact from the precursor to the mixing chamber therefore has to be carefully engineered, and the amount of pulse energy converted to heat has to be balanced against the typically low cooling power in the cryogenic environment.

2.5.2   Other techniques

Several other methods have been developed for injecting particles into a cryogenic buffer-gas. Although these methods are not implemented in our experimental setup they are briefly described here for completeness.

Molecular beam loading

While laser ablation is well suited for substances whose precursor material is already solid at room temperature, an alternative for other species has been demonstrated with the successive buffer-gas cooling [101] and

magnetic trapping of a beam of NH and ND radicals [80]. In these experiments a molecular beam machine is connected to a cryostat and a sample of molecules travelling in a He carrier gas enters the buffer-gas cell via a small opening in the cell walls. The use of molecular beam loading greatly extends the number of possible species. Moreover, employing the versatile and mature methods available to produce and manipulate gas-phase particles in thermal beams, a particle selection or state preparation becomes possible prior to injection in the buffer-gas cell.

However, implementation of this technique adds additional complexity to the already technically challenging experimental realization of buffer-gas loading a magnetic trap. One of the big problems is connected to the escaping He gas that breaks the vacuum, necessary for thermally isolating the inner parts of the cryogenic system. For this reason beam loading seemed not to be the optimum method for injection at the start of this project.

Capillary injection

A third way of introducing particles into the buffer-gas cell at cryogenic temperatures, is capillary injection that has been successfully implemented for CO [102], NO [103], H_2S [104], HCN [105] and SrO [106]. A thin capillary connects the low temperature buffer-gas cell with a room-temperature gas supply and molecules are driven into the cell by the supply pressure.

The method is simple, but has limited applicability since only stable molecules with high vapor pressures at low temperatures can be used without condensation and subsequent clogging at the inner walls of the thin filling capillary. Although resistive heating of the capillary can avoid condensation of the gas on its way to the trapping region, care has to be taken to make the heating needs compatible with the stringent thermal restrictions set by the limited cooling capabilities of the employed refrigerator.

Discharge etching

The basic idea of this injection method is to create a discharge plasma in the buffer-gas to remove atoms that are frozen on the cell wall, and thus

bring them into the gas-phase. It has successfully been implemented in a trapping experiment on metastable helium, created in a plasma inside the cell by a resonator coil. A fraction of about 10^{-6} of the helium atoms is transferred into the paramagnetic metastable state and subsequently gets cooled by the remaining helium atoms [79]. This method has up to now only been used for metastable He and it is unclear whether it will be applicable to a broader range of species.

2.6 Buffer-gas cooling

2.6.1 The choice of buffer-gas

Shortly after the injection of hot particles into the buffer-gas cell, they need to be cooled to temperatures below the trap depth of typically a few Kelvins (see Equation 2.10), before they reach cell walls where they are lost. Its a natural choice to use either ^{3}He or ^{4}He as a buffer-gas, since it is the only gas with a large enough vapor density for cooling at temperatures below $1\,$K. In addition, helium is a noble gas and thus, for the most part chemical reactions between the buffer-gas atoms and the injected species are avoided.

As explained in the following section, theoretical estimates indicate that a helium buffer-gas density of about $\sim 10^{16}\,\mathrm{cm}^{-3}$ is needed to thermalize a good fraction of initially hot atoms or molecules before they hit the cell walls and presumably are lost. This requirement puts a limit on the temperature of the buffer-gas as Figure 2.3 indicates. Here the equilibrium temperature-dependent vapor density curves for both helium isotopes are plotted [100]. The grey bars indicate the optimal density and corresponding temperature regime for thermalization and loading of a magnetic trap. While ^{3}He can be used down to temperatures of $\sim 0.25\,$K in the case of ^{4}He the required number densities are only accessible down to temperatures of $\sim 0.6\,$K.

In our work we have used both ^{3}He and ^{4}He buffer-gas species. As Figure 2.3 indicates, ^{4}He has the advantage that after thermalization it can be frozen to the cell walls via lowering of the cell temperature more easily. However, our observations indicate that in order to successfully get rid of a large fraction of the buffer-gas with the cooling power
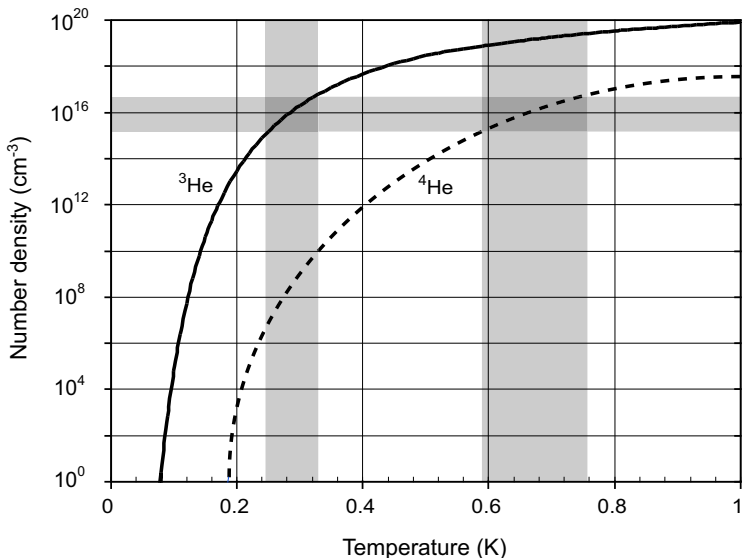
Figure 2.3: Equilibrium number densities for ^{3}He (solid line) and ^{4}He (dashed line) as a function of temperature. The grey areas indicate the optimal density and temperature regimes for thermalization and loading of initially hot particles into a magnetic trap as explained in Section 2.6.2.

given by our cryogenic system, long trapping times on the order of $10\,\mathrm{s}$ are required. ^{3}He, on the other hand, has the advantage that lower cell temperatures can be used for loading. Unfortunately, our loading temperature is determined by the heat of the ablation pulse used for injection of the atoms and molecules into the helium gas. This temporarily increases the cell temperature to $\sim 0.8\,\mathrm{K}$ and thus we cannot make use of this. The helium density at these elevated temperatures is limited by the amount of gas filled into the cell.

2.6.2 The thermalization process

Thermalization of hot particles via injection into a cold buffer-gas relies on the elastic collisions between the injected species and the helium buffer-gas atoms. To illustrate the thermalization process, we use the numerical Monte Carlo simulation described in Chapter 5 and evaluate the velocities of particles after various collision events. 2000 particles, initially 1000 K hot, have been injected into a ^{3}He buffer-gas with a temperature of 0.5 K. The mass of the particles was chosen to be 50 atomic mass units (amu), a value close to the mass of all species we have used in this work. Figure 2.4 (left) shows the velocity distribution of the injected particles after 0, 10 and 30 collisions. The resulting velocities are fitted to the one-dimensional Maxwell-Boltzmann distribution given by

$$f(m_i, T, v_i) = 4\pi \left(\frac{m_i}{2\pi k_B T} \right)^{3/2} v^2 \exp\left(-\frac{m_i v_i^2}{2k_B T} \right), \qquad (2.12)$$

where m_i and v_i is mass and the velocity of the injected species, k_B is the Boltzmann constant and T is the temperature.

The right side of Figure 2.4 shows the fitted temperature as a function of the collision events. As one can see, on the order of 70 collisions are needed to thermalize the molecules to below 1 K, a temperature that corresponds to typical trap depths that can be produced. This result is consistent with an estimate based on an analytical model describing the thermalization process [107, 77].

To ensure that the atoms or molecules thermalize before impinging on the wall of the cell that surrounds the trap, it is necessary that the density of the buffer-gas is large enough to allow for thermalization over a distance smaller than the size of the cell. To investigate the densities required to thermalize a good fraction of the injected particles we again made use of the Monte Carlo simulation. Figure 2.5 shows the density-dependent fraction of the particles mentioned above that is successfully thermalized to a temperature below 1 K within a ^{3}He-filled volume given by the size of our buffer-gas cell. Consistent with previous estimations [108], densities of $n \cong 5.0 \cdot 10^{15}$cm^{-3} are needed in order to thermalize $\sim 80\%$ of all injected particles, assuming a typical elastic cross section of $\sigma_{el} = 10^{-14}$ cm^2 for collisions with ^{3}He atoms.
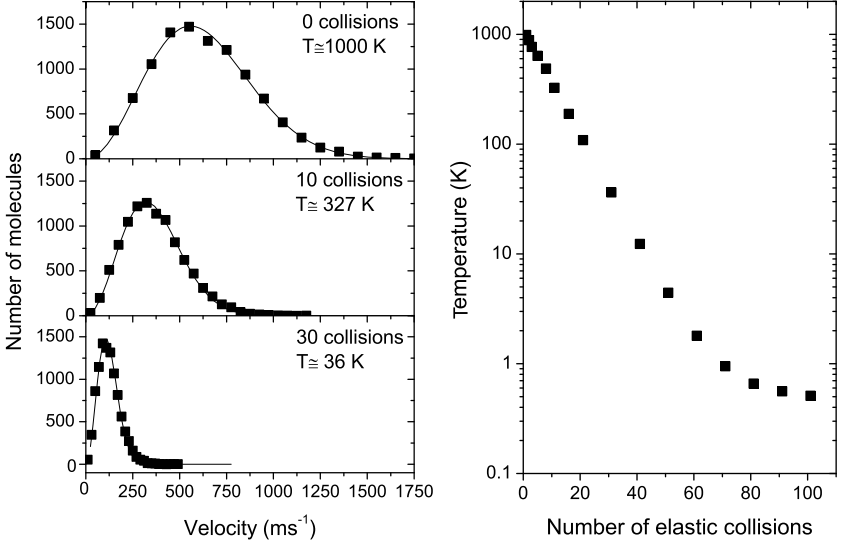
Figure 2.4: *left*: Simulated velocity distribution of particles with a mass of 50 amu together with fits of the Maxwell-Boltzmann velocity distribution after 0, 10 and 30 collision events.
right: Temperature as a function of the number of elastic collisions.

With this information we can now calculate the time necessary to thermalize the molecules. The density dependent elastic collision rate k_{el} is related to the elastic collision cross section via

$$k_{el} = \sigma_{el} \cdot v_{rel}, \tag{2.13}$$

where v_{rel} is the relative velocity between the ^{3}He and the particle. The number of collisions per second N_{coll} at a certain buffer-gas density is then simply given by

$$N_{coll} = k_{el} \cdot n(^3\text{He}). \tag{2.14}$$

Assuming 70 collisions at a helium buffer-gas temperature of $0.5\,\text{K}$, a density of $5.0 \cdot 10^{15}\text{cm}^{-3}$, and setting v_{rel} equal to the velocity of the helium atoms, this leads to a thermalization within a time of around
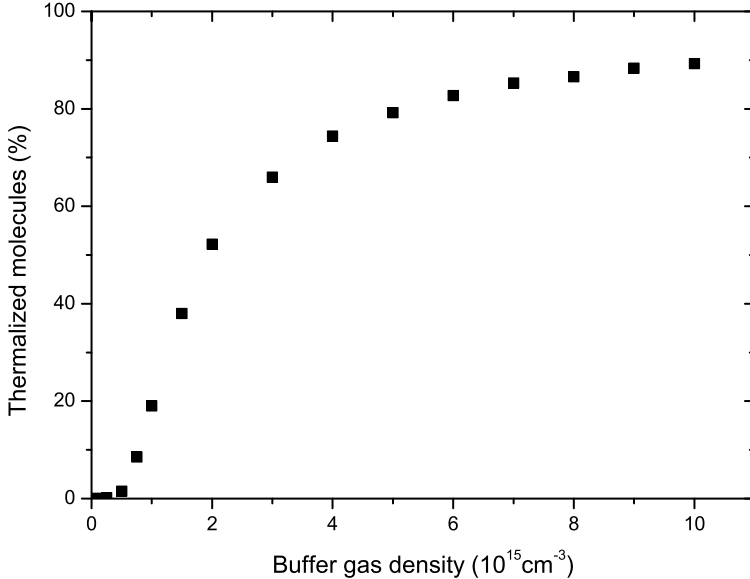
Figure 2.5: Buffer-gas density-dependent fraction of particles with a mass of 50 amu that get thermalized to temperatures below $1\,\mathrm{K}$ within the trap volume before they are lost at the cell walls.

$\sim 200\,\mu$s. This value can only be regarded as an upper limit, since at the initial temperatures v_{rel} is much larger than v_{He}.

2.6.3 Removal of the buffer-gas

A quick removal of the helium buffer-gas after thermalization can be important for several reasons. As will be explained in Section 2.7.1, evaporative trap loss can be significantly reduced by extraction of the helium that is responsible for repopulating the tail of the Boltzmann velocity distribution that cannot be confined in the magnetic trapping field. This is particularly important for particles with effective magnetic moments below $3\,\mu_b$ [82]. In addition to this, extraction of the buffer-gas reduces the rate of inelastic collisions with the helium atoms leading to

trap loss via Zeeman relaxation, as explained in Sections 2.7.2 and 6.5. Finally, breaking the thermal contact to the cell walls allows for further cooling by forced evaporation over the trap edge, known as evaporative cooling.

As can be seen from Figure 2.3, the helium buffer-gas can be frozen out by reducing the temperature of the cell. The condensation time is mainly determined by the cooling power provided by the ^{3}He-^{4}He dilution refrigerator, but typically it is feasible to extract ^{4}He within a time on the order of several seconds. Pumping timescales below 100 ms for particles with lower magnetic moments can be achieved by implementing a cryogenic active charcoal pump [82]. Such a pump consists of a separate chamber coated with charcoal and can be activated after thermalization by opening a valve to the trapping volume. Here, one usually enters a regime where the buffer-gas wind carries a certain fraction of particles out of the trap, initially causing an increased loss. This is, however, more than compensated by the drastically reduced collision-induced evaporative loss on longer timescales, which would otherwise be caused by the remaining buffer-gas.

For both methods, the cryogenic environment helps to provide an excellent vacuum after buffer-gas removal. However, the slow desorption of the remaining thin helium film coating the cell wall can still cause observable background loss, which ultimately limits the trap lifetime [82]. In combination with charcoal pumping, it can be further lowered by slightly increasing the cell temperature over some tens of seconds for a cryogenic "bake-out" after initial loading.

2.7   Trap loss

As long as particles are not actively added to the trapped ensemble after initial loading, their number will continuously be reduced by different loss mechanisms. Besides evaporation of particles over the trap edge, inelastic collisions as mentioned in Section 2.4.1 are the main sources for limitations on the storage time. The implications on the trapping time of these processes is investigated in the following sections.

2.7.1   Evaporative trap loss

Magnet design restrictions, given by the implementation of optical access and the size of the buffer-gas cell, have impact on the geometry of the trapping fields that can be generated. Usually, the trapping volume is limited by the inner walls of the experimental cell in radial direction and the magnetic field saddle point in axial direction (see Figure 2.6). Any particles crossing these boundaries are lost from the trap.

As already mentioned, particles in thermal equilibrium are distributed over the trapping field according the Boltzmann distribution, given by Equation 2.9. The thermal loss rate is then given by the number of particles arriving at these boundaries in a certain time interval. In an analytical approach, based on the diffusion of two gases through each other [77], it can be shown that the lifetime, governed by the loss rate, is growing exponentially with a parameter η. This parameter η is defined as the ratio of trap depth T_{trap} (see Equation 2.10) to the temperature of the particle ensemble, *i.e.*

$$\eta = \frac{T_{trap}}{T} = \frac{\mu B_{max}}{k_B T}, \qquad (2.15)$$

where B_{max} is the maximum field strength at the cell boundary.

Because only the most energetic particles will be able to reach the trapping field boundaries, evaporation is accompanied by a simultaneous decrease of the average energy of the ensemble. In the case where thermal contact to the cell wall is broken by removal of the helium gas, this effect can be exploited to cool the trapped particles by forced evaporation via decreasing the magnetic field strength [90].

In the presence of buffer-gas, the kinetic energy of the magnetically trapped species is rapidly thermalized. On the other hand, the transit of the trapped species to the trapping field boundaries is slowed by the elastic collisions with the helium atoms. In the absence of inelastic collisions, this leads to a considerable enhancement of the trap lifetime with increasing buffer-gas densities.

To investigate the dependence of the trapping time on η and the buffer-gas density, we use the numerical simulations described in Chapter 5 to calculate the lifetime dependence on η (again for a 1 Bohr magneton particle with a mass of 50 amu). The elastic collision cross section is set
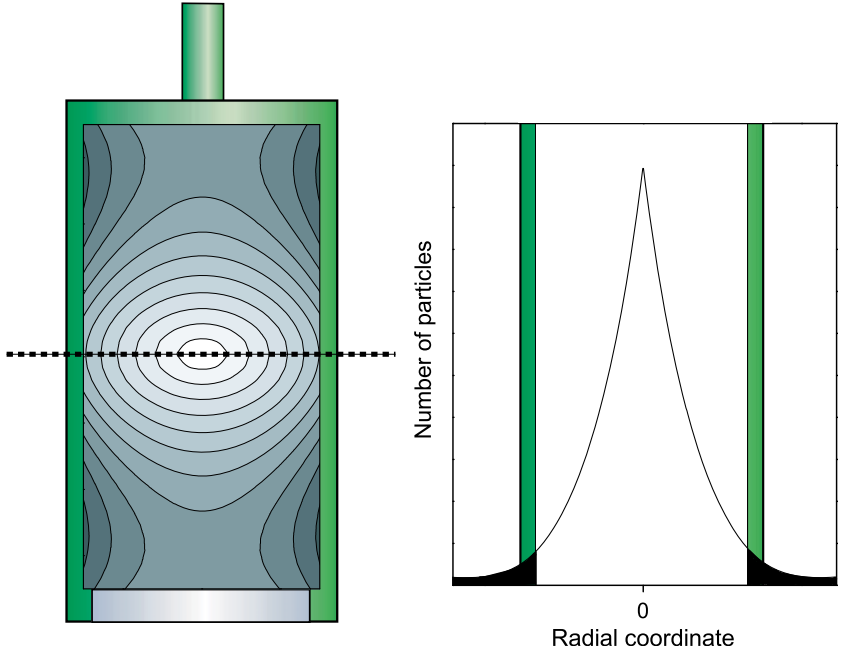
Figure 2.6: *left*: Characteristic trapping field that can be generated in a buffer-gas cell of typical size (⌀70 mm, height: 120 mm). The trapping volume is limited by the inner walls of the experimental cell in radial direction and the saddle-point of the magnetic field in axial direction.
right: Plot of the Boltzmann distribution of particles along the dashed line of the left figure. The bars indicate the cell walls and the two black areas indicate the tail of the particle distribution that, if constantly repopulated, serves as a trap loss channel.
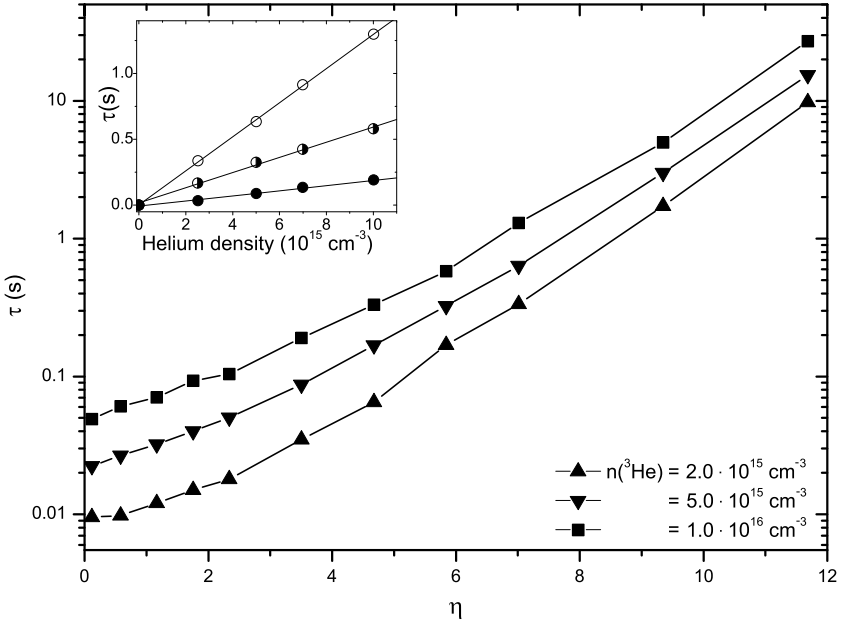
Figure 2.7: Numerically calculated trapping times τ versus η for particles with a mass of 50 amu in the presence of a ^{3}He buffer-gas of different densities $n = 1.0{\cdot}10^{16}$ cm^{-3} (squares), $5.0{\cdot}10^{15}$ cm^{-3} (down triangles) and $2.0{\cdot}10^{15}$ cm^{-3} (up triangles). The storing times exponentially rise with η.
The inset shows a plot of the trapping times against the buffer-gas density for η values of $\eta = 7$ (open circles), 5 (half circles) and 3.5 (full circles), indicating a linear dependence of τ on the helium density.

to a typical value of $10^{-14}\,\mathrm{cm}^2$ for the particle-^{3}He collisions at a gas temperature of $0.5\,\mathrm{K}$. Any effects arising from inelastic collisions are completely neglected.

Figure 2.7 shows a plot of the resulting trapping times in the presence of a ^{3}He buffer-gas of various densities. Consistent with previous studies [77, 107], the lifetime grows exponentially with η and exhibits a linear dependence on the helium density as shown in the inset of this figure.

## 2.7.2 Inelastic collision-induced trap loss

The situation changes dramatically when inelastic collisions are taken into account. Figure 2.8 shows a plot of trapping times versus buffer-gas density, simulated for the same particle at a fixed η-value of 12 (a value similar to that of the species we study in our system). In these simulations, the ratio of elastic to inelastic collisions $\gamma := N_{el}/N_{inel}$ is varied from $5 \cdot 10^7$ down to $2 \cdot 10^3$. The trapping behavior within this range can be divided into three regimes, labeled I, II and III in Figure 2.8. As one can see, the storage times in regime II drop up to an order of magnitude if the helium density is increased by a factor of 10. This is in contrast to what is shown in Figure 2.7, where the lifetime rises with increasing buffer-gas density. The source for this behavior lies in the enhanced number of inelastic collisions that lead to trap loss via Zeeman relaxation. Once the particle is transformed from a low-field into a high-field seeking state, the magnetic forces push it out of the trapping center where it can be lost at the cell boundaries (here on a typical timescale of roughly $\sim 1 - 10$ ms). If this happens for many particles within the trapped ensemble, the observed storing time is reduced. This is a general effect that can clearly be seen for values of $10^4 < \gamma < 5 \cdot 10^6$. However, for γ values outside of this region, a different behavior is found.

With a decreasing number of inelastic collisions, described by an increasing value for γ (regime I), this effect is less pronounced and reverses at a value of $\sim 1.0 \cdot 10^7$. Like predicted for the purely elastic scattering case shown in the inset Figure 2.7, the trapping time here rises if the helium density is increased from 1.0 to $5.0 \cdot 10^{15}\,\mathrm{cm}^{-3}$. However, adding helium always increases the number of inelastic collisions. This finally starts to affect the observable lifetime at densities exceeding $5.0 \cdot 10^{15}\,\mathrm{cm}^{-3}$.
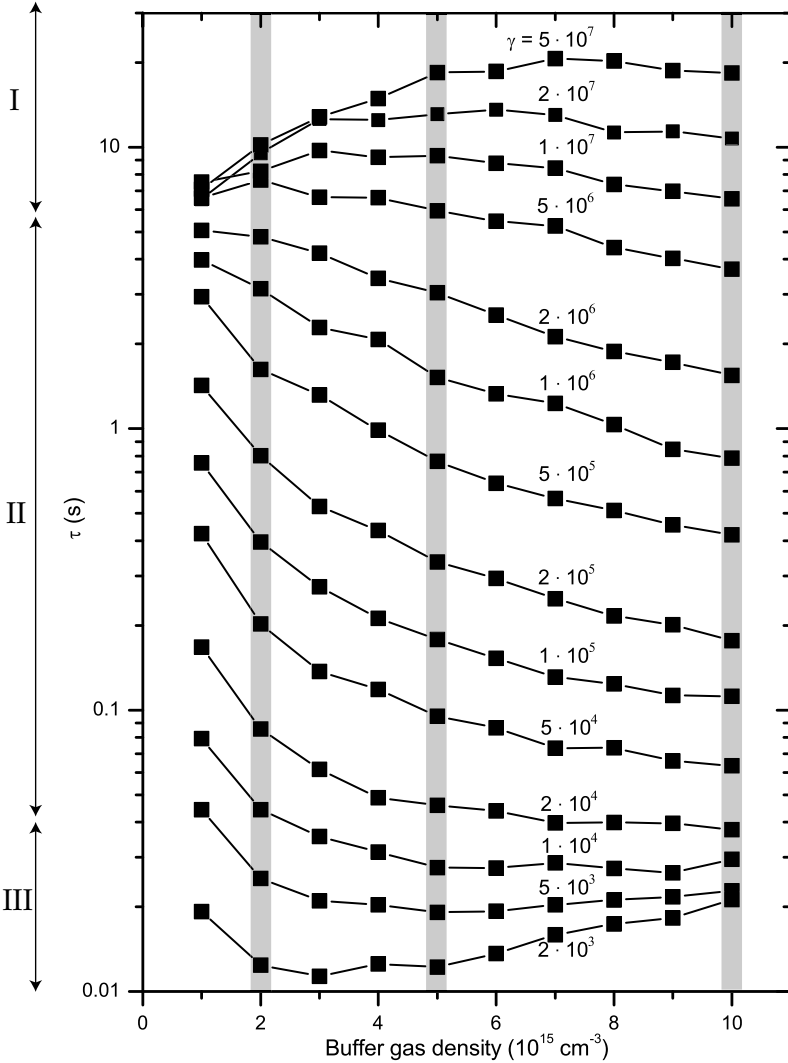
Figure 2.8: Numerically calculated trapping times versus the buffer-gas density for various ratios of elastic to inelastic scattering γ ranging from $5.0 \cdot 10^7$ down to $2.0 \cdot 10^3$. The grey bars indicate the lifetime values plotted in Figure 2.9.

For values of $\gamma < 10^4$ (regime III), Figure 2.9 shows that the lifetime at increasing buffer-gas densities decreases. Surprisingly, above $5.0 \cdot 10^{15}$ cm^{-3} τ increases with density. This effect is caused by an enhanced rate of transformation from low- to high-field seeking states (and vice versa) during the time the particle is in the trapping volume. Once in a high field seeking state, and thus on the way towards the cell walls, the time to the next inelastic collision is shorter than the time to get lost at the cell boundary. If that next inelastic collision scatters the particle into a low field seeking state and if this happens for many particles, the overall lifetime of the ensemble can get enhanced. This is an effect that is observed in our experiments on cooling and trapping of MnH and CrH molecules, as explained in Chapter 6.
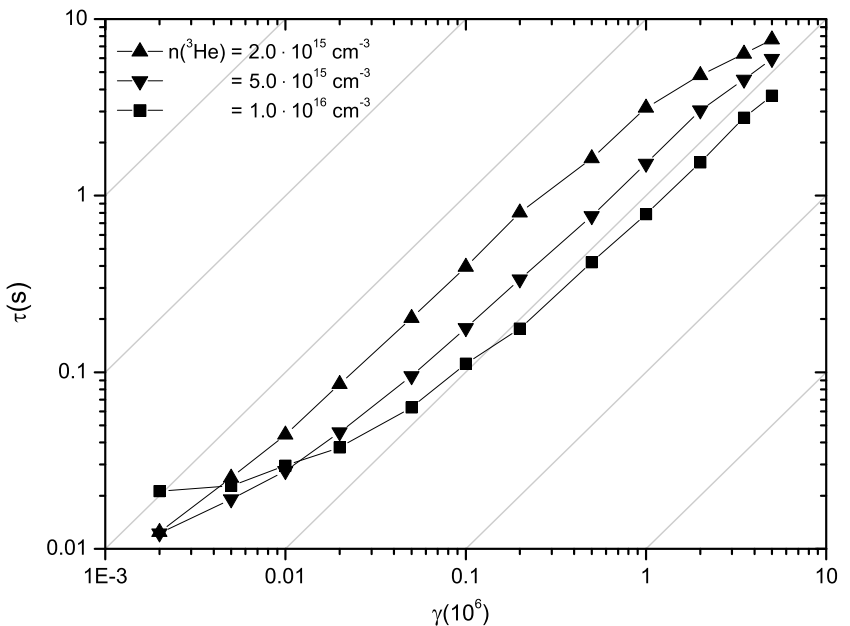
Figure 2.9: Trapping times versus γ for three buffer-gas densities. The trapping time rises more or less linearly with increasing ratio of elastic to inelastic collisions γ. The grey lines are a guide to the eye.

To get a feeling for the dependence of the observable storage times on the ratio of elastic to inelastic scattering processes, Figure 2.9 shows the calculated trapping times versus γ for buffer-gas densities $n = 2.0 \cdot 10^{15}$ cm^{-3} (up triangles), $5.0 \cdot 10^{15}$ cm^{-3} (down triangles) and $1.0 \cdot 10^{16}$ cm^{-3} (squares), respectively. As one can see, all three plots indicate that the lifetime rises more or less linearly with the decrease of inelastic collision processes. To trap atoms or molecules with a mass close to 50 amu, an η of 12 and a typical elastic collision cross section of 10^{-14} cm^2 for periods exceeding seconds, γ should not be smaller than 10^6.

2.7.3 Other trap loss mechanisms

Although not important for the experiments described in this thesis, additional trap loss mechanisms besides evaporation and inelastic collisions do exist. These are described here for completeness.

Majorana transitions

Particles moving in a magnetic trap experience a time-varying magnetic field which is changing in magnitude and direction in a very complex manner. To remain in the initial low field seeking state requires that the projection of the particles spin on the local direction of the magnetic field can adiabatically follow its change [109]. This will eventually be violated near the center of a quadrupole trap, where the field can change abruptly, leading to spin-flips into the lower-energy high-field seeking states [110]. The probability for these Majorana transitions is directly proportional to the number density in the magnetic field minimum, and as consequence gains importance with decreasing ensemble temperature. For experimental conditions in this thesis, however, the timescale for Majorana loss is on the order of thousands of seconds [89]. To avoid this loss channel, one could employ a magnetic trap with nonzero field at the potential minimum, such as the Ioffe trap [111], the Cloverleaf trap [112], or the QUIC trap [113].

Chemical reactions

An additional loss channel is given by possible chemical reactions between collision partners. Due to energy and momentum conservation, the exothermic formation of new species needs a third body to carry away the released energy. As a consequence typical loss rates indicate that these processes are extremely unlikely [90]. However, this is only true for atoms since not all molecular reactions need a third particle to carry away the reaction energy [29]. Chemical reactions serve as a possible explanation for the failed attempt to trap VO molecules [81].

Optical pumping by blackbody radiation

Optical pumping via blackbody radiation is another loss channel common to atoms and molecules. Confined particles can get excited into rotational and vibrational states via absorption of photons that are emitted from the thermally radiating surroundings of the trapping area. This can lead to a particle loss if the excited states are untrappable. The effect of blackbody radiation on the trapping time has been experimentally observed for molecular ions and clusters [114, 115]. Recently, the effect of blackbody radiation on the trapping time of neutral OH and OD radicals has been studied [116]. Since, however, our trap is surrounded by a cryogenic environment, the effect of blackbody radiation on the trapping time is negligibly small.

2.8   Search for molecular candidates

As He atoms are highly non-reactive and do not easily form new species, we can consider the helium buffer-gas cooling an universal cooling method. However, if the cooling is to be combined with magnetic trapping of the (paramagnetic) species, the universality is severely limited due to several constraints. At the heart of these constraints lie inelastic collisions described in the previous sections. The collision partners can be a molecule and a helium atom, but also two molecules. The former case is crucial for the feasibility of buffer-gas loading, while the latter governs a possible evaporative cooling process to further lower the temperature and increase the phase-space density of molecular samples.

For $^2\Sigma$ molecules the Zeeman relaxation occurs through spin-rotational coupling between the rotational ground state and rotationally excited states [84], as mentioned in Section 2.4.2. Therefore, Zeeman relaxation rates increase with the spin-rotation interaction constant γ_{sr} and decrease with the energy separation between rotational states.

In $^3\Sigma$ states, the spin-spin interaction is the dominating factor and again a larger energy difference between the rotational states decreases the couplings between low-field-seeking and high-field-seeking states. As a consequence, the spin-spin interaction parameter λ_{ss} should be relatively small and the rotational constant large to successfully trap molecules [84].

About the collisional properties of molecules in ground states other than $^2\Sigma$ or $^3\Sigma$, little is known. An unsuccessful attempt was made to buffer-gas cool and trap VO molecules ($^4\Sigma^-$ ground state), but it is unclear whether Zeeman relaxation was a problem [81]. Theoretical calculations that predict collisional properties of such high-spin molecules are unknown to us. By extrapolating the cases built for $^2\Sigma$ and $^3\Sigma$ molecules, we assume that the candidate molecule should possess a large rotational constant B and small spin-spin as well as spin-rotation interaction constants γ_{ss} and γ_{sr}. As diatomics containing hydrogen atoms are those with the largest rotational constants, metal hydrides form a natural choice.

Apart from such general criteria, more practical considerations also play a role. As explained in Section 2.3, the trap depth plays a crucial role in the possibility to confine species over longer time periods. A useful quantity to describe trapping is the ratio of trap depth to sample temperature η, as defined in Equation (2.15). As Figure 2.7 indicates, an η of ~ 8 is required to achieve storing times of several seconds for a particle with a mass 50 amu. Assuming a Boltzmann temperature of $0.5\,\mathrm{K}$ this yields a minimum magnetic moment of about $4.0\,\mu_B$.

Based on the criteria mentioned above, we have performed an extensive literature search to find suitable molecular candidates for buffer-gas cooling and magnetic trapping. The results are gathered in Table 2.1. To compile this table, only molecules have been listed that possess an electronic ground state with at least a fourfold multiplicity. For comparison, some molecules studied already using buffer-gas cooling have been

		B	λ_{ss}	$|\lambda_{ss}/B|$	γ_{sr} $\times 10^3$	ref.
GdO	$^9\Sigma^-$	0.355	-0.104	0.29	0.1	[117]
MnH	$^7\Sigma^+$	5.606	-0.004	$7.2\ 10^{-4}$	31.3	[118]
MnF	$^7\Sigma^+$	0.353	-0.005	$1.3\ 10^{-2}$	0.6	[119]
MnCl	$^7\Sigma^+$	0.158	0.037	0.24	0.4	[120]
CrH	$^6\Sigma^+$	6.132	0.233	$3.8\ 10^{-2}$	50.3	[121]
MnO	$^6\Sigma^+$	0.501	0.574	1.1	-2.4	[122]
CrF	$^6\Sigma^+$	0.379	0.539	1.4	13.6	[123]
MnS	$^6\Sigma^+$	0.195	0.350	1.8	-2.4	[124]
CrCl	$^6\Sigma^+$	0.167	0.266	1.6	2.2	[123]
CrO	$^5\Pi$	0.524	1.148	2.2	10.5	[125]
CrN	$^4\Sigma^-$	0.624	2.611	4.2	7.0	[125]
VO	$^4\Sigma^-$	0.546	2.031	3.7	22.5	[126]
NbO	$^4\Sigma^-$	0.432	15.58	36	334.0	[127]
TiH	$^4\Phi$	5.362			182.3	[128]
NH	$^3\Sigma^-$	16.343	0.920	$5.6\ 10^{-2}$	54.7	[129]
O$_2$	$^3\Sigma^-$	1.438	1.985	1.4	-8.4	[130]
CaH	$^2\Sigma^+$	4.229			46.7	[131]
CaF	$^2\Sigma^+$	0.339			1.3	[97]

Table 2.1: Diatomic molecules with high-spin electronic ground states and their rotational constant (B), spin-spin interaction constant (λ_{ss}) and spin-rotation interaction constant (γ_{sr}). All numbers are given in cm^{-1}. The ratio of λ_{ss} over B is an indicator for the strength of Zeeman relaxation.

included: CaH, NH, CaF as well as the oxygen molecule (^{16}O^{18}O), a long time prime candidate. As a further restriction, only molecules that have been observed in experimental work and for which a rotational constant is experimentally determined, are included. A column is added with the ratio of the spin-spin interaction to the rotational constants, $|\lambda_{ss}/B|$, to guide the selection process in minimizing the expected effects of Zeeman relaxation.

An inspection of this table indicates that there are three molecules which clearly stand out in terms of expected stability against Zeeman relaxation: CrH in its $^6\Sigma^+$ ground state, MnH ($^7\Sigma^+$) and MnF ($^7\Sigma^+$).

All three molecules possess a large magnetic moment, which is nominally 5 and 6 μ_B, respectively. We disqualify the MnF molecule, as it has a substantially smaller rotational constant, which would result in level crossings between different rotational manifolds at fields lower than 0.25 T. One could argue that the TiH molecule also possesses a large magnetic moment and a rotational constant that should avoid these level crossings; however, it is believed that non-Σ state molecules are highly susceptible to Zeeman relaxation. The reason for this lies in the collision-induced precession of the non-zero orbital angular momentum, which in turn can cause a change in the Zeeman state via the spin-orbit coupling [95]. Since in addition no value of the spin-spin interaction constant could be found for TiH, it is left out of consideration.

Both CrH and MnH fulfill the requirements of a large rotational constant, a small spin-spin interaction constant while at the same time having a high-spin ground state which should be amenable for magnetic trapping. Both molecules were first observed in the 1930s by Gaydon and Pearse [132, 133]. CrH has attracted by far the most experimental attention as a prototype for high-spin diatomic molecules, especially since it was discovered in the emission spectra of L-type brown dwarfs [134]. Because of its high-spin ground state, CrH is employed as a probe for magnetic field strengths in sunspots [135]. For MnH, the experimental studies are more sparse, which is likely due to the highly complex structure of the spectroscopic transitions which are split into numerous hyperfine components. However, the ground and excited states are well characterized [136,137,138], and the ground state has been studied using ESR spectroscopy [139,140]. Based on the extensive experimental information available and the properties mentioned above, CrH and MnH radicals appear to be ideal candidates for a successful buffer-gas cooling and magnetic trapping experiment in our system.

Chapter 3

Experimental realization

3.1 Introduction

The experimental realization of buffer-gas cooling and subsequent magnetic trapping is technologically demanding. Reaching the temperature regime to which the particles have to be cooled in order to thermalize them below achievable trap depths involves state-of-the-art cryogenic techniques. In addition, exceptionally strong magnets have to be incorporated in the cryogenic system to produce the necessary trapping fields while offering optical access to the trapping center for detection of the particles. These challenges have been met with a standard dilution refrigerator unit attached to a custom-built helium cryostat that incorporates the magnetic system. The design is based on the experimental technology developed by John Doyle and co-workers in the Harvard group [141, 61, 60, 63].

This chapter starts with a description of the helium cryostat, followed by a brief introduction to the ^{3}He-^{4}He dilution unit. While the specific buffer-gas cells, as they are used in the experiments, will be described in the experimental chapters, the next section discusses their general properties and the design constraints imposed by the cryogenic system and the experimental demands. This is followed by a description of the magnet and the corresponding trapping field. The chapter closes with a

section on the performance of the parts forming our cryogenic system.

3.2 Cryogenic system

3.2.1 The helium cryostat

A scheme of the cryostat, including the dilution unit as well as the buffer-gas cell and the magnet, is depicted in Figure 3.1. The ^{4}He cryostat was custom-made (VOSKAM GmbH, Oldenburg, Germany) with an initial design goal of 72 h of continuous operation between two helium fills. It has a total height of ~ 240 cm and a maximum diameter of ~ 50 cm. To shield the dilution unit and the helium dewar from thermal radiation, the outer vacuum chamber (OVC) contains a liquid nitrogen (LN2) tank to which a copper shield is attached. The OVC is pumped with a turbo molecular pump (Pfeiffer Balzers TPH 060) backed by a rotary vane pump (Pfeiffer Balzers TPH 004 B).

The inner vacuum chamber (IVC) is surrounded by a 80 l volume liquid helium tank. Vapor-cooled radiation baffles in the upper helium dewar reduce the heat load on the liquid He bath and help to lower the helium consumption to a tolerable amount. All evaporating helium gas is transferred to a recovery system, where it is recycled and reliquified. The magnet, that needs to be cooled to 4 K for operation, is immersed in the liquid helium. Its clear bore ($\varnothing 76.5$ mm) forms a part of the outer wall of the IVC. This innermost part of the cryostat also contains the ^{3}He-^{4}He dilution unit of the refrigerator and can be evacuated using a Pfeiffer Vacuum pumping station (TSU 071). All room temperature vacuum parts are sealed using Viton o-rings, while flanges at cryogenic temperatures are sealed with indium.

Optical access to the trapping center is provided from six sides through windows sitting at different temperature stages in the system, namely room temperature (OVC), 77 K (LN2 shield) and 4 K (magnet). With a diameter of 3 inch, the largest aperture is provided from the bottom of the cryostat. On the same axis, but looking down from the top, a free port of 20 mm diameter offers additional access but was not used for the experiments described in this thesis. Due to mechanical stability restrictions in the magnet design, side access through the magnet support is

limited to openings of 10 mm diameter.

The whole cryostat is mounted in an aluminum rack (ITEM) that also holds a breadboard with detection optics. The vacuum vessels, and the copper parts necessary for radiation shielding are designed such that an assembly/disassembly of the cryostat can be done within this rack.

3.2.2 The ^{3}He-^{4}He dilution unit

The dilution unit, mounted within the IVC, is a standard Leiden Cryogenics Minikelvin 126-700 with customized apertures on the vertical optical axis to provide access from the top. Directly flanged to the top of the cryostat, a large turbomolecular pump (Pfeiffer Vacuum TMH 1600 MC) with magnetic bearing and a pumping speed of approximately 1600 l/s drives the gas mixture circulation for dilution refrigeration. The necessary backing pressure is provided with a helium-tight rotary vane pump (Pfeiffer Vacuum DUO 20).

Pumping on the 1K pot is done with a second rotary vane pump of the same type. During operation of the dilution unit, the 1 K vessel is continuously filled from the surrounding liquid ^{4}He tank through a needle valve (see Figure 3.1). To avoid the diffusion of oil into the cryostat and the helium recovery system, all rotary pumps are equipped with oil filters, both at the pumping line and the exhaust.

The flow of the ^{3}He-^{4}He gas mixture, pumped in a closed circuit through the system, is controlled with the help of a commercial Leiden Cryogenics gas handling system. To prevent clogging of the condensation capillaries by freezing impurities, the gas is passed through two liquid nitrogen traps to clean the circulating helium gas before sending it into the cryogenic system. Two capillaries of different diameter lead to the mixing chamber and can be switched for alternative or parallel use. When the dilution unit is not in operation, the ^{3}He rich and ^{4}He rich mixtures are held in separate dumps incorporated into the stainless steel hollow frame of the gas-handling system. The whole system has a specified cooling power of 700 μW at 120 mK and a base temperature of 8 mK.

^{3}He-^{4}He gas mixture
incondensation line

1K pot pump line

He tank
safety valve

^{3}He-^{4}He gas
circulation

vapor-cooled
radiation baffles

LN2 dewar

80 l He tank

OVC
pressure gauge

OVC
evacuation

1K pot
1K pot filling line
still

dilution refrigerator unit

IVC

bellow vessel

mixing chamber
cold plate

buffer gas cell
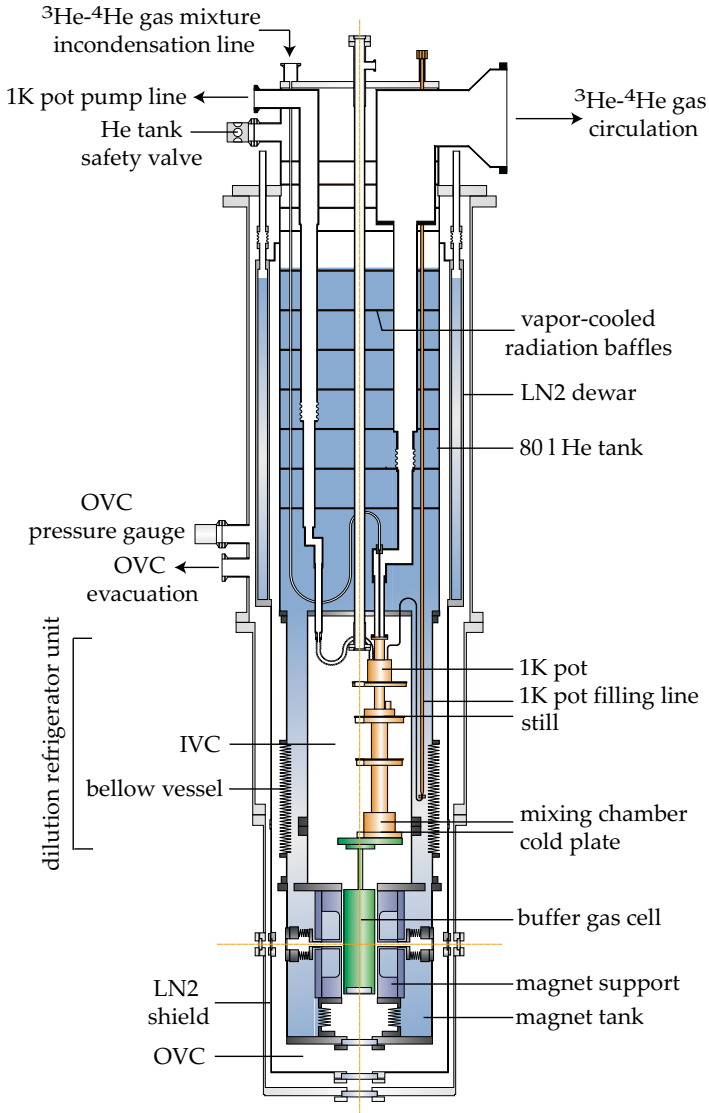
LN2
shield

magnet support
magnet tank

OVC

**Figure 3.1:** Scheme of the cryogenic system.

3.2.3 The buffer-gas cell

The experimental cell is the container for the helium buffer-gas and its shape and material properties determine the thermal anchoring of the gas atoms to the mixing unit of the refrigerator. Making it suitable for buffer-gas cooling and magnetic trapping implies material and design constraints.

First of all, to not interfere with the trapping field, the material should be non-magnetic. In addition, any temperature gradients, e.g. by the heat of an ablation pulse or a heating pulse from an incorporated resistive heater, should equilibrate as quickly as possible. This requires a high thermal conductivity of the material. On the other hand, the thermal contact to the cryostat cold plate has to be chosen with care to avoid excessive heating of the mixing chamber at higher cell temperatures while still allowing an efficient re-cooling.

For all the experiments described in this thesis, no quick magnetic field ramps where necessary. This allowed us to build the cell from oxygen-free high conductivity copper (OFHC) which is ideally suited for cryogenic experiments due to its giant thermal conductivity of 500 mW/cm·K and a specific heat as low as 0.1 mJ/mol·K. If such ramps had been necessary, induced eddy currents in the copper would have led to unacceptable heating of the cell. In this case, a cell constructed from insulating G-10 material can be used. To compensate its low thermal conductivity, one can make use of the ideally infinite thermal conductivity of superfluid ^{4}He II, which is filled into a double wall from a gold-plated and indium-sealed reservoir, attached to the mixing chamber. Here, a sinter provides a large surface area improving thermal contact, which otherwise would be inhibited by a large Kapitza boundary resistance. Such a cell was developed previously [89, 142] but has not been used in any of the experiments described in this thesis.

A scheme of all parts forming the buffer-gas cell, as it is attached to the cold plate, can be seen in Figure 3.2. For an optimum thermal connection to the refrigerator, the top part has a diameter that matches the bottom of the mixing unit. A well defined thermal impedance between the cell body and the cold plate is established by a rod of 15 mm diameter and a length of 140 mm, that allows for an efficient cooling of the cell while not overheating the mixing chamber; this part also forms
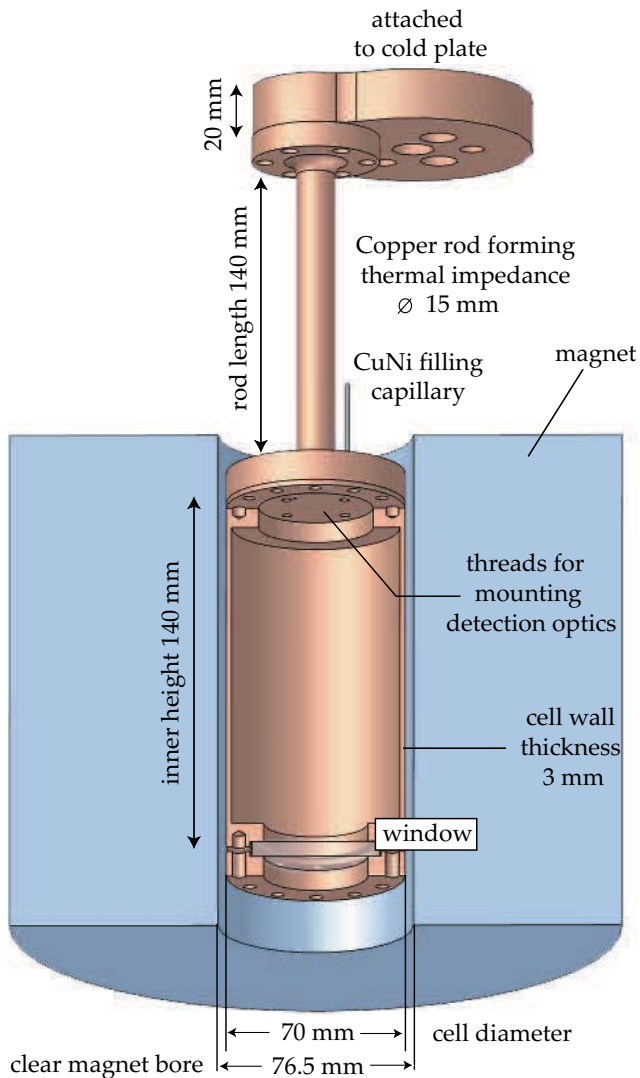
Figure 3.2: Scheme of the experimental cell within the magnet bore and attached to the cold plate of the refrigerator. For clearness, the brass screws used for sealing, have been omitted.

the top wall of the cell. The main part of the copper cell is formed by a cylinder with a length of 140 mm and a wall thickness of 3 mm; it is closed at the bottom by a copper window mount containing a 2 inch diameter window. All parts of the cell are sealed using indium and fastening is done using Helicoil threads and brass screws. The top wall of the cell contains mounts for reflective detection optics, as well as space for sample targets The specific cells and detection schemes used in the actual experiments are described in the experimental sections. All cells can be heated by a 200 Ω resistor epoxied into the copper cell body. An embedded 1 kΩ ruthenium oxide (ROX) sensor is used to measure the cell temperature. Helium buffer-gas can be filled using a CuNi filling capillary, that is thermally anchored at the dilution unit and connects to a small volume ($\sim 0.3\,$l) outside the cryostat. To add a specified amount of helium, this volume is filled with gas of a certain pressure, that is subsequently transferred into the cell.

3.2.4 Thermometry

Information on the temperatures of the inner parts of the cryogenic system is crucial for trouble-shooting and optimization of the cooling power of the system. Therefore, the following parts within the IVC are equipped with temperature sensors (from bottom to top of the cryogenic system): copper cell, mixing chamber, still, 1K pot and the bottom of the helium tank. In addition, the OVC is equipped with sensors at the magnet tank and at the LN2 copper shield.

   All temperature sensors are monitored throughout, using either platinum resistors (Pt-100) or ruthenium oxide sensors (LakeShore RX-102A) of different resistances (1 kΩ, 2 kΩ and 10 kΩ). While Pt-100s can be individually calibrated down to the boiling point of liquid helium at 4.2 K, the ruthenium oxide sensors provide superior sensitivity from 40 K to below 50 mK, so that the total range of interest is covered. Both types are negligibly affected by the presence of a magnetic field. The sensors are read out by an AC resistance bridge (Picowatt AVS-47) with a four-terminal measurement at typical excitation voltages of 300 μV or less. The resistance bridge is controlled via GPIB by a Labview program that converts the resistance readings into temperature. A prerequisite for reliable temperature readings is a thorough thermal anchoring of the

sensor to the object of interest. Thermal equilibrium between the two is largely improved by using a piece of copper into which the sensor is glued using epoxy. This assembly is then attached to the object with a brass screw. The electrical connection to the outside world of the cryostat is established with Constantan wire. To minimize heat transfer to the cryogenic parts, the wires are twisted and thermally anchored to all stages at higher temperature. For example, the leads to the copper cell sensor are connected to the 4 K, 1K, and additionally at the still and the mixing unit.

### 3.2.5 Magnetic quadrupole trap

The magnetic quadrupole trap is generated by two coils in anti-Helmholtz configuration. The fields created by the coils cancel in the center, creating a field minimum in space that can be used to trap paramagnetic particles. The actual coil arrangement, summarized in Table 3.1, determines all geometrical properties of the resulting field. The coils have been custom-made by American Magnetics from NbTi wire ($\varnothing$ 0.48 mm), embedded in high thermal conductivity epoxy to prevent wire motion induced by the Lorentz force in operation.

Coil arrangement	
Inner coil radius	42.34 mm
Outer coil radius	73.34 mm
Coil separation	23.98 mm
Coil height	50.70 mm
Number of turns	8241.5
Estimated inductance	9.8 H

**Table 3.1:** Configuration of the quadrupole coils and specifications of the magnet.

Since the two field generating currents flow in opposite directions, the coils of a quadrupole magnet repel each other with a substantial force. From a finite elements analysis we know that forces on the order of 100 kN have to be compensated at typical fields necessary in the experiments [142]. The magnet support therefore has a vital role, since mechanical

failure would pose a threat both to technical equipment as well as human health. It consists of a special titanium alloy (Ti-5Al-2.5Sn) which is non-magnetic, exceptionally robust and non superconducting at cryogenic temperatures. Optical side access to the trapping center is provided via 10 mm diameter holes in the mandrel structure [142]. The concept follows a working prototype of the Harvard group [89, 143] and has been aimed at generating trapping fields of up to 4 T, which roughly represents the present limit of technical feasibility.
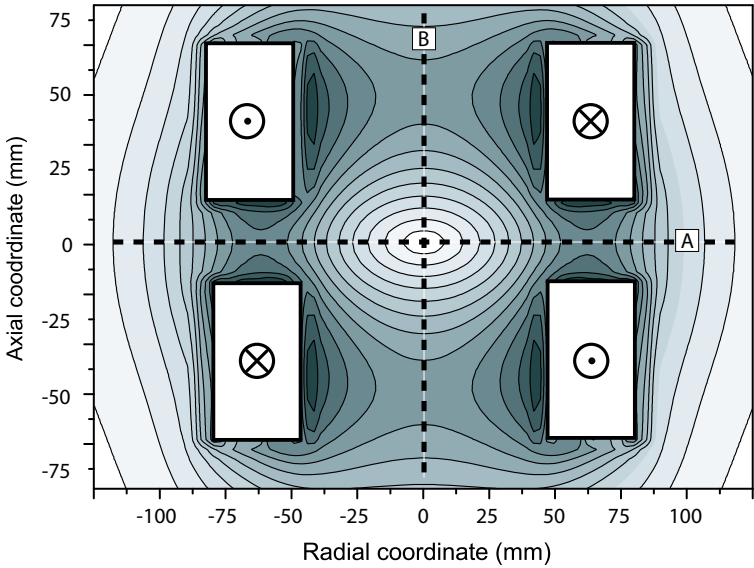
Figure 3.3: Cylindrical symmetric trapping field, produced by two coils in the arrangement of our setup. A and B represent the lines along which the magnetic fields are plotted in Figure 3.4.

Figure 3.3 shows a plot of the field lines of the cylindrically symmetric field. It has been calculated by numerically integrating over Biot-Savart's law using the geometrical coil arrangement, depicted in Table 3.1. Since the fields are proportional to the current running through the magnet, the values are given in mT/A. As already mentioned in Section 2.3, one
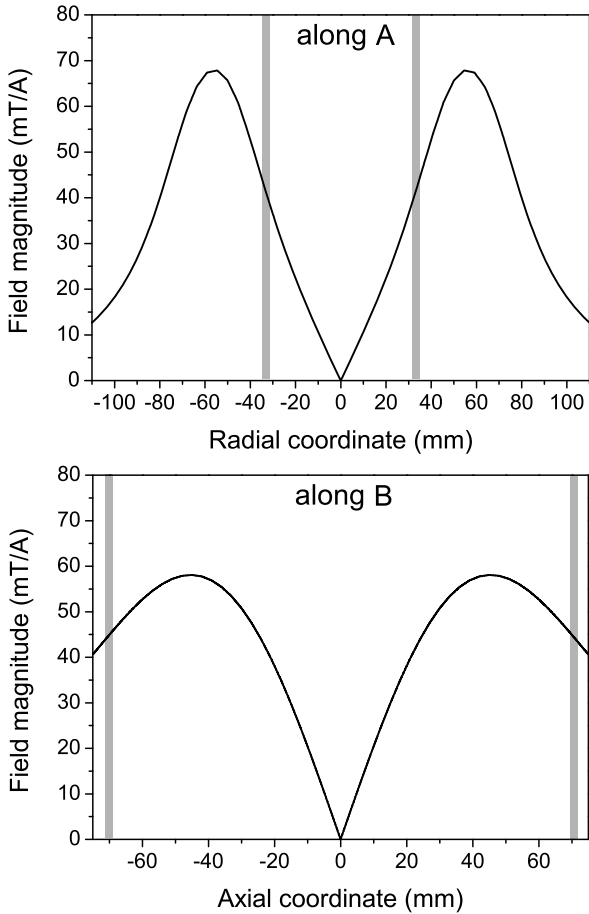
Figure 3.4: Plots of the magnetic field along the dashed lines of Figure 3.3 for a current of 1 A. The grey lines indicate the cell boundaries.

can take advantage of $|B_{max}(\text{axial})|$ to confine particles in axial direction. Radially, however, the trap depth will usually be limited by the position of the inner wall of the buffer-gas cell (see Figures 3.4 and 2.6). The field maxima, confining particles along the dashed lines going through the trapping center in Figure 3.3 are

$$|B_{max}(\text{radial})| = 36.3\,\text{mT/A} \ \text{ at } \rho = 30.0\,\text{mm}, z = 0.0\,\text{mm} \qquad (3.1)$$

$$|B_{max}(\text{axial})| = 58.8\,\text{mT/A} \ \text{ at } \rho = 0\,\text{mm}, z = 45.4\,\text{mm} \qquad (3.2)$$

Close to the center, the magnetic field is asymptotically linear, with magnetic field gradients in radial and axial direction given by

$$|\nabla B_{radial}| = 11.5\,\frac{\text{mT}}{\text{cm} \cdot \text{A}} \qquad (3.3)$$

$$|\nabla B_{axial}| = 22.9\,\frac{\text{mT}}{\text{cm} \cdot \text{A}} \qquad (3.4)$$

With a targeted operating current of 75 A, the resulting characteristic field strengths of this magnet are extraordinarily high when compared to standard magnetic traps in experiments using MOTs, for example.

The performance of any superconducting magnet is limited to conditions under which the superconductivity in the coil wires does not break down. A break-down will ultimately happen when the magnet current or the external field exceeds the critical values of the wire material. More commonly, however, frictional heating from small movements of the coil wires due to the Lorentz force can cause a breakdown of superconductivity. In the case of such an event, called a *quench*, the enormous energy stored in the magnetic field has to be safely extracted from the magnet. A lot of it will be converted into heat and cause evaporation of large amounts of liquid helium. A quench therefore is an event to be avoided, putting high demands on the cryogenic system, the magnet, and its power supply. A special quench-protected 4-quadrant power supply (Oxford IPS120-20) is used here. It provides a maximum of ± 120 A at ± 20 V and allows automated sweeping of the magnet current.

The limiting quench current can be successively increased upon re-energizing the magnet several times, causing the wires to gradually

move to more optimal positions. Unfortunately, this training has to be repeated whenever the magnet has been brought to room temperature. Electrical connection between the power supply and the magnet is established with 58 cm long helium-vapor-cooled current leads (AMI 50A/75A) and 1.5 m long superconducting bus bars (AMI BB-75-S). To reduce the helium consumption when the magnet is not in use, the current leads are equipped with a breakaway option.

3.3 System performance

Cooling power of the dilution unit

We found that the cooling power of the dilution unit was never up to the specifications for all experiments described in this thesis. My predecessors on this project were able to reach a base temperature of 20 mK and measured a cooling power of 100 μW at 100 mK [142]. This is in agreement with the specs (700 μW at 120 mK, base temperature: 8 mK), considering that the implementation of a large surface copper cell and optical access increases the heat load on the mixing chamber. In addition, the specs of the dilution unit are given for the case a turbo molecular pump with a pumping speed of 2000 l/s is used for the circulation of the ^{3}He-^{4}He gas mixture, whereas ours has a lower pumping speed of only 1600 l/s. However, in the configuration of my predecessors we measured a cooling power of 100 μW at a much higher temperature of 300 mK. Since the cooling power in a dilution refrigerator drops quadratically with the temperature [100], this is almost a factor of 10 worse.

As a possible cause for this, we suspect a small leak in the heat exchangers, where the gas mixture flowing towards the mixing unit is pre-cooled by the ^{3}He on the way to the still, to reduce the gas flow through our system. Since the cooling power depends on the flow of the ^{3}He-^{4}He gas mixture, this can be a problem. Although a larger cooling power would have enabled us to measure at a higher repetition rate, the actual cooling power available is sufficient for the described experiments.

Helium consumption

The cryostat serves as the precooling stage for the dilution unit. In operation, it constantly consumes a significant amount of liquid helium that frequently has to be refilled. Such a refill can be done within ~ 1.5 h, however, measuring during this time is difficult. For this reason and because liquid helium is expensive, the consumption should be as low as possible.

The liquid level in the ^{4}He dewar surrounding the IVC can be measured with two level sensors that consist of superconducting NbTi wires of different length. A short sensor (280 mm) covers the magnet tank, and a long sensor (1350 mm) - starting above the small one - reaches all the way to the top of the dewar. A Labview-controlled readout unit (AMI Model 135) measures the resistance of the wire parts above the helium level (and thus not superconducting) and converts this value into a height.
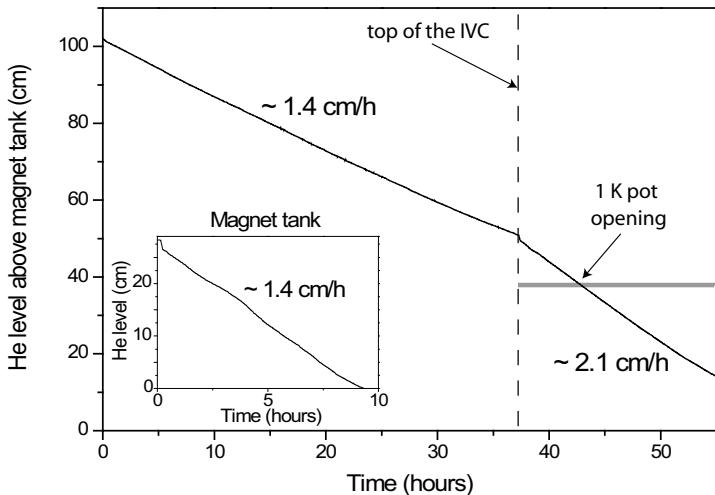
Figure 3.5: Helium level above the magnet tank versus time for detached magnet current leads. The inset shows the helium level versus time in the upper domain of the magnet tank.

Figure 3.5 shows a plot of the He level as a function of time for the case of detached current leads. The part left of the dashed line shows the level in the tank above the top of the IVC. This part is larger as the IVC takes a substantial volume of the ^{4}He dewar (see Figure 3.1). Clearly, this volume difference is reflected in a higher drop rate of the helium level below the IVC top, represented by the part right of the dashed line in Figure 3.5. The amount of evaporated liquid helium per hour, however, is the same in both volumes ($\sim 1.2\,l/h$). In the original configuration of the cryostat this rate was about twice as high, mainly caused by the height of the busbars. Initially, these were mounted 40 cm from the top plate in the He dewar (below the first two radiation baffles, see Figure 3.1). In a retrofit of the cryostat they have been lowered to 70 cm (below five radiation baffles). At this height, the top of the copper busbars experience a colder environment and thus less heat is transferred to the liquid helium bath via the copper busbar material. The inset of Figure 3.5 shows the liquid helium level as function of time in the magnet tank. In this part of the dewar, the lowest helium evaporation rate is found.

When the dilution unit is operating, the 1 K pot constantly needs to be refilled from the He tank. This means that the helium level has to be kept above a certain height to avoid evaporation of the liquid helium in the transfer line from the dewar towards the 1 K pot. As a consequence, a full He tank allows operation for about 40 hours without the need for refilling. Unfortunately, a lot of heat gets transferred to the dewar whenever the magnet is connected to its power supply via the copper busbars, sitting in the helium tank. If the magnet is frequently in use, we have to fill a 100 l can of helium per day.

Magnet performance

The original magnet current specs of 75 A has never been reached. Quenches of the magnet at much lower currents of ~ 45 A unfortunately limit the field strength of the system to about 1.6 T at the cell boundaries in radial direction. We can only speculate that imperfections in the epoxy material, used to prevent the wires from moving, leads to a larger motion of the wire material and a quench.

In addition, the magnet system seems to have degraded over time.

While a current of 40 A could be reached without quenching at the start of this project, we had to train it by forced quenching (see Section 3.2.5) to reach this value at the end of the experiments. Still, a more than sufficient trap depth of several Kelvins is obtained for all species under study in this thesis.

Chapter 4

Buffer-gas cooling and magnetic trapping of atomic chromium

4.1 Introduction

To become acquainted with the cryogenic system and the difficulties of buffer-gas cooling and magnetic trapping we start with experiments on a well known species that serves as a test candidate for our experimental infrastructure. Cr is chosen, as it has a large magnetic moment of 6 μ_B and strong, well-characterized electronic transitions suitable for detection using absorption spectroscopy. Moreover, the most abundant isotope ^{52}Cr (86 %) has zero nuclear spin, which considerably simplifies the spectrum. Cr was one of the first atoms to be magnetically trapped using buffer-gas cooling by Doyle and co-workers [60]. For all these reasons, Cr atoms serve as the ideal candidate to test the performance of our cryogenic cooling and trapping system.

This chapter starts with a brief description of our experimental setup

and of the detection scheme that we have used for monitoring the chromium atoms within the trap. This is followed by a discussion of the experimental chromium data. Number densities and temperature information are extracted from the recorded absorption spectra, using a numerical spectrum simulation that is compared to the measurements. This information is used for the interpretation of the cooling and trapping dynamics of the atom ensemble. Probing the atoms by direct imaging of the Cr cloud onto a CCD chip adds insight about the spatial distribution of the trapped atom cloud.

4.2 Experimental

The experiment is done in the cryogenic setup described in detail in Section 3; a scheme is shown in Figure 4.1. The right side of that figure shows a cut through the buffer-gas cell body built from high thermal conductivity copper. Its design details are described in Section 3.2.3 and only a brief overview of the properties of the experimental cell shall be given here. It is positioned in the center of the magnet bore and linked to the cryostat by a copper rod, forming a well-defined thermal impedance. Optical access is provided by a 50 mm diameter window sealing the bottom. A buffer-gas fill line is implemented using a CuNi capillary. Finally, the cell is equipped with RuO thermistors and a resistive heater for temperature monitoring and control.

A Q-switched pulsed Nd:YAG laser (Continuum Minilite-II) is used to generate 10 Hz laser pulses of the second harmonic with 532 nm, that we use for ablation. Pulses with an energy of ~ 12 mJ and a duration of ~ 10 ns are loosely focused (lens f: 750 mm) onto the solid chromium targets, glued to the top of the buffer-gas cell. In order to avoid power fluctuations, the laser is running at a 10 Hz repetition rate and single ablation pulses are selected by opening a shutter in the beam path. The number of atoms that are evaporated from the chip surface and subsequently enters the probing region is sufficiently large to allow for detection via absorption, a method that is particularly well suited for extracting density information of the investigated species.

Figure 4.2 depicts a scheme of the energy levels, used for detection of the Cr atoms. We monitor the amount of absorbed light when excit-
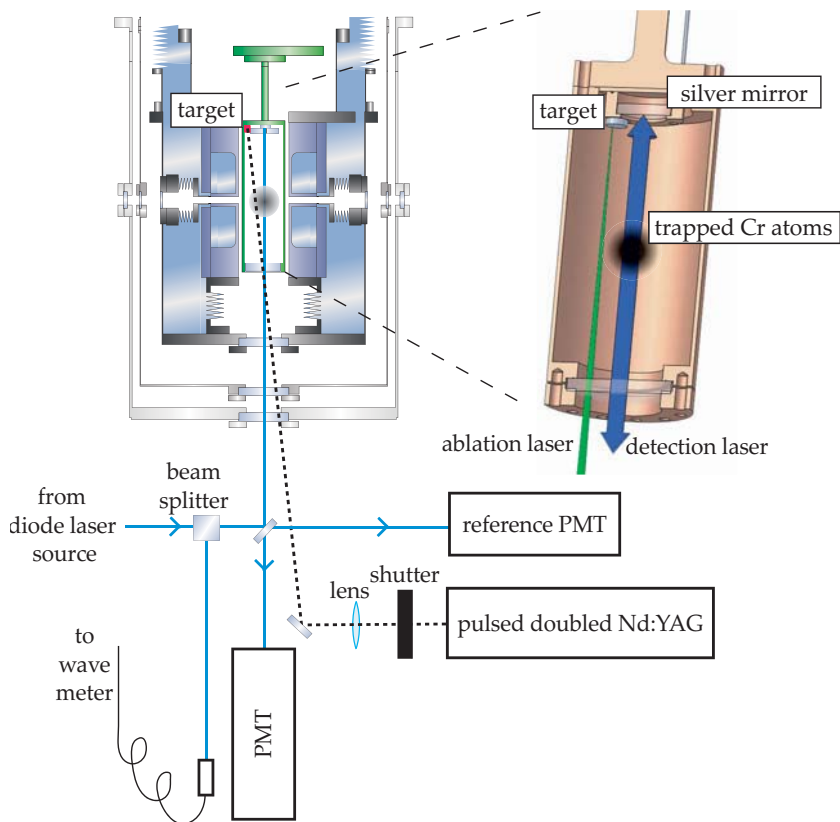
Figure 4.1: *Left*: Scheme of the detection setup. Cr atoms are produced via laser ablation using a pulsed Nd:YAG laser (dotted line). Subsequently, they are probed by a cw diode laser that is retroreflected by a silver mirror. A lens system guides the light onto the PMT cathode, where the amount of absorbed light is measured with respect to a reference PMT.
Right: An artist's impression of the buffer-gas cell.

ing from the $m_J = +3$ sublevel of the ground state, resonant with the $a^7S_3(m_J = +3) \rightarrow z^7P_4(m_J = +4)$ transition around 425 nm. This is a nearly closed transition, where almost all excited Cr atoms decay back into the initial state (leakage $\sim 10^{-6}$). The light is generated by frequency doubling the output of a grating-stabilized diode laser (Toptica DL100) at 850 nm in a $KNbO_3$ crystal within an external bow-tie cavity. The cavity is actively locked to the diode laser using a Pound-Drever-Hall scheme [144]. On long timescales, the cavity length is adjusted piezo-electrically to match the laser frequency; on short time scales, the frequency of the diode laser is adjusted to match the cavity length by modulating the diode current. It must be stressed that the laser is not frequency-locked to an external reference, so that long-term frequency drifts can occur. The frequency-doubled light is amplitude stabilized by an acousto-optic modulator (AOM), spatially filtered, expanded and (optionally) sent through an aperture, defining a beam diameter of a few mm.

As indicated in Figure 4.1, this beam is then sent into the cell using a beam splitter and retroreflected by a mirror mounted at the top of the cell. For these experiments, only the windows that give access from the bottom of the cell are implemented, and to minimize optical etaloning effects all windows are wedged by $\sim 1^o$ and anti-reflection (AR) coated for the wavelengths used in the experiment. Light exiting the cell is directed onto a photomultiplier tube (PMT, Electron Tubes 9813QB). A fraction of the light that is not entering the cryostat, is directed onto a second PMT (Electron Tubes 9814QB) for normalization and correction of residual intensity fluctuations. Typical light powers used are less than $1~\mu$W, in order to avoid both heating of the cell and loss of atoms due to optical pumping effects. The measured transmission is thus obtained by normalizing the detection signal on the reference signal from the second PMT. When the detection laser is scanned in frequency, the signal is corrected for etaloning effects by recording a background transmission signal on which the signal is normalized. In an alternative detection scheme, the transmitted beam is directly steered onto the light-sensitive chip of a CCD camera (PCO Imaging, Sensicam SuperVGA).
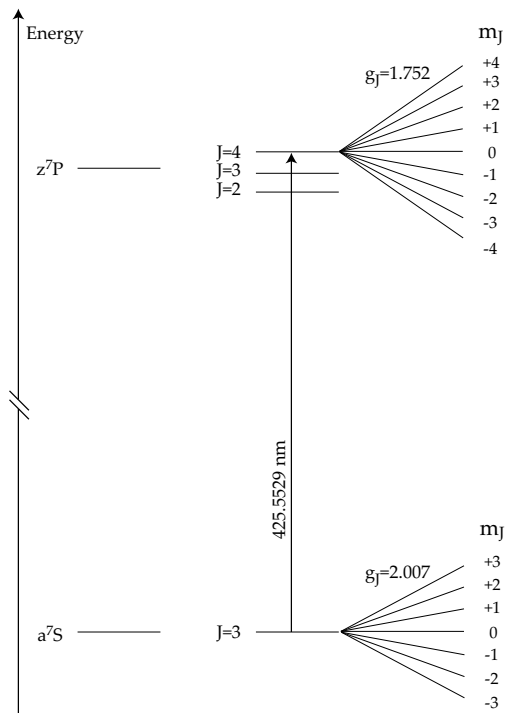
Figure 4.2: Level scheme used for detection. We monitor the amount of absorbed light when exciting from the $m_J = +3$ sublevel of the ground state, resonant with the $a^7S_3(m_J = +3) \rightarrow z^7P_4(m_J = +4)$ transition around 425 nm.

4.3 Magnetic trapping of Cr

Figure 4.4 depicts a typical recorded transmission trace spanning a time period of 1 minute. In this experiment, starting at t=-3.5 s, the cell is heated for a period of 3 s with a heating power of $\sim$ 20 mW. Then, at t=0 s, the ablation laser (15 mJ) is fired to inject Cr atoms into the ^{4}He vapor. The optimal loading conditions are found in a procedure where the heating power and ablation are optimized to yield the best capture efficiencies. A field-free measurement under the same conditions suggests that the heating over a few seconds ensures a full evaporation of the helium off the cell wall, whereas the short waiting period allows for the buffer gas to be cooled somewhat without noticeable cryopumping effects taking place. The 15 mJ used for the ablation is a compromise between signal intensity and the temperature at which the atoms are captured in the trap.

To give an idea on how the ablation laser heats the cell and the times necessary for cooling it down again, Figure 4.3 shows a plot of the cell temperature versus time for 3 ablation pulses with an energy of 15 mJ. In contrast to the procedure mentioned above, this curve, however, was recorded without additional heating prior to ablation.

The trace shown in Figure 4.4 is recorded by repeatedly scanning the probe laser frequency over a range of $\sim$ 10 GHz to obtain a magnetic-field broadened absorption line while minimizing the effect of long term drifts of the laser wavelength. In the scanned signal, some interesting dynamics can be observed. In the initial few seconds after ablation, the strong absorption signal first decreases, then shortly grows again and finally decays slowly. Additionally, a rapid narrowing of the line profile can be seen during the first 5 seconds following ablation. These different regimes will be discussed in detail below.

More detailed information about the density and temperature evolution of the trapped atom ensemble can be obtained by simulating the spectra and comparing them to the recorded ones. First we note that at temperatures below 1 K the expected Doppler broadening is less than 100 MHz, which is negligible in comparison with the observed Zeeman broadened linewidths of 1 GHz and larger.

For the modelling, it is assumed that the cloud of atoms is in thermal equilibrium and can be characterized by a Boltzmann temperature [145].
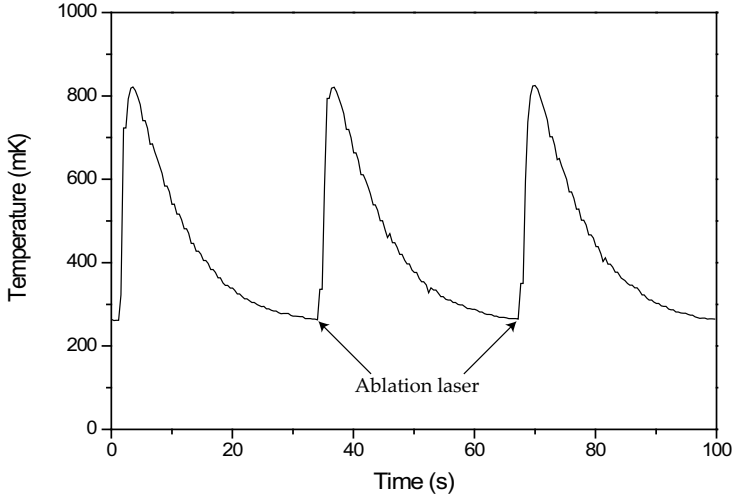
Figure 4.3: A plot of the cell temperature versus time for several 15 mJ ablation laser pulses.

For any given point in the trapping field, the Zeeman shifted transition frequency and a (relative) population density and a resulting absorption cross-section are calculated. A transmission spectrum is obtained by numerically integrating the absorption over the volume defined by the probe beam. The details of this numerical program are explained in the Appendix A. From the inset in Figure 4.4 it can be seen that the simulated spectrum is in excellent agreement with the recorded data.

The simulations show that the spectral shape strongly depends on the probe beam parameters and we have thus carefully measured beam diameter and intensity profile. However, the relative position of the probe beam with respect to the center of the magnetic quadrupole trap is less amenable to direct measurements and must therefore be included in the model. This relative position is especially important when the probe beam is linearly polarized, as the projection of the driving E-field onto the quantization axis of the atoms, the inhomogeneous magnetic field, has a strong angular dependence. It can be shown that the angular
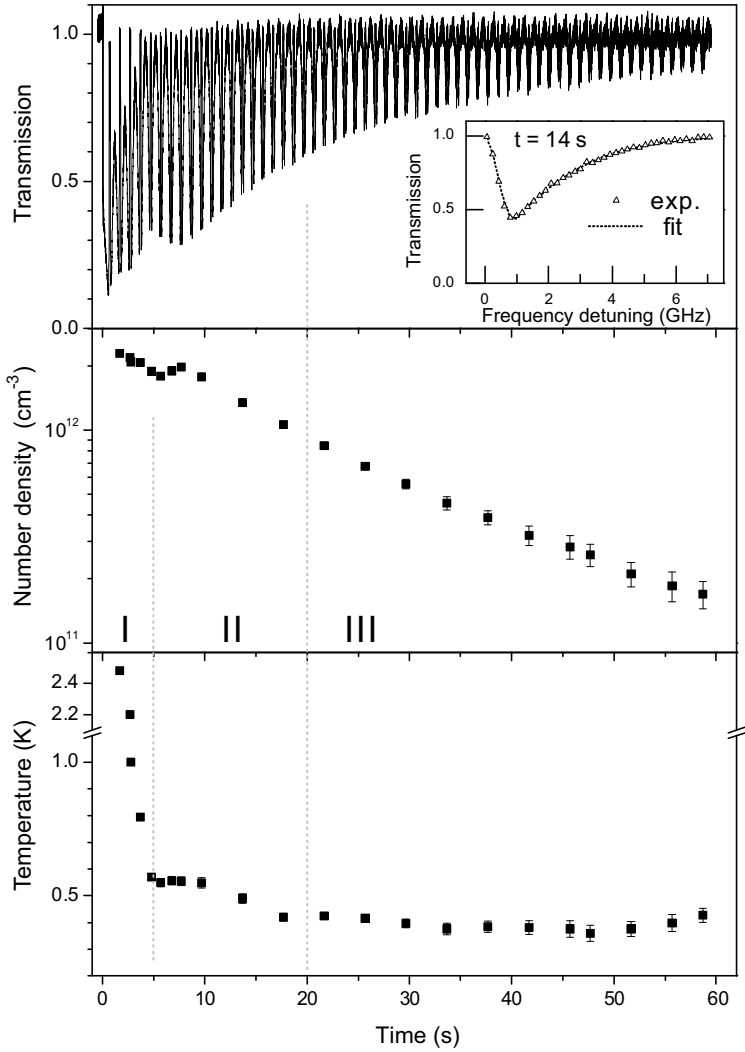
Figure 4.4: (Figure see previous page) Transmission through a sample of Cr atoms in the buffer-gas cell (top graph). The probe laser frequency is scanned repeatedly over the atomic transition with a repetition rate of 1 Hz. The inset shows a typical absorption profile (dots) after $\sim$ 14 s, together with a simulation (solid line). The other two graphs show the evolution of the particle density (middle) and temperature (bottom graph) of the trapped atom ensemble over time.

dependence of the absorption coefficient is $(\cos^2\theta + \sin^2\theta\sin^2\phi)$, where θ is the angle between magnetic field and light propagation axis, and ϕ that between polarization direction and magnetic field, respectively. The derivation of this expression can be found in the Appendix A. To the best of our knowledge, this full angular dependence has not been implemented in modeling of data in previous buffer-gas loading experiments. Best agreement is obtained when it is assumed that our 2 mm diameter beam is offset by 0.3 mm from the trap center, which appears very reasonable. The remaining free parameters used in the simulations are the particle density at the trap center and the Boltzmann temperature, which are found using a least-squares fitting procedure.

A possible error in the parameters obtained this way arises from a breakdown of the assumption of thermal equilibrium. This is likely the case at times shortly after the ablation pulse, where the changes in temperature are on comparable time scales as the time it takes to record one spectral profile. For this reason, the temperatures and densities obtained before t=5 seconds are given without error bars and should be considered as indicative only. Additionally, long-term drifts in the laser frequency could amount to errors of a few %. The densities and temperatures of the sample as obtained from the spectral simulations are depicted in the lower two graphs in Figure 4.4. The size of the error bars reflects the reduced signal-to-noise level at later times, when absorption signals become less pronounced.

Data at short times after ablation have not been published by Doyle and co-workers previously and it is interesting to speculate on the nature of the observed dynamics. The time evolution can roughly be divided into three periods which are indicated by I, II and III in Figure 4.4. During period I, the temperature falls rapidly from $\sim$ 1.5 K at t=2

s to some 500 mK after 5 s. This is attributed to so-called spilling effects, where during trap loading the warmest particles are lost over the trap edge. As a result the overall temperature drops. However, this temperature drop happens on a timescale of seconds, in contrast to the thermalization time of < 1 ms, estimated in Section 2.6.2. We attribute this to the breakdown of the assumption of thermal equilibrium within the first seconds after the ablation pulse, as mentioned above.

In Period II, the sample temperature does not change as dramatically as in Period I. The sample appears to be in thermal equilibrium as it has a temperature similar to that of the cell wall. The obvious *recurrence* in the transmission spectrum after 5 s is also observed in the density. The increase in the density is interpreted as a net diffusion of cooled atoms into the trap center.

After ~ 20 s, the temperature of the cell wall (not shown) has dropped to around 350 mK and the gas-phase helium within the cell is now cryopumped to the cell wall. As a consequence the sample now becomes thermally isolated and the temperature of the trapped cloud is no longer decreasing. Its final temperature thus corresponds to the cell temperature at the time of thermal disconnect.

At times later than 20 s, a clear continuous loss of Cr is observed. It is not expected that evaporation plays a large role at this point, as the effective trap depth at these temperatures is very large and evaporation rates are expected to decrease exponentially with effective trap depth [90]. A further indication for this is that the observed temperatures do not change, which rules out effective evaporative cooling. As additionally the buffer gas temperature is similar to or lower than the Cr temperature, we can thus rule out elastic collisions as a loss mechanism.

As a consequence, the observed trap loss must be due to inelastic collisions, which change the spin of the atom. Several such processes are known and they can be distinguished by the number of Cr atoms involved. The dominant loss mechanism may be found by fitting functional forms to the number density evolution. In an earlier set of data recorded over 180 s (where the signal was noisier and thus less suitable for quantitative data analysis) a clear signature is found of two-body loss processes, i.e. collisions in which two Cr atoms are involved. For the data presented in Figure 4.4, the signature of two body loss processes cannot
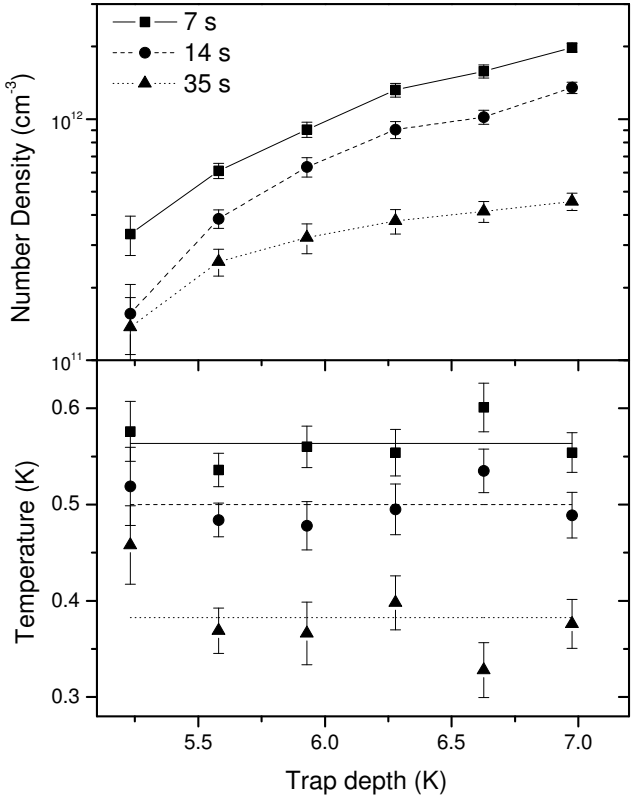
Figure 4.5: Density (upper graph) and temperature (lower graph) of a trapped cloud of Cr atoms as a function of trap depth, measured at three different times; at t=7 s (squares), t=14 s (circles) and 35 s (triangles) after ablation. The lines in the upper graph are guides to the eye, whereas in the bottom graph they represent the average temperature.

be easily distinguished from that due to collisions with background gas. If we leave one-body decay out of consideration, we obtain a maximum value for the two-body inelastic collision cross-section of $6 \cdot 10^{-13}$ cm^2 at $T = 350$ mK , consistent with a previous measurement [146].

To investigate the potential of this system for future experiments on the buffer gas cooling and trapping of molecular species, it is of interest to evaluate the trapping efficiencies at lower trap depths. Such a measurement is performed by lowering the current through the two anti-Helmholtz coils. The results of these tests are depicted in Figure 4.5 where the observed number densities and temperatures of a trapped Cr cloud, evaluated at three different times, are shown as a function of trap depth. Each value is obtained by averaging over several measurements. The trends that can be seen from these graphs are clear: a lower trap depth leads to a substantial drop in the number of captured atoms. The temperature of the trapped atoms is independent of trap depth. It seems thus obvious that a shallower trap captures less particles, while the temperature behavior gives us supporting evidence that no evaporative cooling, and thus no evaporation takes place. It is obvious from this figure that if a molecule were to be trapped, it should possess a large enough magnetic moment to allow for a trap depth of at least 5 K. Both CrH and MnH molecules fulfill this condition.

Absorption Imaging

In the measurements presented above, the probe laser diameter is limited to ~ 2 mm and is aligned close to the trap center. This way not the whole trapping volume is addressed. In an alternative experimental configuration, the full waist of the collimated probe beam is sent through the trap center, retroreflected and steered directly onto the light-sensitive element of a CCD camera. For these imaging experiments the laser frequency is kept at a fixed value. Since the atomic resonance frequency is determined by the field-dependent Zeeman shift, a fixed frequency experiment selectively probes for atoms in specific 'shells' within the trapping volume. The results of these measurements are depicted in Figure 4.6 for three probe laser frequencies and three different times at the maximum trap depth of 6.8 Kelvin. The images shown (1 second gate time) are obtained as the ratio of an image recorded with Cr in the trap and

one where no Cr is in the system. The size of the images is 8.6 mm (horizontal axis) by 6.9 mm (vertical). Since the beam is collimated, the spatial extent of the absorption signal on the CCD element has a 1:1 correspondence to the trapped cloud size.
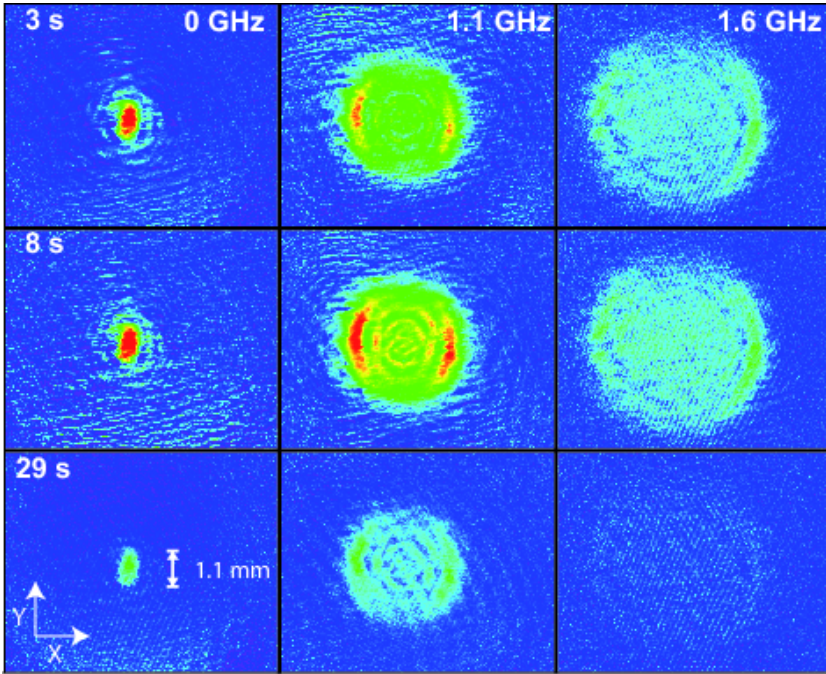
Figure 4.6: Absorption images of a trapped cloud of Cr atoms, at three different times (rows) and at three different laser frequencies (columns). The size of the image is 8.6 mm x 6.9 mm.

The first set of images is recorded at the frequency of the field-free atomic transition. A strong absorption signal is clearly visible at the trap center. One can see that the absorption is anisotropic, which is a manifestation of the use of linearly polarized probe light. When the probe laser is tuned towards higher frequencies, a ring structure becomes apparent in the images. Here, it is obvious that the angular

intensity distribution can be described by $\sin^2 \phi$, as discussed above. At a frequency-offset of $+1.1$ GHz, the strongest absorption is observed in a ring with a radius of ~ 1.5 mm. The reason for such a pronounced ring is that the probe beam line-of-sight here coincides with a 'shell' of Cr atoms trapped at the same field magnitude. Again, the asymmetry attributed to the laser polarization is clearly visible. The ring structure allows for a consistency check of our trapping field calculations. If we assume that the probe beam is collimated well, this implies that at a radius of 1.5 mm the magnetic field calculated from the Zeeman shift $\Delta\nu = B\mu_B(g_f m_{J,f} - g_i m_{J,i})/h$ is 76 mT. This is indeed consistent with our trapping field calculations (69 mT at 1.5 mm), used in the spectral simulations described earlier.

Apart from this strong outer ring of absorption, some weaker but still pronounced rings are also visible. The origin of these rings is unknown to us. It is unlikely that they are due to population in lower m_J states, as they persist for tens of seconds and it is expected that population in lower m_J states is lost more quickly than in the $m_J = +3$ state due to a combination of lower trap depth and spin-exchange collisions. It can be speculated that they are caused by diffraction of the beam by the dense atomic cloud in the trap center. It is, however, unfortunately not straightforward to simulate this diffraction pattern due to our probe geometry where the probe beam passes the trapped cloud twice. Without diffractive effects included, a semi-quantitative agreement between our simulated data and the images is found. We therefore do not extract temperature and density information out of these images. For the absorption measurements where only a small probe beam is steered through the center of the cloud, such diffractive effects are not expected to play an important role as the cloud size is larger than the beamsize, and the sensitive area of the PMT is significantly larger than the probe beam diameter.

4.4 Conclusions

Buffer-gas loading of paramagnetic species into a magnetic trap has successfully been demonstrated in our system. In the experiments, Cr atoms are confined with storage times of more than one minute. The use of an

absorption based detection scheme combined with a simulation of the absorption properties of the cloud in the presence of the inhomogeneous magnetic trapping field allows for extraction of important parameters that give insight into the dynamics of the buffer gas cooling and trapping processes. Thermal contact between the trapped cloud and the walls of the experimental cell is reliably broken after a period of 20 s. The final temperatures of ~ 350 mK that are reached are determined by the temperature of the buffer gas at thermal disconnect. Observed initial number densities exceed 10^{12} per cm^3. We have also succeeded in implementing continuous non-destructive absorption imaging of the trapped cloud, which can provide complementary information on temperature and internal state distribution over the whole trapping volume.

Chapter 5

Numerical simulation of the cooling and trapping dynamics

5.1   Introduction

In this chapter the numerical simulation used to describe cooling and trapping in our system, is specified. This simulation is used for extraction of the inelastic collision cross sections of MnH and CrH molecules in the next chapter. In addition, it serves as a tool to give deeper insight into the dynamics of buffer-gas cooling in conjunction with magnetic trapping.

Although a simple analytical model can be used to extract physical properties like the elastic-to-inelastic scattering ratio, such a model suffers from some deficiencies. Based on the description of the diffusion of one gas through another (for a detailed treatment of this see [147]), such a model is only valid in the limit of high buffer-gas densities and large ratio between the trap depth and the temperature of the particles η. Moreover, including a realistic, non-spherical, magnetic trapping field in the analytical approach is difficult.

To overcome these limitations and to have the possibility to study different inelastic scattering models, we set up a Monte Carlo simulation of the buffer-gas loading and trapping process. The basic idea of this approach is to track the trajectories of an ensemble of molecules through a gas of Helium atoms under different experimental conditions.

This chapter starts with a general description of the features of the numerical simulation. Subsequently, the elastic and inelastic collision subroutines, vital for describing cooling and trapping of the molecules, are elaborated. This is followed by a brief section on the optimization of the computational time of the simulation. At the end of this chapter, we test this program by reproducing data of the Harvard group, where NH molecules have been buffer-gas cooled and subsequently magnetically trapped [80].

5.2   General features of the simulation

In this simulation, molecules are generated randomly in a certain volume given by the size of our copper cell described in Section 3.2.3 and the molecules are randomly distributed over all possible m_J levels. Each molecule gets a random velocity with components v_x, v_y and v_z that are consistent with a Maxwell-Boltzmann distribution at a specified temperature. However, although the molecules are distributed over all possible m_J levels, they all populate the rotational and vibrational ground state, *i.e.* vibrational and rotational cooling is not treated by the simulation. This is a simplification, since typical initial temperatures within the experiment are on the order of 1000 K and therefore hardly any molecules do populate the rotational and vibrational ground states originally.

The trajectory of each molecule is solved by integrating Newton's equations of motion until a specified end time or until the molecule escapes from the cell volume. This can be done for the field-free case or within the potential of a magnetic trapping field. For analysis, output files can be generated including information like trajectories, escape time, potential and kinetic energy, time decay curves, etc..

Any interaction between the molecules is neglected since all processes will be completely dominated by collisions with the buffer-gas atoms. This is a reasonable assumption, since Helium densities of $\sim 10^{15}$-10^{16}

cm^{-3} are typically needed to sufficiently cool the particles of interest before they can reach the cell walls and are lost. Based on our spectroscopic data on CrH described in Section 6.5, we can estimate the molecular densities within the magnetic trapping field to be only on the order of 10^6 cm^{-3}.

5.3 Numerical trajectory calculation

As mentioned above, the trajectory of each molecule is calculated by solving Newton's equations of motion. Figure 5.1 shows a typical trajectory, for a particle with an initial temperature lower than the trap depth when no buffer-gas is present. Since the magnetic trapping field is conservative, the particle neither gains or loses energy and, as a consequence, it will orbit the trapping center forever.

The situation changes when collisions with a background gas are taken into account. Every collision will have an effect on the velocity of the molecule and thus the energy of the travelling particle will be changed. The next section describes the details concerning the handling of collisions within this simulation.

5.4 Collisions

5.4.1 Time between collisions

The mean time between collisions of a molecule and a helium atom is given by [147]

$$\tau = \frac{1}{n\sigma_{el} \cdot \langle v_{rel} \rangle} \simeq \frac{1}{n\sigma_{el} \cdot \langle v_{He} \rangle}, \qquad (5.1)$$

with the mean relative velocity between the collision partners $\langle v_{rel} \rangle$, the mean relative velocity of the atoms $\langle v_{He} \rangle$, the elastic collision cross section σ_{el} and the helium buffer-gas density n.

In reality, the time between collisions is not constant, but follows a distribution with a mean value given by Equation (5.1). From statistical physics it is known, that the probability $p(t)$ of a molecule to survive a
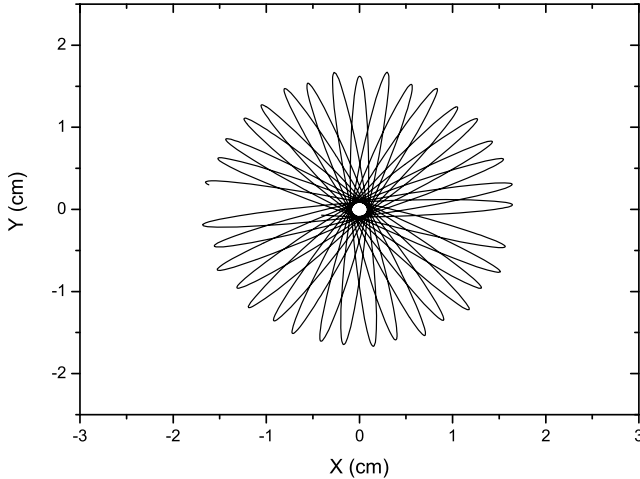
Figure 5.1: Simulation of the x- and y- components of the trajectory of a molecule in our magnetic trapping field with no buffer-gas present. The particle's energy is lower than the trap depth. The center of the trap is at the origin of the coordinate system and the particle orbits around the trapping center forever.

time t without experiencing a collision is given by the exponential decay function [147]:

$$p(t) = e^{-t/\tau}. \tag{5.2}$$

To implement this in the simulation, we need a function for the collision time t_{col} that, in combination with a random number generator, gives this probability distribution if a large number of collision times are generated. This function is built from a random number generator $Ran[0, 1]$, that gives a uniform distribution of values from the interval between 0 and 1 [148]. The corresponding collision times to the gener-

ated values from this interval are then calculated according to

$$t_{col} = -\tau \cdot ln(1 - Ran[0,1]). \tag{5.3}$$
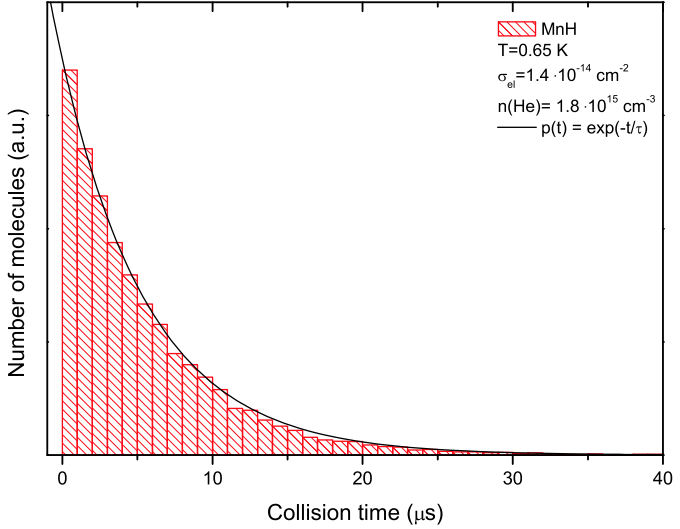
Figure 5.2: Histogram of collision times calculated with the help of Equation (5.3) for 10^4 MnH molecules in a helium buffer-gas of a density of $1.8 \cdot 10^{15}$ cm^{-3} and a temperature of 650 mK. The required functional form of Equation 5.2 ($p(t) = e^{-t/\tau}$) is reproduced by means of the generation of random numbers in the interval [0,1] using Equation 5.3.

Figure 5.2 shows a histogram plot of the collision times of 10^4 MnH atoms calculated with the help of expression (5.3) for a buffer-gas density of $1.8 \cdot 10^{15}$ cm^{-3} and a temperature of 650 mK. As it can be seen, this plot reproduces Equation (5.2), also shown in this figure.

5.4.2 Elastic collisions

As already mentioned, during the time between collisions t_{col} with the helium atoms, the trajectories of the molecules are solved using Newton's

equations of motion. This section now describes how the simulation handles the elastic collision events, responsible for cooling. In the next section, the inelastic collision handling procedure leading to trap loss via spin-flip collisions is described.

Once the trajectory has been evaluated to the time of a collision event, the elastic collisions are treated statistical as billiard-like (hard spheres). To simplify this problem, these collisions are treated in the center-of-mass frame (CM). The technical details and the subsequent steps within the collision handling subroutine are described below:

1. First the program checks whether the collision is elastic, or inelastic. This is done by checking the following statement

$$Ran[0,1] > \frac{\sigma_{inel}}{\sigma_{el}}, \qquad (5.4)$$

where σ_{inel} and σ_{el} are the specified inelastic and elastic collisions cross sections and $Ran[0,1]$ is the output of the random number generator.

If this statement is true, the collision is completely elastic and the simulation proceeds as follows.

2. A helium atom is generated with random velocity components v_x, v_y and v_z, consistent with a Maxwell-Boltzmann distribution at a specified buffer-gas temperature.

3. The collision process can be simplified if it is treated in the center-of-mass frame (CM) (for a detailed treatment of this see [149]). To do this, the following steps are executed:

   (a) As a first step, the CM velocity v_{cm} is calculated via

   $$\vec{v}_{cm} = \frac{m_{mol} \cdot \vec{v}_{mol} + m_{He} \cdot \vec{v}_{He}}{m_{mol} + m_{He}}, \qquad (5.5)$$

   where m_{mol} and m_{He} are the molecule and helium masses with corresponding velocities $\vec{v}_{mol}$ and $\vec{v}_{He}$.

   (b) After this, a transformation into the CM frame is performed.

   $$\vec{v}_{mol(cm)} = \vec{v}_{mol} - \vec{v}_{cm}, \qquad (5.6)$$

where $\vec{v}_{mol(cm)}$ is the velocity of the molecule in the center-of-mass frame.

(c) It can be shown [149] that the absolute value of the velocity after the collision can be written as

$$\|\vec{v}\,'_{mol(cm)}\| = \frac{m_{He} \cdot \|\vec{v}_{mol(cm)}\|}{m_{mol} + m_{He}}. \qquad (5.7)$$

(d) Now a vector $\vec{v}\,'_{mol(cm)}$ needs to be created. Since we are dealing with statistical collision processes, this is done by randomly picking a vector from a sphere with radius $\|\vec{v}\,'_{mol(cm)}\|$.

(e) As a last step we transform back to the initial frame via

$$\vec{v}\,'_{mol} = \vec{v}\,'_{mol(cm)} + \vec{v}_{cm}, \qquad (5.8)$$

where $\vec{v}\,'_{mol}$ is the new velocity vector after the elastic collision with the helium atom.

4. The elastic collision is now over and a new collision time t_{col} is generated.

As a test for this subroutine, Figure 5.3 shows the velocities of an ensemble of thermalized MnH molecules. The MnH molecules, at an initial temperature of 1000 K have been placed in the center of a volume filled with helium with a density of $1.0 \cdot 10^{16}\,\mathrm{cm}^{-3}$ and at a temperature of $0.5\,\mathrm{K}$. After thermalization via elastic collisions, excellent agreement between the numerically calculated velocities and a plot of the Boltzmann temperature for MnH molecules at a temperature of $0.5\,\mathrm{K}$ (solid line) is obtained.

Figure 5.4 illustrates the influence of elastic collisions on the trajectories of the molecules. It shows the x- and y- components of a trajectory of a molecule diffusing through a helium gas in the presence of a magnetic trapping field. The molecule, initially 1000 K hot, is created about $3\,\mathrm{cm}$ from the trapping center and after many collisions it is thermalized and attracted towards the center of the trapping field, which is at the origin of the coordinate system.
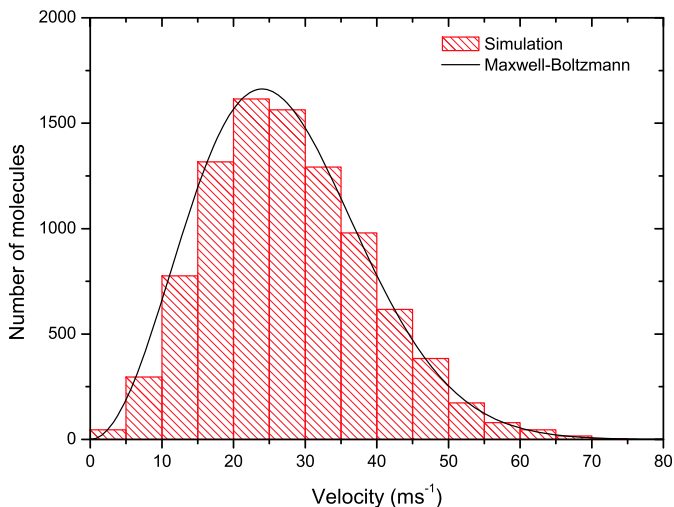
Figure 5.3: Histogram of the velocities of initially hot MnH molecules (blocks) after thermalization for 25 ms with a helium background gas of $n = 1.0 \cdot 10^{16} \, \text{cm}^{-3}$ and a temperature of $0.5 \, \text{K}$. The solid line is a plot of the Maxwell-Boltzmann velocity distribution for MnH molecules at the given buffer-gas temperature.

5.4.3   Inelastic collisions

Introduction

This section describes how the simulation handles inelastic spin-flip collisions between the molecules and the helium atoms. This process can result in strong limitations on the storage times and thus is of great importance for the trapping dynamics in a buffer-gas environment. Fitting numerically simulated storage times to measured lifetimes at different buffer-gas densities should allow to extract values for the inelastic molecule-helium cross sections σ_{inel}.

Unfortunately, there is not much known about inelastic scattering processes of high multiplicity molecules like MnH and CrH. As a consequence, we have to extrapolate results from *ab initio* studies of molecules
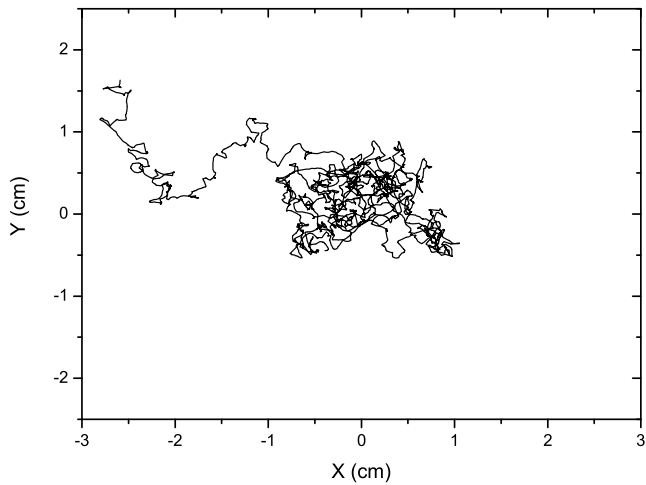
Figure 5.4: A full trajectory, showing the x- and y-components of a molecule traveling through a volume filled with buffer-gas at a density of $1.0 \cdot 10^{15}\,\mathrm{cm}^{-3}$ and at a temperature of $0.5\,\mathrm{K}$ in the presence of a magnetic trapping field. The initial temperature of the molecule was set to be 1000 K. The molecule is created at a distance of about $3\,\mathrm{cm}$ from the trap center. After many collisions, the molecule is thermalized to the helium temperature and diffuses towards the center of the trap, which is at the origin of the coordinate system.

in $^3\Sigma$-states, *e.g.* from NH-^{3}He collisions [85,98] to implement these processes in the simulation. From these studies it is known that spin-flipping transitions are dominantly caused by coupling of the Zeeman levels via the electrostatic interaction of the $N = 0$ and $N = 2$ rotational levels (see also Section 2.4.2). Figure 5.5 (*top*) depicts a result from these investigations. The inelastic collision cross section exhibits a strong dependence, both on the magnetic field as well as the collision energy. However, the dependence on the magnetic field becomes negligible at collision energies of $\sim 0.1\,\mathrm{cm}^{-1}$ and a sharp cross section rise, induced by a shape resonance, starts to appear. A similar behavior was found in studies on CaH [150]. Since no such calculations do exist for MnH and CrH so far, we have to use a rather qualitative model for the inelastic collision cross sections.

In the lower plot of Figure 5.5, the collision energies E_{col} for MnH molecules at our typical experimental temperature of $T = 650\,\mathrm{mK}$ is shown. As it can be seen, the collision energies are dominated by energies greater than $0.1\,\mathrm{cm}^{-1}$. If we would have NH under our experimental conditions, the magnetic field dependence could be neglected and Zeeman relaxation would be completely dominated by collisions at energies $\gtrsim 0.1\,\mathrm{cm}^{-1}$. It is not unlikely that a similarly sharp rise in the inelastic collision cross section as a function of collision energy is also present for MnH and CrH. To account for this in a simple model, we implement the inelastic collision cross section as a step-function: if the collision energy is below a certain energy barrier E_b the inelastic collision cross section is zero, otherwise it is a non-zero constant. A scheme of this is depicted in Figure 5.6 (right). We further simplified the collision treatment within the simulation by neglecting any magnetic field dependence of the elastic and inelastic collision cross sections. However, we cannot rule out that such dependencies on the magnetic field, as well as a more realistic dependence of σ_{inel} on the collision energy have to be implemented for an adequate physical description.

Another free parameter lies in the choice whether to include transitions with $|\Delta m_J| > 1$. We perform simulations both with inelastic collisions restricted to neighboring Zeeman levels ($\Delta m_J = \pm 1$) and with inelastic collisions to all Zeeman levels ($\Delta m_J = $ all) (see Figure 5.6 (top)). In any case, the final Zeeman states have to be energetically
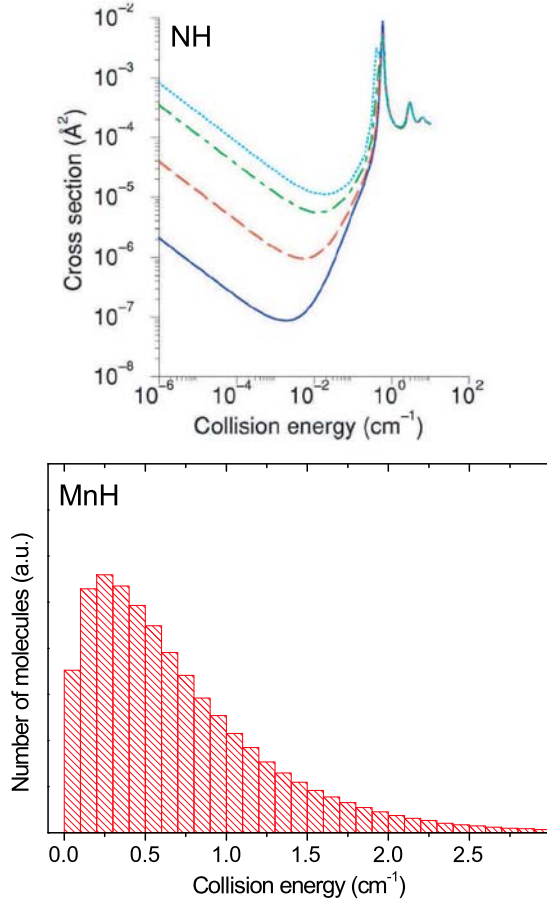
Figure 5.5: *top*: Inelastic NH-^{3}He collision cross section determined by ab initio studies and plotted for different magnetic fields of $100\,\mathrm{G}$ (full curve), $300\,\mathrm{G}$ (long-dashed curve), $700\,\mathrm{G}$ (dot-dashed curve) and $1000\,\mathrm{G}$ (dotted curve). A strong dependence on the magnetic field as well as on the collision energy is observed.
bottom: Plot of collision energies for the MnH-^{3}He system at our experimental temperature of 650 mK. Most of the collisions lie in the range between 0.1 and $2.0\,\mathrm{cm}^{-1}$. The collision energies for CrH molecules are very similar.

reachable with the available collision energy, which is calculated for each collision event.

Inelastic collision subroutine

This section describes the technical details and subsequent steps within the inelastic collision subroutine. It gets executed if statement (5.4) is wrong. In addition, the collision energy E_{col} needs to exceed a specified energy barrier E_b for the reasons given above. Typical values for E_b used within the simulation are $0.0\,\mathrm{cm}^{-1}$, $0.25\,\mathrm{cm}^{-1}$, $0.5\,\mathrm{cm}^{-1}$, $1.0\,\mathrm{cm}^{-1}$ and $1.5\,\mathrm{cm}^{-1}$. From that point on, the procedure first proceeds identically to the elastic collision subroutine, described in Section 5.4.2. Only from the point where the new velocity in the CM-frame $\vec{v}\,'_{mol(cm)}$ in Equation (5.7) is determined, things are treated differently. The subsequent steps of this subroutine are summarized here:

1. The inelastic collision handling procedure starts if the collision energy is larger than the specified energy barrier E_b *and* if statement 5.4 is wrong.

2. A helium atom is generated with random velocity components v_x, v_y and v_z, consistent with a Maxwell-Boltzmann distribution at a specified buffer-gas temperature.

3. The collision is treated in the CM frame to determine $||\vec{v}\,'_{mol(cm)}||$, identical to the elastic collision routine.

4. Inelastic collisions change the electronic spin states of the molecules. To account for this, the Zeeman state into which the particle gets transferred via the inelastic collision process, is determined. Two different models are implemented:

   (a) Only one electron spin can flip and therefore only $\Delta m_J = \pm 1$ is possible.

   (b) All the electron spins of the molecule can flip and therefore all m_J states are reachable ($\Delta m_J = $ all).

   Independent of the spin-flipping model used, only states will be populated that are energetically reachable. In other words, the
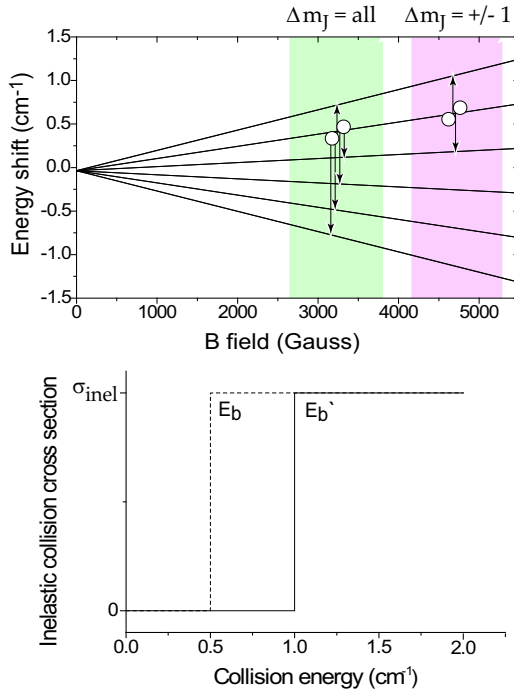
Figure 5.6: *top*: Scheme of the two spin-flipping models that are implemented in the simulation. Either inelastic collisions are restricted to neighboring Zeeman levels ($\Delta m_J = \pm 1$) or all Zeeman levels (Δm_J = all) can be reached in one collision event.
bottom: Implementation of an inelastic collision energy barrier. If the collision energy is below a certain energy barrier E_b the inelastic collision cross section is zero, otherwise it is a non-zero constant σ_{inel}.

collision energy has to be larger or equal to the Zeeman energy difference between the initial and the final state. Transitions to lower states are thus always possible, such to higher states are not.

5. Subsequently, the energy difference between those two states $\Delta E_{mf'\leftarrow mf}$ is converted into a change in velocity and added (in the case of $\Delta m_J \leq 1$) or subtracted ($\Delta m_J \geq 1$) to $||\vec{v}\,'_{mol(cm)}||$ from Equation (5.7). Taking into account that the energy difference is distributed equally over the molecule and the helium atom, this leads to:

$$||\vec{v}\,'_{mol(cm)_{inel}}|| = ||\vec{v}\,'_{mol(cm)}|| \pm \sqrt{\frac{|\Delta E_{mf'\leftarrow mf}|}{m_{mol}}} \qquad (5.9)$$

6. From this point, everything is again identical to the treatment of an elastic collision, and the subsequent steps are the generation of the velocity vector $\vec{v}\,'_{mol(cm)_{inel}}$ with the help of expression (5.9) by picking a random direction and the transformation to the initial frame to obtain the final velocity vector $\vec{v}\,'_{mol_{inel}}$.

7. The inelastic collision is now over and a new collision time t_{col} is generated. In the trajectory calculation to the next collision event, the program now takes into account that the molecule experiences a different potential, since its new state typically experiences a different Zeeman-energy shift.

5.5 Computational simplifications and technical choices

In order to reduce the computational time of the simulation, we make approximations regarding the calculation of the magnetic field and the integration time steps. However, the most important simplification is how the collisions with the helium background gas have been implemented. The trajectories of the He gas atoms are not calculated, instead, as explained in Section 5.4, collisions with the injected molecules are treated statistically.

The trapping field is calculated, by solving Biot-Savart's law for our specific magnet coil configuration described in Section 3.2.5. To speed up the running time, this is only done once. The resulting field is then stored in an array which gets interpolated in the actual trajectory simulation.
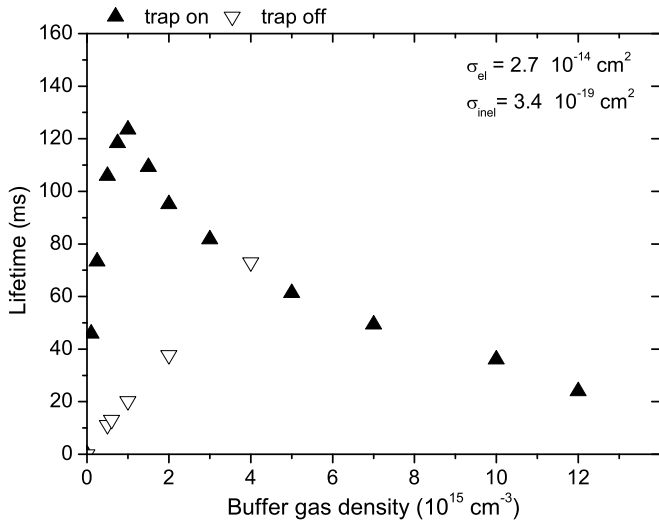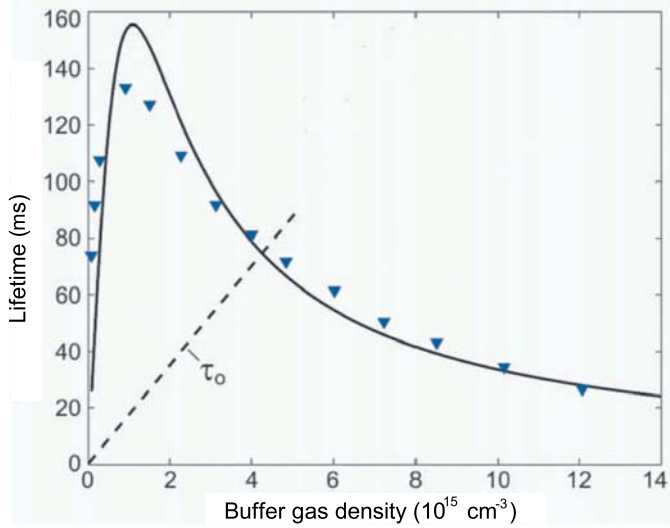
Another important factor for minimizing the computational effort regards the implementation of integration time steps for the trajectory calculation. We chose these to be dynamic and implemented this using a Runge-Kutta adaptive step size engine [148]. This way, the integration time steps are adjusted, such that the result of the integration stays within a specified precision. This has the big advantage that the simulation gives a good description (with variable precision) of the system under various experimental conditions, while minimizing the running time of the simulation.

5.6 Application of the simulation to the buffer-gas loading data of NH

In a recent experiment at Harvard University, NH molecules have been successfully buffer-gas cooled and loaded into a magnetic trap where storage times of $\sim 200\,\text{ms}$ have been reached [80]. In this experiment, a molecular beam machine is used to produce and load the molecules into the probing area in the center of a buffer-gas cell, coinciding with the center of a magnetic quadrupole trapping field. This is somewhat different from our setup where molecules are created via laser ablation of a solid precursor within the buffer-gas cell. However, from the point on when the molecules have left the molecular beam machine and entered the cell, this should not play a big role for the observable trapping dynamics, since these mostly are determined by the NH-He collision properties as well as by the Zeeman effect of NH. As a consequence, the trajectory simulations that we specifically set up to model the dynamics of our system, should also give a good description of the observations made in the NH experiment. As a final test of our program we therefore tried to reproduce the NH data measured in the Harvard experiment.

Figure 5.7 (top) is a plot of the measured lifetimes of NH molecules at various ^{3}He buffer-gas densities ($T(^3\text{He}) = 710\,\text{mK}$) in the pres-

Figure 5.7: *top*: Plot of the observed lifetime of NH molecules versus the buffer-gas density (solid triangles) in a cooling and trapping experiment similar to ours [80]. The solid line is a fit of an analytical expression to the data. The dashed line indicates the field-free diffusion times τ_0 of NH.
bottom: Storage times of NH molecules versus the ^{3}He buffer-gas density calculated with our numerical simulation (solid triangles), mimicking the experimental conditions under which the NH data has been recorded. Also included are the field-free diffusion times (open triangles).

ence of a magnetic trapping field with a trap depth of $\sim 3.3\,\mathrm{T}$. The observed storage times drop after a maximum at a helium density at $\sim 1.0 \cdot 10^{15}\mathrm{cm}^{-3}$. By fitting analytic expressions to those lifetimes, as mentioned in Section 5.1, the elastic and inelastic collision cross sections for the NH-He system were found to be $\sigma_{el} = 2.7 \pm 0.8 \cdot 10^{-14}\,\mathrm{cm}^2$ and $\sigma_{inel} = 3.8 \pm 1.1 \cdot 10^{-19}\,\mathrm{cm}^2$, respectively. A detailed description of the underlying analytic model, based on the description of the diffusion of two gases through each other, can be found in references [89] and [80].

To reproduce this data with our simulation, we mimicked the magnetic trapping field used in the NH experiment by simply increasing the field calculated for our magnet. This should give a good approximation since the magnet coil configuration, defining the shape of the quadrupole field, is similar to ours. The Zeeman effect of ground state NH molecules ($X^3\Sigma^-$) and the corresponding energy shift within a magnetic field is well known [151] and the implementation in our simulation was straightforward. To extract the lifetimes from our simulation, we randomly placed 10^4 NH molecules with a temperature of $710\,\mathrm{mK}$ within a sphere of $2\,\mathrm{mm}$ around the trapping center. This sphere lies in the center of a helium gas filled volume given by the size of our buffer-gas cell. We then monitor the time evolution of the number of molecules within this sphere.

Figure 5.7 (bottom) shows a plot of the lifetimes at different buffer-gas densities extracted from our simulation. Good agreement to the measured data shown in Figure 5.7 (top) is found for values of $\sigma_{el} = 2.7 \cdot 10^{-14}\,\mathrm{cm}^2$ for the elastic collision cross section and $\sigma_{inel} = 3.4 \cdot 10^{-19}\,\mathrm{cm}^2$ for the inelastic collision cross section, respectively. While σ_{el} is identical to the one found in the Harvard experiment, the inelastic scattering cross section σ_{inel} lies within the specified error bars. We therefore conclude

that the numerical simulation is working as intended and that we can use it to investigate the trapping dynamics of MnH and CrH.

Chapter 6

Buffer-gas cooling and magnetic trapping of CrH and MnH

6.1 Introduction

In this chapter we report on the buffer-gas cooling and magnetic trapping of CrH and MnH molecules. We start with a description of our experimental system and detection setup. Subsequently, essential field-free measurements at room temperature, 4 K, and in the mK regime are presented. Besides the extraction of the buffer-gas densities within our probing area, these measurements allow for measuring the elastic cross section for both molecules as well as giving evidence for rotational cooling within a time of 10 ms.

We then report on the trapping of CrH and MnH molecules at a temperature of 650 mK. Using the numerical trajectory simulations described in the previous chapter, the effects of Zeeman relaxation are studied and inelastic molecule-^{3}He collision cross sections are extracted.

6.2 Method and experimental setup

The present experiments are performed in a slightly modified version of the experimental setup described in Chapter 3. For LIF detection, the buffer-gas cell now is additionally equipped with side window access. This is provided by two 12.5 mm diameter sapphire windows with an effective aperture diameter of 9 mm in the side of the cell body. A scheme of this cell is depicted in Figure 6.1. As the effective trap edge in the radial direction coincides with the cell wall, the design of the optical access on the side is aimed at minimizing the cell wall thickness.

For this reason, the side windows are glued using epoxy (Stycast 2850) onto a 0.1 mm thick copper foil, which itself is glued over 25 mm diameter openings in the cell wall. The thin copper foil serves to relieve the mechanical stress on the glue joints and the sapphire window resulting from thermal contraction when the apparatus is cooled down from room temperature. For preparation, we carefully scratched the outermost mm of the sapphire window with a diamond rasp in order to obtain a large gluing surface area at the overlap to the foil. In addition, all copper surfaces were roughened with sandpaper and subsequently cleaned with acetone. Prior to gluing, both sides of the joint had been covered with epoxy and then left to dry over night at room temperature. This combination remained leak-tight after multiple cooling cycles from room temperature to below $1\,\mathrm{K}$ and even survived several quenches of our superconducting magnet, a process where the cell temperature more or less instantaneously rises to a temperature on the order of $100\,\mathrm{K}$. RuO thermistors and a resistive heater, immersed within the cell body, are used to monitor and control the temperature of the cell.

Molecules are injected into the cell via laser ablation from a solid precursor. For this, single light pulses produced by a Q-switched pulsed Nd:YAG laser (Continuum Minilite-II, 532 nm, $\sim$ 12 mJ) are steered and loosely focused with a 750 mm focal length lens onto the precursor targets, glued to the top of the buffer-gas cell. These targets are solid Cr (Mn) chips that are electrochemically doped with H atoms. To prepare these targets the chips are submerged in distilled water and a negative potential with respect to a Pt counter electrode is applied to them. To increase the conductivity of the solution, H_2SO_4 is added until a current of $\sim$ 100 mA between the two electrodes is reached; this current is
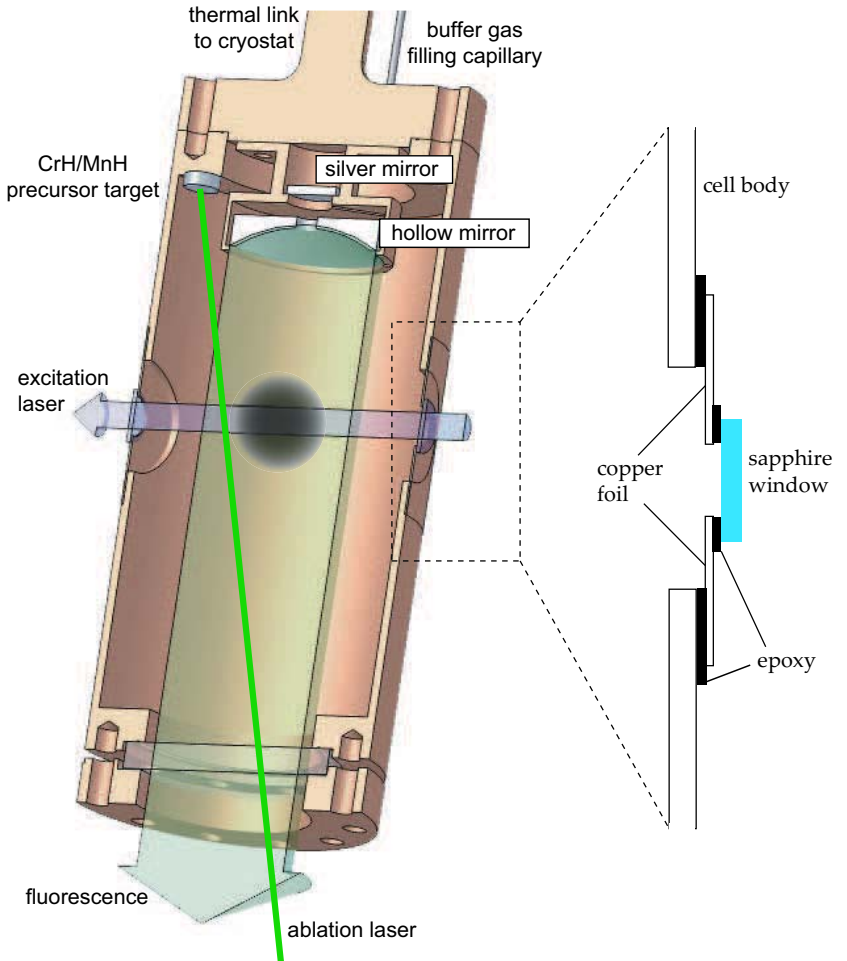
Figure 6.1: (Figure see previous page) *left*: Artist's impression of the experimental copper cell and detection scheme. A concave mirror produces a parallel fluorescence beam to the outside of the cryostat. A central hole in this mirror leads to a small silver mirror allowing absorption measurements.
right: Scheme of the gluing layers that are necessary to mount the side window. Sapphire windows are glued onto thin copper foils. These foils are then glued onto large holes in the side of the copper cell body.

then maintained for 1 hour. This procedure results in the embedding of hydrogen in the intersticial sites of the Cr (Mn) crystal [152]. Since Mn suffers from dissolution by the acid, care is taken to minimize this effect while reaching the necessary current by carefully adjusting the H_2SO_4 concentration. To position the targets inside the buffer-gas cell by gluing, it is unavoidable to expose them to air for a few hours. However, we found that this does not affect the yield for both molecules that are chemically formed in the ablation process.

After injection, the molecules are cooled by the helium gas atoms. In the current experiment we use ^{3}He as buffer-gas because it has a higher vapor pressure than ^{4}He. This allows for buffer-gas loading at lower temperatures with a higher effective trap depth. The disadvantage of the use of ^{3}He with the present cooling power of the dilution refrigerator is that a thermal disconnect from the cell wall is difficult to obtain; however, it will be shown below that this is irrelevant as the trapping times observed are too short to establish a thermal disconnect by means of cryopumping.

Optical detection of the molecules in the trapping region is performed using laser induced fluorescence according to the scheme depicted in Figure 6.2. To this end a pulsed excitation laser is sent through the two side windows and fluorescence produced by the molecules is collected onto a 35 mm diameter concave silver mirror attached to the top of the experimental cell (see also Figure 6.1). In order to minimize the heat transfer to our buffer-gas cell, we reduce the size of the excitation laser beam with the help of an aperture of $\sim 4\,\text{mm}$. With the help of a shutter within the beam path of the excitation laser, single pulses are picked from the laser that nominally runs at a 10 Hz repetition frequency. This is necessary for minimizing the heat transferred into the buffer-gas cell.
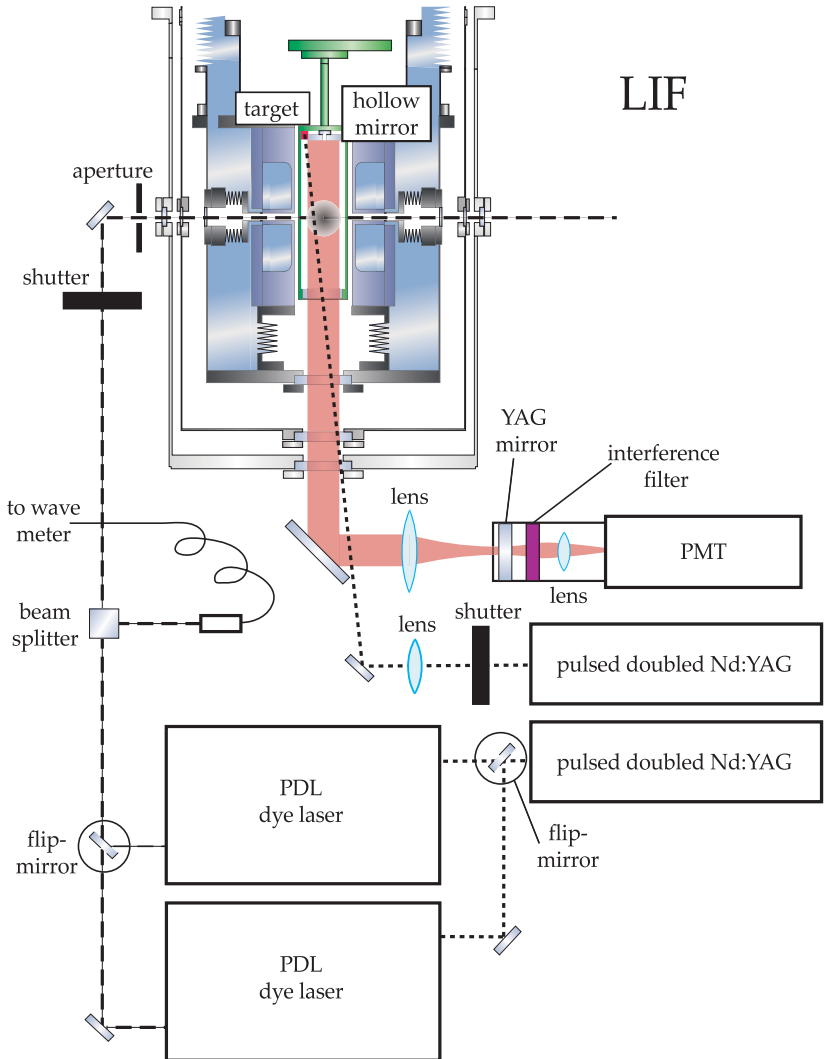
Figure 6.2: (Figure see previous page) Schematic overview of the optical detection setup.
The molecules are produced via laser ablation using a pulsed Nd:YAG laser (dotted line). Subsequently, they are excited via a pulsed dye laser (dashed line). The fluorescence is collected after reflection on a concave mirror on top of the cell. A lens system collects the light and focusses it onto the PMT cathode while passing through an interference filter.

The radius of curvature of the silver mirror for fluorescence collection is chosen such that the 35 mm distance focal point of the mirror coincides with the center of the trapping field. By means of a planar silver mirror, a lens and an interference filter appropriate for the wavelength of the detected light, the reflected fluorescence is imaged onto a photomultiplier tube (PMT, Hamamatsu R943-02) placed outside the experimental vacuum chamber. The combination of all fluorescence collection lenses, windows and filters allows us to detect $\sim 0.1\,\%$ of all photons created in the center of our probing area. To shield the PMT against the stray fields produced by the superconducting magnet, the cathode array is surrounded by a μ-metal shield. The PMT output current is converted into a voltage using a 50 Ω resistor and integrated using a 12 bit 100 MS/s digitizer (Acqiris DC438). For the magnetic trapping experiment of CrH, the PMT current is directly amplified using a fast pre-amplifier (Ortec VT120A) to perform photon counting on the digitizer mentioned above. To obtain information on the time dependence of the number of molecules in the trapping region, the time delay between the ablation and excitation pulses is varied using a homebuilt delay generator.

To allow for a measurement of the buffer-gas density, absorption spectroscopy on a sample of buffer-gas cooled chromium atoms can be performed. To this end a planar silver mirror is placed directly above the concave mirror for fluorescence collection (see also Figure 6.1), and both the concave mirror inside the experimental cell and the planar mirror on the outside for imaging the fluorescence onto the PMT have a 5 mm hole to allow for the entrance and exit of a detection laser. The procedure for atomic chromium detection is identical to that described in Chapter 4.2. The helium density is then determined from the measurement of the field-free lifetimes of chromium atoms within the copper cell.

CrH molecules are detected using LIF via excitation of the $R_1(0)$ rotational transition of the $A^6\Sigma^+$ (v'=1) $\leftarrow$ $X^6\Sigma^+$ (v''=0) band system near 766 nm. Fluorescence into the $X^6\Sigma^+$ (v''=1) state near 860 nm is collected [153]. The 766 nm light is produced by a pulsed dye laser system (Spectra-Physics PDL-3, LDS 751 dye) pumped by a frequency-doubled Nd:YAG laser (Spectra-Physics INDI). With this system 766 nm light pulses of ~ 5 mJ and a bandwidth of ~ 0.1 cm^{-1} are produced. A small fraction of this light is split of and sent to a wavemeter (HighFinesse Ångstrom WS/6) via a beam splitter and a fiber (see Figure 6.2). The dye laser is not actively wavelength stabilized but since both the spectral width of the excitation laser and that of the inhomogeneously broadened transition frequency of the molecular ensemble within the magnetic trap are rather large, small drifts of the wavelength do not substantially affect our measurements.

MnH molecules are detected via excitation of the rotational transition of the $A^7\Pi$ (v'=0, N'=0, J'=2) $\leftarrow$ $X^7\Sigma^+$ (v''=0, N''=0, J''=3) band system near 568 nm and collection of fluorescence into the $X^7\Sigma^+$ (v''=1) state near 624 nm [154]. The excitation light is created by a second pulsed dye laser system, identical to the one for CrH, now with the Rhodamine 6G dye.

6.3 Buffer-gas cooling to 4.2 K

Taking data with our cryogenic system at temperatures below 4 K involves utilization of our ^{3}He-^{4}He-dilution unit. Once this system is running one has to carefully pay attention to keep the temperature in the mixing chamber of this system below ~ 700 mK to maintain a sufficient cooling power. For this, one has to apply a low repetition rate of about 1 measurement every 30 - 40 seconds to allow the system to cool the copper cell from the heat of the ablation pulse before the next Nd:YAG pulse enters the cell.

However, starting measurements at a high repetition rate clearly has advantages. First of all, fine tuning the alignment of the collection lenses with the help of the fluorescence signal is then much easier. In addition, we wanted to check how efficient CrH and MnH are rotationally cooled via inelastic rotational collisions with the helium atoms. For this, several

rotational lines in the spectrum have to be resolved. Since both molecules have large rotational constants of $\sim 6\,\mathrm{cm}^{-1}$, long wavelength scans have to be recorded and also for this a high repetition rate is favorable.

Rotational cooling

The process of rotational cooling enhances the number of molecules in the desired rotational ground state that is used for detection in buffer gas cooling experiments. Likewise, inelastic vibrational collisions enhance the number of molecules in the vibrational ground state. We did not check for vibrational cooling, but measurements of the lifetime of a vibrationally excited state of NH ($X^3\Sigma$, v'=1, N'=0) in a magnetic trap (in the presence of a helium gas) indicate a lifetime of ~ 40 ms. This suggests, that inelastic vibrational collisions of cold molecules occur at a sufficiently slow rate, so that vibrationally excited molecules could be trapped with only small losses due to vibrational inelastic collisions [20].

Figure 6.3 shows spectra of the relevant electronic transitions of CrH and MnH molecules taken at room temperature in a separate test chamber and at 4.2 K within our cryostat. Some rotational transitions have been labelled according to the following labelling scheme: $^{\Delta N}\Delta J_{F_i'F_i''}(N'')$, where N'' denotes the total angular momentum excluding electron spin and nuclear spin of the ground state (and $\Delta N = N'' - N'$, where N' denotes the excited state). J is the total angular momentum excluding nuclear spin (and $\Delta J = J'' - J'$, where J'' and J' denote the ground and the excited state). F_i'' and F_i' denote the spin components of the ground, and the excited state, respectively. The F_i subscripts take on values from $N + S$ to $|N - S|$. The time between ablation and excitation was set to be $400\,\mu$s at room temperature and 10 ms at 4.2 K. The repetition rate of the experiment at 4.2 K was chosen such that the contact gas within the inner vacuum chamber had enough time to cool the copper cell to 4.2 K before the next shot. This allowed us to record one data point every ~ 4 s; a similar repetition rate was applied in the room temperature scans. Since the different setups have different fluorescence collection efficiencies it is difficult to compare the intensities, but the structural differences in both spectra are obvious.

At typical helium buffer-gas densities necessary for translationally cooling a sufficient fraction of particles before loosing them at the cell
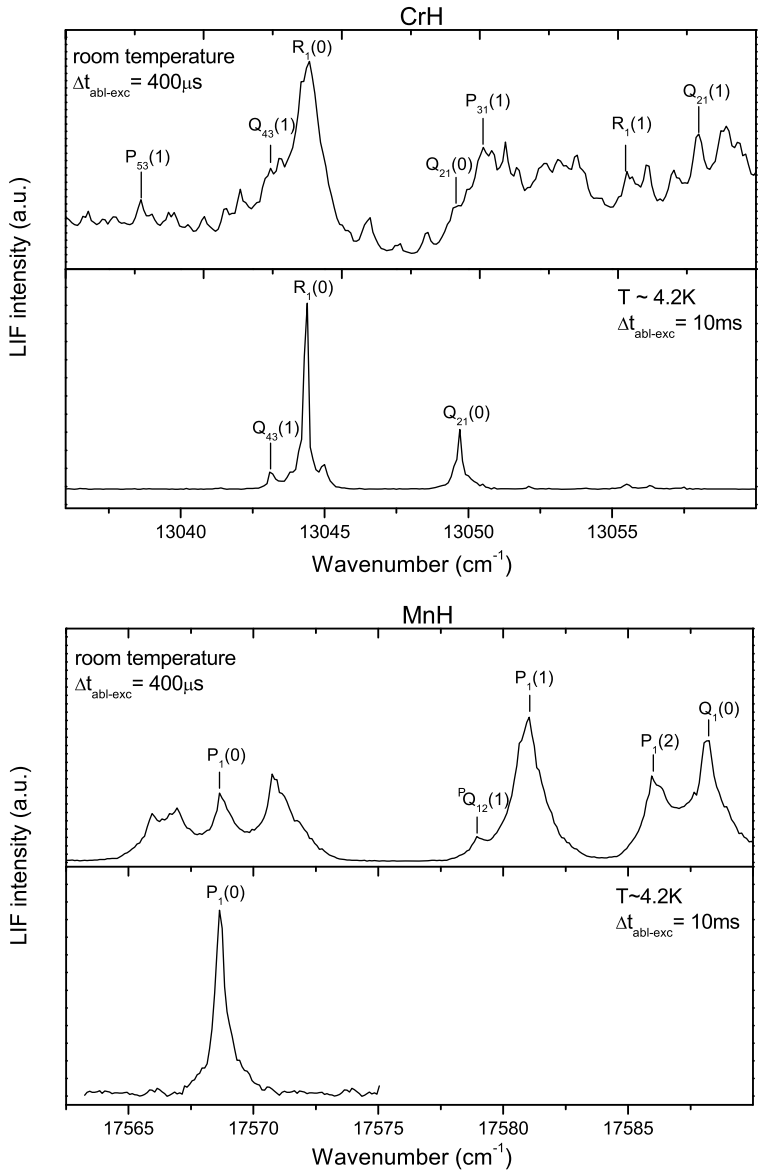
Figure 6.3: (Figure see previous page) *Top graph*: Laser induced fluorescence excitation spectrum of CrH at room temperature (upper part) and at $\sim 4.2\,$K (lower part). *Bottom graph*: Laser induced fluorescence excitation spectrum of MnH at room temperature (upper part) and at $\sim 4.2\,$K (lower part). In all spectra several rotational transitions are labeled. While there are many lines arising from rotationally excited molecules at room temperature, nearly all of them vanish when the molecules are thermalized to $\sim 4.2\,$K.

walls, the particles' translational motion is thermalized within a very short time on the order of 100 μs (see Section 2.6.2). Rotational cooling will happen on a slightly longer, but similar timescale. We did not investigate the dynamics of rotational cooling in detail, but from Figure 6.3 it is clear that at least within 10 ms most of the molecules are transformed into their rotational ground state. While many rotational lines are present for both molecules at room temperature (upper figures), most of them are gone in the spectra taken at liquid helium temperatures after 10 ms (bottom figures). The remaining lines at 4.2 K mostly arise from the rotational ground state ($N'' = 0$).

6.4 Field-free measurements below 1 K

Measurements of the field free diffusion times enable the extraction of the molecular elastic collision cross sections with ^{3}He, provided we know the buffer gas density in the experimental cell. We determine this density by measuring the diffusion time of Cr atoms through the helium gas. The procedures to extract the helium buffer-gas densities and the elastic collision cross sections are described here.

Determination of the helium buffer-gas density

We determine our helium buffer-gas density by measuring the field-free diffusion of chromium atoms through the helium gas before and after each molecular lifetime measurement. To extract the density from these lifetime measurements, we make use use of an analytical model that describes the diffusion of two different gases through each other [89]. A detailed treatment of this problem can be found in reference [155].

In this model, the temporal time decay of the gas in a cylindrical volume of height h and radius r_0, where particles get destroyed at the cell walls, is given by a single exponential with a time constant of

$$\tau \simeq 2.1 n \sigma_{el} \cdot \sqrt{\frac{\mu}{k_B T}} \cdot \frac{1}{(\frac{2.4}{r_0})^2 + (\frac{\pi}{h})^2}, \qquad (6.1)$$

where n is the buffer-gas density, σ_{el} is the elastic collision cross section between the two gases, k_B is the Boltzmann constant, T is the temperature of the gases in thermal equilibrium and μ is the reduced mass of the two colliding particles.

From evaporative cooling experiments on ^{52}Cr [78], the Cr-^{3}He elastic collision cross section σ_{el} is known to be $1.8\,(\pm 0.6) \cdot 10^{-14}$cm^2 at a temperature of $300\,$mK. The temperature of our buffer-gas, determined via field-free Cr wavelength scan traces, is $650\,$mK. Assuming that σ_{el} does not change in the temperature range between 300 and 650 mK, we can convert the field-free chromium lifetime τ_{Cr} to a buffer-gas density with the help of expression 6.1. Unfortunately, a large error arises from the uncertainty in the elastic collision rate of chromium that is on the order of $(\pm 30\,\%)$.
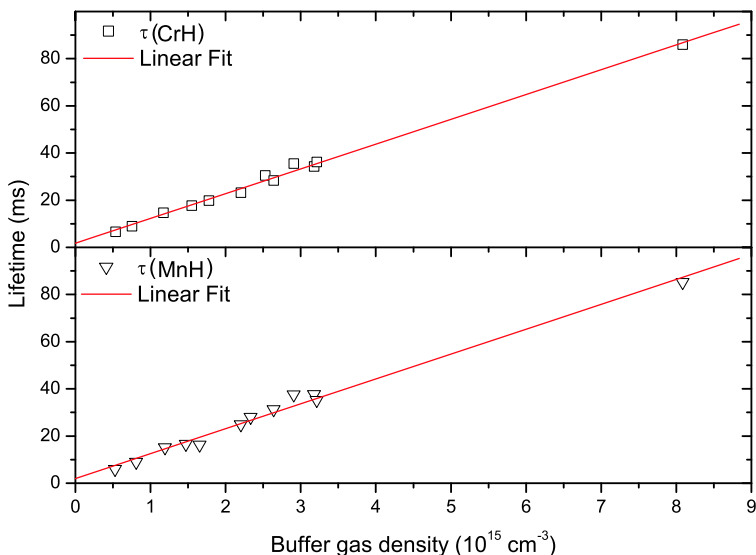
Extraction of the elastic collision cross sections for CrH and MnH

Once we know our buffer-gas densities, we can use Equation 6.1 to extract the elastic collision cross sections for the molecules. Figure 6.4 shows two linear fits of Equation 6.1 to the measured field-free lifetimes of chromium- and manganese hydride where the only free parameter was the elastic collision cross section σ_{el}(CrH) and σ_{el}(MnH), respectively.

Within the precision of our measurement method, both elastic collision cross sections are found to be identical, *i.e.*,

$$\sigma_{el}(\text{CrH}) = \sigma_{el}(\text{MnH}) = 1.4\,(\pm 0.5) \cdot 10^{-14}\,\text{cm}^2. \qquad (6.2)$$

This is close to the value for the elastic collision cross section of NH at $710\,$mK (σ_{el}(NH) $= 2.7\,(\pm 0.8) \cdot 10^{-14}\,$cm^2) [80]. It is unexpected that the elastic collision cross sections for MnH and CrH are smaller with respect to NH, however, all given values for σ_{el} have rather large error bars. As

Figure 6.4: 1/e lifetimes of CrH and MnH as a function of the buffer-gas density. The straight lines show a linear fit of Equation 6.1 to the lifetimes of CrH (upper) and MnH (lower). The only free parameter is the elastic collision cross section $\sigma_{el}(\text{CrH})$ and $\sigma_{el}(\text{MnH})$, respectively.

already mentioned, our error bars are dominated by the uncertainty in the buffer-gas density arising from the error bar in the elastic collision cross section of Cr.

6.5 Magnetic Trapping

To investigate the trapping behavior of chromium hydride and manganese hydride, we measure the diffusion times of both molecules at various buffer-gas densities in a trapping field of $\sim 2\,\text{T}$ resulting in a trap depth of $6.6\,\text{K}$ for CrH and $7.8\,\text{K}$ in the case of MnH. Confirmation of trapping is obtained via comparison with field-free lifetime measurements at the same helium densities.
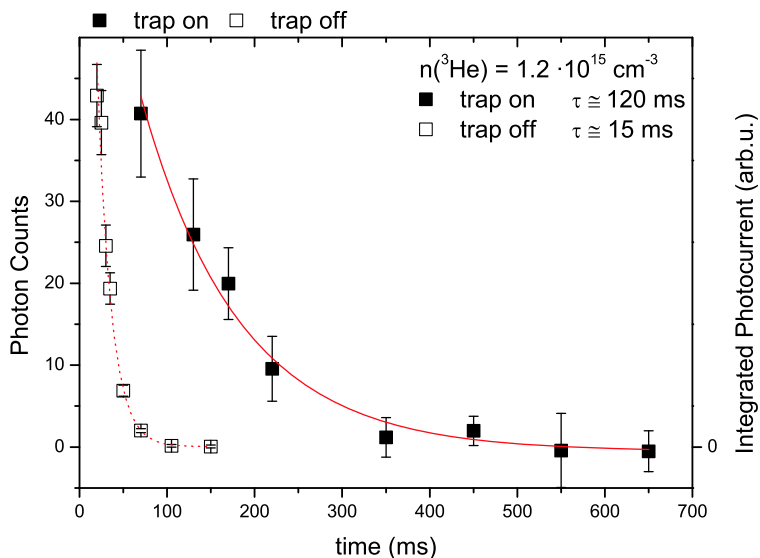
Figure 6.5: Time dependence of the fluorescence signal from CrH molecules after injection into the buffer-gas cell in the presence (solid squares: photon counts) and absence (open squares: integrated photocurrent) of the magnetic trapping field at a buffer-gas density of $1.2 \cdot 10^{15}$ cm^{-3}.

In Figure 6.5 an example of such a measurement is depicted for CrH at a buffer-gas density of $1.2 \cdot 10^{15}$ cm^{-3}. It shows a measurement of the detected fluorescence signal, produced at various delays between the ablation and detection lasers, both with the magnetic trapping field on and off. Due to the lifting of the m_J degeneracy by the presence of the magnetic field and the accompanying broadening of the optical transition used for detection, as well as due to the escape of molecules in untrappable states, the fluorescence signal is strongly reduced when the magnetic field is on. The weakness of the signal combined with the about 1 μs lifetime of the A$^6\Sigma^+$ state of CrH makes the signal suitable for photon counting. To rule out any long term drifts, a random sequence of time delays is used in this measurement. Each data point is the average of five measurements for a specific time delay between ablation and exci-

tation. The measurement values have been fitted to a single exponential decay function, yielding a diffusion time constant. In the case where the diffusion time is significantly enhanced by the presence of the magnetic field, we denote this as a trapping time.

From Figure 6.5 it is immediately clear that the magnetic field enhances the diffusion time of the molecules by a factor of ~ 10, giving a clear signature for trapping. Given our collection efficiency of ~ 0.1 % we have on the order of 10^5 molecules in the center of our trapping field at a density of $\sim 10^6$ cm^{-3} at 100 ms after injection via the ablation pulse.
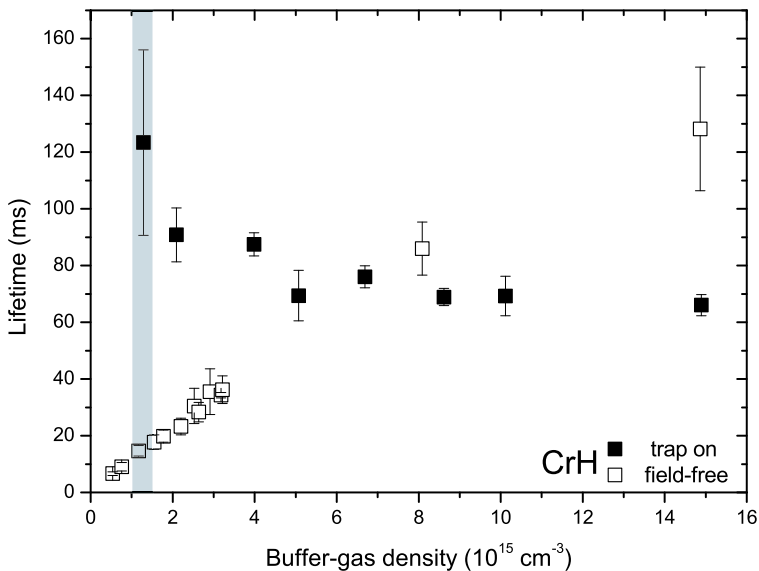
Figure 6.6: CrH lifetime as a function of the buffer-gas density in the presence (solid squares) and absence (open squares) of the magnetic trapping field. The grey bar labels the lifetime measurements depicted in Figure 6.5.

To investigate the collisional properties of CrH, the diffusion time is measured for a number of buffer-gas densities, both with and without the trapping field present. The results of these measurements are depicted

in Figure 6.6. The error bars on the lifetimes are dominated by shot-to-shot fluctuations in the fluorescence signal. This signal instability is on the order of 50 % and arises from the molecule production method via laser ablation. The rate of data taking, which could reduce the statistical errors, is limited by the cooling power of the refrigerator. In the absence of the magnetic field, one clearly recognizes a linear dependence of the diffusion time on the buffer-gas density, which is fully consistent with a simple diffusion process. From this linear dependence of the diffusion time an elastic collision cross section for CrH of $1.4 \, (\pm 0.5) \cdot 10^{-14}$ cm^2 is determined. It is important to note that the error is dominated by the uncertainty in the buffer-gas density, that arises from the uncertainty in the elastic cross sections for the ^{3}He-Cr collisions.

In the presence of the magnetic trapping field the dependence of the lifetime on the buffer-gas density is much more complicated. While the field free diffusion time rises linearly with increasing helium density, the longest storage times are found for low buffer-gas densities in the trapping field. Adding more helium, the trapping time decreases and for densities higher than $7 \cdot 10^{15}$ cm^{-3} the "trapping" time becomes *shorter* than the field free diffusion time. Such a crossing is a strong indication for trap loss due to Zeeman relaxation. Although the addition of more buffer-gas leads to cooling of a larger number of molecules, simultaneously the number of inelastic collisions that changes the spin states of the particles is increased. If these spin-flips transform a significant fraction of molecules into high-field seeking states, their lifetime in the presence of a trapping field is reduced. The field-free diffusion is not affected by such collisions.

The maximum observed trapping time of 120 ms is found at a buffer-gas density of $1.2 \cdot 10^{15}$ cm^{-3}. At lower buffer-gas densities, the fluorescence signal is too weak to record a clear signal. This indicates a very strong increase in the signal at a certain threshold buffer-gas density. It is likely that at densities below $1.2 \cdot 10^{15}$ cm^{-3} the number of helium-CrH collisions is insufficient to translationally and rotationally cool a substantial fraction of the injected CrH molecules.

In Figure 6.7, the same measurements as described above are depicted for MnH. The error bars for the data in the presence of the magnetic trapping field are somewhat larger for MnH than for CrH. This partly
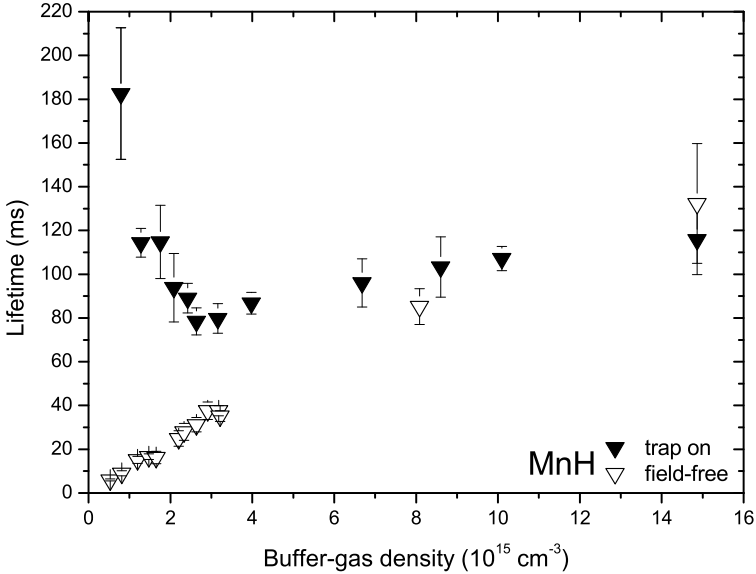
Figure 6.7: Lifetime of MnH molecules as a function of the buffer-gas density in the presence (solid triangles) and absence (open triangles) of the magnetic trapping field.

arises from the use of photon counting for CrH, which not possible for MnH due to the short lifetime of 93.1 ns of the $A^7\Pi^+$ state of MnH.

The dependence of the trapping time on the buffer-gas density is similar to that for CrH. Interestingly, however, the crossing is much less pronounced. Rather, where the trapping time for CrH monotonously falls with increasing buffer-gas density, for MnH the trapping time goes through a minimum at a buffer-gas density of $\sim 2.5 \cdot 10^{15}$ cm^{-3} after which the trapping time increases again.

This counterintuitive effect can be explained as follows: an increased density of the buffer-gas will lead to an increase of the number of collisions that leave a particle in a high-field seeking state and should result in a larger trap loss and a decreased lifetime. However, inelastic collisions can also transfer particles from a high-field seeking into a low-field

seeking state. If the buffer-gas density gets so high that the average time between collisions becomes smaller than the time it takes the particle to escape to the cell wall, and spin-flip collisions from high- to low field seeking states start to enhance the lifetime. This observed enhancement thus indicates a substantially larger inelastic collision cross section for MnH than for CrH.

The functional form of the density dependence of the trapping time of CrH is very similar to that measured for NH by Doyle and coworkers [80]. For NH, a similar maximum trapping time of 200 ms was found, although this was measured at a lower trap depth than used in the current experiment. At our buffer gas temperature of ~ 650 mK we have an effective trap depth $\eta = \mu B / k_B T \sim 10$. In the NH experiment effective trap depths below $\eta = 7$ were used [80]. This points to a less favorable ratio of elastic to inelastic collision cross sections for CrH with ^{3}He than for NH with ^{3}He.

6.6 Investigation of the cooling and trapping dynamics

To quantify the latter statement, we perform trajectory simulations of CrH (and MnH) molecules in a buffer-gas experiment. The details of this simulation are described in detail in Chapter 5. For a given inelastic collision cross section σ_{inel} the time dependence of the density of molecules in the center of the trapping region is extracted from the simulation. This calculated lifetime is then compared to the measured molecule lifetimes. A best value for σ_{inel} is then obtained by minimizing χ^2. This is done for several values of the inelastic collision energy barrier E_b and for each choice of transitions allowed in inelastic collisions.

Figures 6.8 and 6.9 show the result of the simulations for CrH and for MnH, respectively. In each of the figures, the best fit to the trapping time dependence on buffer-gas density is given for a few collision energy barriers E_b. The results are shown both for the model where inelastic collisions are restricted to neighboring Zeeman states ($\Delta m_J = \pm 1$, top graphs) and for the model where all energetically accessible Zeeman states can be reached in a single spin-flip process. For both molecules,

the resulting inelastic collision cross sections are substantially larger for the neighboring-states model than for the all-inclusive model. This is readily explained by the fact that in the all-inclusive model ($\Delta m_J =$ all), a change from a trapping into a non-trapping state can be induced by one single collision. For comparison, in the neighboring state model it requires at least 4 collisions for an $m_J=3$ state to become non-trappable.

A second common feature is the rise in trapping time at large helium densities for a higher collision energy barrier E_b. This can be explained as follows: while inelastic collisions can bring a molecule in an untrappable, high field seeking state, the reverse can also happen. This last process can only take place if the collision energy is sufficient to transfer the molecule to the higher energy state. Raising E_b, and thus requiring a higher collision energy to produce a spin-flip, eliminates all inelastic collisions at energies below E_b. This includes those, that typically induce transitions to lower energy and therefore less trappable states. As a consequence, the relative probability for a collision that transforms the molecule into higher energy (more trappable) Zeeman states is increased. Since the average time between two spin-flip collisions at high buffer-gas densities is shorter than the time that a high field seeking molecule needs to escape the trapping volume, a significant number of molecules can be "switched" between *trappable-* and *non-trappable* states. If this happens for many molecules of the ensemble, the observable lifetime is enhanced. This effect is more pronounced in the neighboring state model due to the fact that, if the collision energy is sufficient to reach the higher Zeeman level, there is always a 50 % chance for a $\Delta m_J = +1$ transition. This is in contrast to the all-inclusive model where typically more transitions to lower states are possible, since these are energetically always allowed.

For CrH it can be seen in Figure 6.8 that for both models a satisfying agreement between simulated and experimental data can be obtained. However, one should note that the energy barrier of 1 cm^{-1} for which the best agreement is obtained in the all-inclusive model rules out $\sim$ 70% of the collisions at 650 mK, and one might therefore question how realistic such a model is.

For MnH, the all-inclusive model is not able to reproduce the observed buffer-gas density dependence of the trapping time, even at a relatively high energy barrier of 1.75 cm^{-1}. The neighboring states model
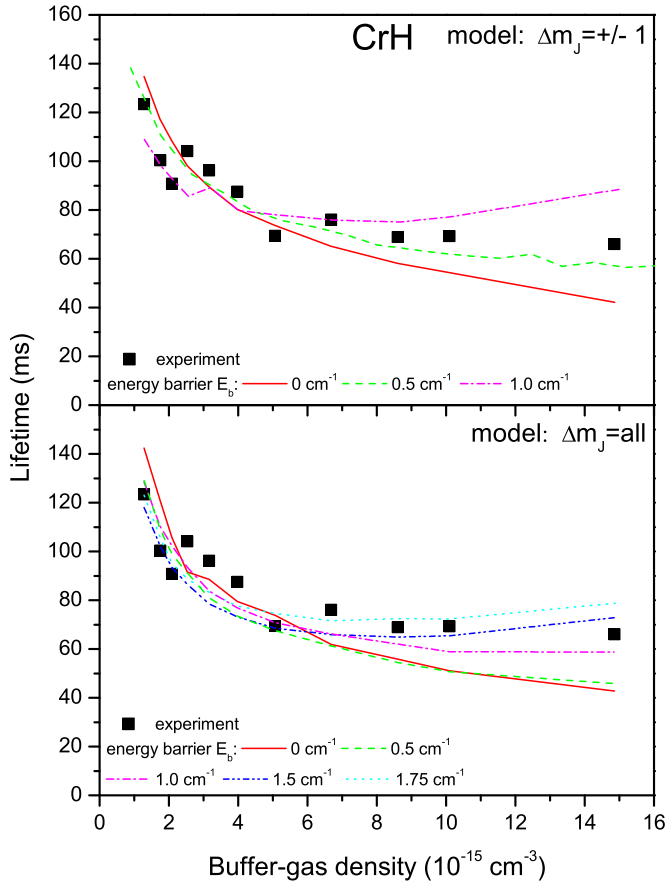
Figure 6.8: Simulated lifetimes of CrH as a function of the buffer-gas density for two implementations of the spin-flipping model. Each graph shows the best fit for a given inelastic collision energy barrier E_b. In the top curve inelastic collisions are restricted to neighboring Zeeman states ($\Delta m_J = \pm 1$); in the bottom graph all energetically accessible Zeeman states are included. The experimentally obtained data are shown in both graphs as solid squares.
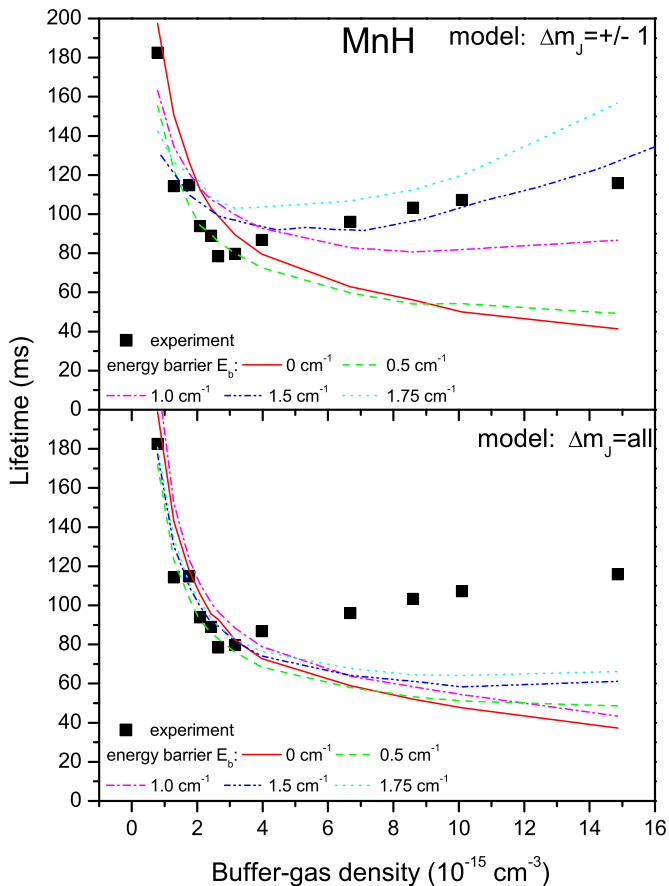
Figure 6.9: Simulated lifetimes of MnH as a function of the buffer-gas density for two implementations of the spin-flipping model. Each graph shows the best fit for a given inelastic collision energy barrier E_b. In the top curve inelastic collisions are restricted to neighboring Zeeman states ($\Delta m_J = \pm 1$); in the bottom graph all energetically accessible Zeeman states are included. The experimentally obtained data are shown in both graphs as solid squares.

does give a good agreement with the observed data, including the rise in the trapping time for higher buffer-gas densities discussed above.

Based on these observations we conclude that a model where only neighboring states are accessible in inelastic collisions is the most suitable to describe Zeeman relaxation. With this, we obtain for CrH an inelastic collision cross section of $1.6 \cdot 10^{-18}$ cm^2, with an inelastic collision energy barrier E_b of 0.5 cm^{-1}. For MnH, we obtain an inelastic scattering cross section of $3.1 \cdot 10^{-17}$ cm^2 at an inelastic collision energy barrier of 1.5 cm^{-1}. These values correspond to a gas temperature of 650 mK. The cross section for MnH is an order of magnitude larger than in the case of CrH, and leads to a lifetime extension at high buffer-gas densities due to an increased (back-)conversion of the molecules from high- to low-field seeking behavior on their way towards the trap edge. It is difficult to give reliable uncertainties for the inelastic collision cross section values given the very simplified inelastic scattering model. For CrH we estimate the relative error to be about 30%. For MnH, where the match between theoretical model and measured data is worse, it should then be about 50%.

Figure 6.10 shows more detailed plots of the CrH and MnH trapping times versus the buffer-gas density that show the best agreement with our experimental data. Here, it can be seen that the trapping time rises very fast at low buffer-gas densities, until reaching a sharp maximum at $\sim 1 \cdot 10^{15}$ cm^{-3}. After this, the trapping time gradually decreases over the buffer-gas range studied in this work and, for MnH, exhibits an increase above $\sim 5 \cdot 10^{15}$ cm^{-3}.

The maximum predicted trapping time of 250 ms for CrH could experimentally not be observed due to low signal strength. As already mentioned, a certain buffer-gas density is needed for cooling a sufficient fraction of molecules before they are lost at the cell walls. From our simulations we know that below a ^{3}He "threshold" buffer-gas density of $\sim 1.0 \cdot 10^{15}$ cm^{-3} hardly any molecules are translationally cooled. In addition to translational cooling, the molecules need to be cooled to the rotational ground state. Since we use this state for monitoring the relative number of molecules in the buffer-gas cell, this is a crucial process that presumably happens on a similar, but slightly longer timescale than cooling of the translational motion. We therefore conclude that at
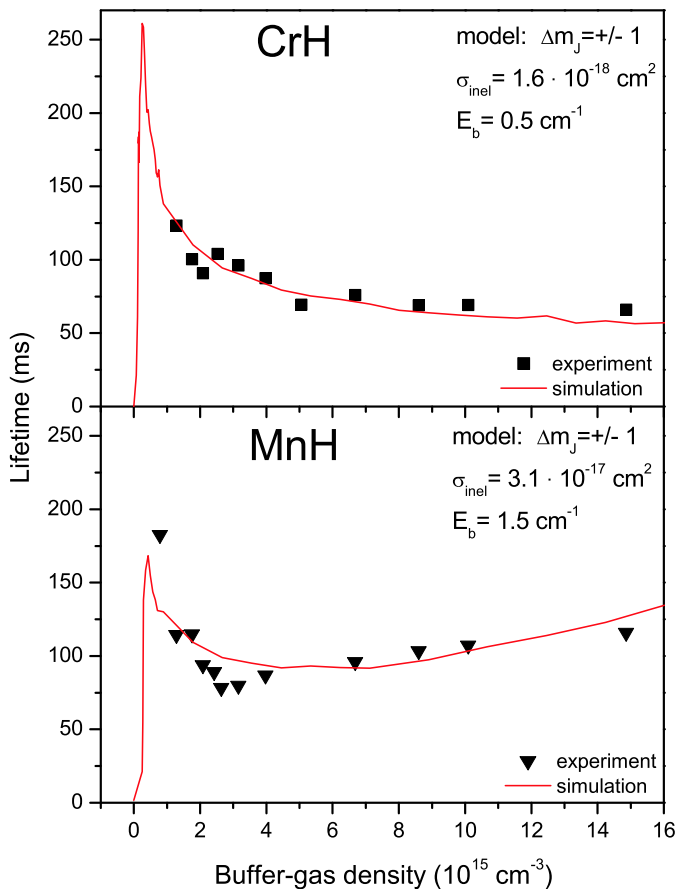
Figure 6.10: Calculated lifetimes of CrH and MnH molecules as a function of the buffer-gas density with inelastic scattering cross sections of $1.6 \cdot 10^{-18} \mathrm{cm}^2$ and $3.1 \cdot 10^{-17}$ cm^2, respectively.

buffer-gas densities of $\sim 0.5 \cdot 10^{15}$ cm^{-3}, for which these lifetimes are predicted, the number of collisions are insufficient to cool a sufficient fraction of molecules, both translationally and rotationally.

While the simulation for CrH shows an excellent agreement with the experimental data, the simulation for MnH exhibits shortcomings, especially seen in the pronounced dip in the observed trapping time around $3 \cdot 10^{15}$ cm^{-3}. This is possibly caused by the oversimplified model of the Zeeman structure in the simulation, where the large density of Zeeman hyperfine states, induced by the nuclear spin ($I = 5/2$) of the ^{55}Mn atom (abundance: 100 %), is not implemented in the simulation. In addition to this, an inelastic collision energy barrier of 1.5 cm^{-1} is quite high, given the fact that all inelastic collisions induced by lower energies, and thus the majority of collisions, are simply not taken into account in our simple inelastic scattering model. Although the simulations give a good insight in the trapping dynamics of both molecules, it is clear that a theoretical study of the CrH-He and MnH-He collision processes, the inclusion of hyperfine effects, rotational cooling, as well as the dependence of the cross sections on the magnetic field are required for a more quantitative model.

6.7 Conclusion and Outlook

MnH and CrH molecules have been buffer-gas cooled and magnetically trapped. Maximum storage times of 120 ms (CrH) and 180 ms (MnH) at buffer-gas densities of $\sim 1 \cdot 10^{15}$ cm^{-3} have been observed. At higher buffer-gas densities Zeeman relaxation leads to lower trapping times which become comparable to the field free diffusion times. To gain a better understanding of the trapping dynamics of MnH and CrH molecules a Monte Carlo simulation has been developed. Using a model where only energetically accessible spin-flipping transitions are allowed, inelastic and elastic collision cross sections are extracted. The model exhibits a good agreement with experimental data and large inelastic scattering cross sections have been found that seem to preclude the prolonged trapping and thermal isolation of samples in a buffer-gas cooling experiment.

The observed trapping dynamics are similar to those made for NH

in the Harvard buffer-gas cooling and trapping experiment [80]. For NH, a ratio of elastic-to-inelastic collisions of $\sim 7 \cdot 10^4$ was found. For CrH and MnH we found significantly lower values of $\sim 9 \cdot 10^3$ (CrH) and $\sim 5 \cdot 10^2$ (MnH). Although the ratio of inelastic to elastic helium-molecule collisions is more favorable for the NH experiment, all results indicate that the trapping of molecules with a triplet or higher multiplicity ground state is severely hindered by the presence of a helium buffer-gas.

The trapping lifetimes could be significantly enhanced when the helium gas is removed directly after the buffer-gas loading. Recently, it has been shown that helium can be rapidly extracted from the trapping area within a time of ~ 40 ms by means of a cryogenically driven active charcoal pump [82]. As long as the removal time is shorter than the trapping time, this will considerably enhance the lifetime of the trapped sample. Implementation of this technically challenging method seems crucial for the preparation of dense samples of trapped, isolated cold molecules using buffer-gas cooling. Moreover, if the buffer-gas removal is successful, the trapping time would benefit from the fact that such a trapped sample is surrounded by a cryogenic environment at sub-Kelvin temperatures. This avoids trap loss via optical pumping with blackbody radiation, an effect that has recently been observed for molecules [116].

Chapter 7

Summary

In this thesis, the potential of the technique of buffer-gas cooling and magnetic trapping a broad range of molecules has been investigated. The experimental and theoretical studies of inelastic collisions in buffer-gas cooling and magnetic trapping have thus far been limited to molecules with a $^2\Sigma$ or $^3\Sigma$ ground state. Here, we set out to obtain information about molecules with ground states of a higher multiplicity.

To test the experimental infrastructure and to become acquainted with the method, we demonstrated buffer-gas cooling and subsequent trapping on a species with well-known properties that has been trapped before. Cr atoms have been confined for times of more than 1 min, and thermal disconnect to the cell walls has been achieved. The use of an absorption-based detection scheme combined with a simulation of the absorption properties of the cloud in the presence of the inhomogeneous magnetic trapping field allowed us to determine a temperature of 350 mK and an initial atom density of $10^{12}\,\mathrm{cm}^{-3}$ for the trapped species. In addition, the loading efficiency has been studied at different trap depths.

Next, we have outlined the criteria for selecting the optimum molecular candidate for buffer-gas cooling experiments. Since a high helium gas density is needed for cooling, such a molecule should have - apart from a high magnetic moment - a low probability for spin-flipping collisions with the buffer-gas atoms as these would result in trap loss. Due to their combination of large rotational constants, Σ ground-states and

small spin-spin interaction coefficients, MnH and CrH molecules have been identified as ideal candidates for buffer-gas loading.

To monitor these molecules by means of LIF detection in the magnetic trapping field, it is crucial to know the Zeeman splittings of the ground and the excited states involved in the transitions. These tunings have been studied and the relevant spectroscopic parameters for both CrH and MnH have been determined.

Following these experiments, the potential to confine and store CrH and MnH molecules has been investigated. Both molecules have been buffer-gas cooled and magnetically trapped. In these experiments on the order of $\sim 10^6$ molecules were loaded into the trap. Maximum storage times of 120 ms (CrH) and 180 ms (MnH) at low buffer-gas densities have been observed. At higher helium densities, the storage times became comparable to the field free diffusion lifetime. This behavior has been investigated using a numerical simulation of the cooling and trapping dynamics of the molecule ensemble. The model is in good agreement with the experimental data and large inelastic scattering cross sections have been found. These lead to a large number of spin-flip collisions that preclude the prolonged trapping and thermal isolation of the samples in the buffer-gas cooling experiment. The elastic molecule-^{3}He collision cross sections have been measured.

The results that have been obtained indicate that the trapping of molecules with a high multiplicity ground state is severely hindered by the presence of the helium buffer-gas. However, it has been shown that helium can be rapidly extracted from the trapping area after cooling by means of a cryogenically driven active charcoal pump [82]. Since the removal times can be shorter than the trapping times that have been observed so far, the effect of spin-flip collisions could be reduced and longer trapping times should be feasible.

Chapter 8

Zusammenfassung

Im Rahmen dieser Doktorarbeit wurde untersucht, ob sich die Technik der Puffergas-Kühlung und magnetischen Speicherung auf eine breitere Auswahl von Molekülarten erweitern lässt. Experimentelle und theoretische Arbeiten hierzu betrachteten bis jetzt leider nur Moleküle in $^2\Sigma$ und $^3\Sigma$ Zuständen. Im Verlauf dieses Projekts wurde nun untersucht, ob sich auch Moleküle in einem Grundzustand höherer Multiplizität mit dieser Technik kühlen und magnetisch einfangen lassen.

Zum Test des experimentellen Aufbaus, und um uns mit dieser Methode vertraut zu machen, kühlten und speicherten wir atomares Chrom. Dies ist eine gut erforschte Spezies, die bereits in früheren Experimenten mit dieser Technik eingefangen werden konnte. In unseren Experimenten konnten Lebensdauern in der Falle jenseits von einer Minute erzielt und die gefangenen Chromatome thermisch von der Zellwand isoliert werden. Mittels Absorptionsdetektion in Kombination mit einer Simulation der Absorptionseigenschaften der atomaren Wolke innerhalb des inhomogenen Magnetfeldes, konnte eine Temperatur von 350 mK und eine anfängliche Teilchendichte von 10^{12} cm^{12} bestimmt werden. Zusätzlich wurde die Effizienz des Prozesses der Ladung der Magnetfalle mittels Puffergaskühlung für unterschiedliche Fallentiefen untersucht.

Um optimale Kandidaten zur Präparation von kalten Molekülen mittels Puffergas-Kühlung zu finden, wurden im Anschluss die dafür notwendigen Moleküleigenschaften ermittelt. Da eine hohe Heliumgasdichte zur

Thermalisierung der anfänglich heißen Teilchen benötigt wird, sollten diese neben einem hohen magnetischen Moment, einen mglichst kleinen inelastischen Stoßquerschnitt besitzen.   Diese Eigenschaft ist äußerst wichtig, da inelastische Stöße mit den Heliumatomen zu hohen Verlusten in der gefangenen Teilchenzahl und damit der Lebensdauer der Molekülwolke in der Falle führen können. Durch die Kombination von hohen Rotationskonstanten, dem Σ Grundzustand und kleinen spin-spin Kopplungskonstanten wurden MnH und CrH als ideale Kandidaten für das Laden einer magnetischen Falle mittels Puffergas-Kühlung identifiziert.

Um diese Moleküle im magnetischen Feld der Falle mittels LIF Detektion nachzuweisen, ist es essentiell die Zeeman-Verschiebung des Grundzustandes, sowie des angeregten Zustandes zu kennen. Diese Verschiebung wurde in Zusammenarbeit mit der Forschergruppe von Tim Steimle untersucht. Auf diesem Weg wurden alle relevanten spektroskopischen Parameter der Zustände für beide Moleküle ermittelt.

Im Anschluss begannen die Untersuchungen zur Speicherung von MnH und CrH. Beide Moleküle wurden mittels Thermalisierung mit einem kryogenen Heliumgas gekühlt und anschließend magnetisch gespeichert. In diesen Experimenten wurden ca. 10^6 Moleküle in die Falle transferiert, wobei die maximalen Lebenszeiten von 120 ms (CrH) und 180 ms (MnH) bei relativ niedrigen Puffergasdichten beobachtet wurden. Bei höheren Heliumgasdichten verkürzten sich die Lebenszeiten und wurden vergleichbar mit der feldfreien Diffusion. Dieses Verhalten wurde mit der Hilfe einer numerischen Simulation des Kühl- und Speicherprozesses des Molekül-Ensembles untersucht. Mit diesem Modell ließen sich unsere experimentellen Beobachtungen gut reproduzieren. Dabei konnten hohe inelastische Streuquerschnitte für die Molekül-Helium Stöße konnten extrahiert werden. Diese verursachen eine große Anzahl von Spin-Flip Prozessen, wodurch längere Lebenszeiten in der magnetischen Falle verhindert werden, so dass die Moleküle nicht thermisch von der Zellwand isoliert werden konnten. Zusätzlich zur Bestimmung der inelastischen Streuquerschnitte, wurden in den Experimenten die elastischen Stoßquerschnitte für beide Moleküle vermessen.

Die Ergebnisse weisen darauf hin, dass das Einfangen von Molekülen mit einem Grundzustand hoher Multiplizität stark durch die Gegenwart

des Helium Puffergases eingeschränkt wird. Allerdings konnte experimentell bereits gezeigt werden, dass Helium nach dem Kühlprozess mittels einer kryogenen Aktivkohlepumpe innerhalb kurzer Zeit aus dem Bereich der Falle extrahiert werden kann [82]. Da die Zeiten für diese Extraktion kleiner sein können, als die bisher gemessenen Lebenszeiten in der Falle, könnte dadurch der Einfluss von Spin-Flip Stößen gemindert und längere Lebensdauern erzielt werden.

Appendix A: Numerical program for investigation of the trapping dynamics of atomic chromium

This section describes the numerical program used for fitting the absorption lines that are broadened by the inhomogeneous magnetic trapping field. With the help of this program, number density and temperature information of the atom ensemble is extracted. The discussion of the trapping dynamics in Section 4.3 is based on this data. For this, we simulate the spectrum of a thermal distribution of atoms in the trap, and vary the number and temperature until a χ^2 minimized fit is obtained. While this technique cannot be used with distributions of atoms that are far out of thermal equilibrium, it typically fits our data quite well.

Absorption of light crossing a unit cell

To calculate the transmission at a frequency ω of a sample of Cr atoms trapped in a magnetic quadrupole trap we make use of the Lambert-Beer law. Since both the absorption cross-section and the particle density are determined by the magnetic field we have to calculate the transmission through infinitesimal small unit cells that span up our detection volume. The light intensity I that gets transmitted through an infinitesimally

small volume $dzdrd\phi$ is given by:

$$I(\omega) = I_0 e^{-\epsilon N\sigma dz}, \tag{A.1}$$

where N is the number density, σ is the cross-section for absorption of radiation and ϵ a factor that describes the polarization dependence of absorption. For the density, we assume a Boltzmann distribution over the trapping field:

$$N(B(r,z),T) = N_0 e^{-\frac{\mu B(r,z)}{k_B T}}, \tag{A.2}$$

where N_0 is the particle density at the trap center, $\mu = 6\mu_B$ is the magnetic moment of Cr, T is the sample temperature and k_B the Boltzmann constant.

For the cross-section, we assume only natural lifetime broadening and use [156]:

$$\sigma(\omega) = 3\frac{\pi^2 c^2}{\omega_0^2} A_{21} g_H(\omega, \omega_0), \tag{A.3}$$

where A_{21} is the Einstein coefficient for stimulated absorption, ω_0 is the Zeeman shifted atomic resonance frequency, that is given by

$$\omega_0(B(r,z)) = (m_{Jf}g_f - m_{Jf}g_i)\mu_B B(r,z), \tag{A.4}$$

where g_f and g_i are the Landé factors of the final and the initial state, respectively and where m_{Jf} and m_{Ji} are the quantum numbers of the final and the initial magnetic sublevel, respectively and where $g_H(\omega, \omega_0)$ is a Lorentzian lineshape function given by

$$g_H(\omega, \omega_0) = \frac{1}{2\pi} \frac{\Gamma}{(\omega - \omega_0)^2 + \Gamma^2/4}, \tag{A.5}$$

where Γ is the FWHM scaling parameter. Also, σ needs to be multiplied by the Clebsch-Gordon coefficients for the specific transition used.

Selection rules

Selection rules state that in the presence of a magnetic field $\vec{B}$ circularly polarized light (σ^+) drives a $\Delta m_J = +1$ transition if the polarization

vector aligns with $\vec{B}$. We thus need to find out what fraction of our probe beam - which is linearly polarized - is σ^+ polarized and aligned with $\vec{B}$. Let a probe beam with linearly polarized light be characterized by $\vec{E}$ and the (local) magnetic field by $\vec{B}$. Since $\vec{E}$ is linearly polarized, $\vec{E}$ can be decomposed into two linearly polarized fields $\vec{E}_\parallel$ and $\vec{E}_\perp$, which are parallel and perpendicular to the direction of the magnetic field:

$$\vec{E} = \vec{E}_\parallel + \vec{E}_\perp \tag{A.6}$$

Since the $\vec{E}_\parallel$ only contains light whose polarization vector is parallel to $\vec{B}$ we leave it, for now, out of consideration. Light with the $\vec{E}$-field vector perpendicular to the quantization axis $\vec{B}$ can be decomposed into two components of oppositely circularly polarized light:

$$\vec{E}_{\sigma^+} = 1/2 \cdot \sqrt{2} \cdot ||\vec{E}_\perp||(\hat{k} + i\hat{l}) \tag{A.7}$$

$$\vec{E}_{\sigma^-} = 1/2 \cdot \sqrt{2} \cdot ||\vec{E}_\perp||(\hat{k} - i\hat{l}), \tag{A.8}$$

where i is an imaginary number, $\hat{k}$ and $\hat{l}$ are unit vectors and $\hat{k}, \hat{l} \perp \vec{B}$.

The intensity of the probe beam at any point can thus be written as

$$I = ||\vec{E}_\parallel||^2 + 1/2 \cdot ||\vec{E}_{\sigma^+}||^2 + 1/2 \cdot ||\vec{E}_{\sigma^-}||^2. \tag{A.9}$$

Because we retro-reflect our beam through the cell, the σ^+ and σ^- will become equivalent (or rather, what was σ^- light and did nothing for a $\Delta m_J = +1$ transition will become σ^+ light and vice-versa), and the probe beam gets attenuated to

$$I = ||\vec{E}_\parallel||^2 + ||\vec{E}_\perp||^2 e^{-N\sigma dz}. \tag{A.10}$$

We now need to derive the relative magnitude of $\vec{E}_\perp$. Let our axis system be span up by $\hat{x}$, $\hat{y}$ and $\hat{z}$. Let our propagation direction be coincident with $\hat{z}$ and the linear polarization pointing along $\hat{x}$. Let the magnetic field vector $\vec{B}$ be described by two Euler angles ϕ and θ, where ϕ is the polar angle in the plane span up by $\hat{x}$ and $\hat{y}$ and θ the azimuthal angle between $\vec{B}$ and $\hat{z}$. A scheme of this convention can be found in Figure A.1. Our conventions are that $\phi = 0$ when $\vec{B}$ is in the $\hat{x}$-$\hat{y}$-plane and $\theta = 0$ when $\vec{B}$ coincides with $\hat{z}$.
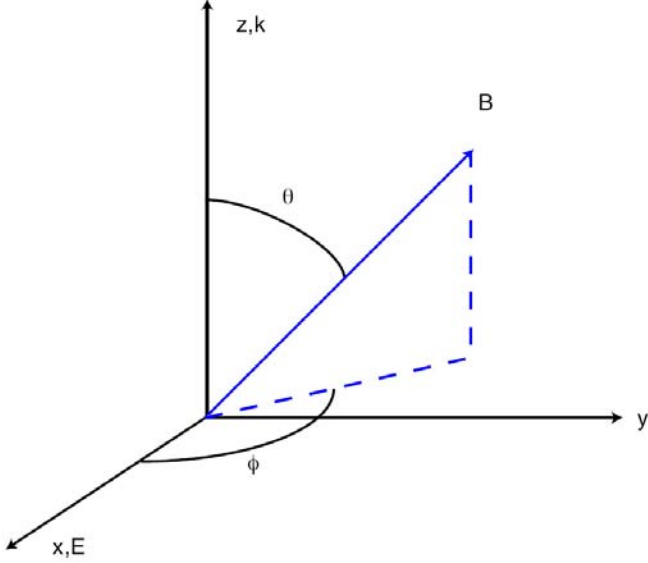
Figure A.1: Definition of our axis system. The electric field of the probe beam is polarized along the x-axis, the propagation direction points along the z-axis.

Decomposing the E-field vectors in components parallel and perpendicular to the quantization axis $\vec{B}$ yields:

$$\vec{E}_{\parallel} = (E_0 \hat{x} \cdot \vec{B})\hat{x} = E_0 \sin\theta\cos\phi\,\hat{x} \tag{A.11}$$

$$\vec{E}_{\perp} = E_0 \hat{x} \times \vec{B} = E_0 \cos\theta\,\hat{y} + E_0 \sin\theta\sin\phi\,\hat{z} \tag{A.12}$$

If we now assume $||\vec{E}_{\parallel}||^2 + ||\vec{E}_{\perp}||^2 = E_0^2 = I_0$, and enter equation A.11 and A.12 into A.10 we come to:

$$I/I_0 = \sin^2\theta\cos^2\phi + (\cos^2\theta + \sin^2\theta\sin^2\phi)e^{-N\sigma dz} \tag{A.13}$$

When $N\sigma dz << 1$, which is the case for infinitesimal small volumes, $e^{-N\sigma dz} \approx 1 - N\sigma dz$. This simplifies Equation A.13 to

$$I/I_0 = 1 - (\cos^2\theta + \sin^2\theta\sin^2\phi)N\sigma dz$$
$$\approx e^{-(\cos^2\theta+\sin^2\theta\sin^2\phi)N\sigma dz}. \tag{A.14}$$

Comparing this result with equation A.1 yields a polarization coefficient ϵ of

$$\epsilon = \cos^2\theta + \sin^2\theta\sin^2\phi. \tag{A.15}$$

Transmission of a light beam through the sample

At a position (r, ϕ) from the trap center, the transmitted power can be described by multiplying the transmission through an array of unit cells along the full length:

$$I = I_0 e^{-\int_L^L dz\epsilon N\sigma} \tag{A.16}$$

$$= I_0 e^{-\kappa(\omega,r,\phi)}, \tag{A.17}$$

where κ is the optical density of the sample.

The PMT signal

Since the recorded photomultiplier current signal S reflects the transmitted power of the whole beam we have to take the intensity distribution $I_0(r, \phi)$ of the beam into account. To obtain the measured signal we integrate this intensity distribution, convoluted with the optical density over the full beam profile, and for normalization divide this by the integrated intensity profile:

$$S = \frac{\int_0^{2\pi} d\phi \int_0^R rdr I_0(r,\phi)e^{-\kappa(\omega,r,\phi)}}{\int_0^{2\pi} d\phi \int_0^R rdr I_0(r,\phi)}, \tag{A.18}$$

where R is the radius of the beam.

For a uniform intensity distribution $I_0(r, \phi) = I_0$ this integral becomes

$$S = \frac{1}{\pi R^2} \int_0^{2\pi} d\phi \int_0^R r dr e^{-\kappa(\omega, r, \phi)}. \qquad (A.19)$$

The fitting procedure

The fitting procedure itself is an automated χ^2 minimization of the simulated spectrum with respect to the measured Cr absorption lines by variation of the following free parameters: the Boltzmann temperature T, the number density at the trapping center N_0 and the probe beam offset with respect to the trapping center r.

Appendix B: Zeeman spectroscopy on CrH

B.1 Introduction

Understanding the energy levels and Zeeman tuning of the $X^6\Sigma^+$ ($v = 0$) state of CrH is crucial for buffer-gas cooling and magnetic trapping. Fortunately, the field-free energy levels and magnetic tuning of the low-rotational levels of this state are known from laser magnetic resonance (LMR) [121] and mm-wave [157] pure rotational spectra. Modeling the field-free energies and magnetic tuning of the low-rotational levels ($N = 0$, 1 and 2) of the $A^6\Sigma^+$ ($v = 0$ and 1) state is also vital to the development of buffer-gas cooling and magnetic trapping of CrH because the intense (0, 0) band at 866 nm and the (1, 0) band at 767 nm of the $A^6\Sigma^+ - X^6\Sigma^+$ electronic transition are convenient for monitoring the spatial and temporal molecular concentrations of CrH in the trap. The (1, 0) band is of particular interest because it is at a convenient wavelength for excitation while the resulting off-resonant (1, 1) fluorescence near 874 nm can be selectively detected without interference from scattered laser light. Similar optical spectroscopic monitoring was performed in the buffer-gas cooling and trapping experiments for CaH [58].

Studying the Zeeman spectroscopy of the CrH molecules was done in collaboration with the group of Tim Steimle.[1] This Appendix is an

---

[1]Department of Chemistry and Biochemistry, Arizona State University, Tempe, USA

adaption of a paper [153] that was published as a result of the work that was done during a short visit to that group.

The field-free optical spectrum of a high-temperature sample of CrH has been thoroughly investigated at Doppler-limited resolution, motivated in part by its astrophysical importance [158]. The optical spectrum of a cold sample produced by supersonic expansion has been investigated using time-delayed resonant two-photon ionization spectroscopy [158] and moderate resolution laser induced fluorescence (LIF) [159]; a review of the spectroscopy of CrH can be found in these references as well. The high-resolution spectrum of the $A^6\Sigma^+-X^6\Sigma^+$ electronic transition is complex because each rotational level of the $A^6\Sigma^+$ and $X^6\Sigma^+$ states is split into up to six ($= 2S + 1$) fine structure components due to spin-rotation and spin-spin interactions. The fine structure splitting, which is dominated by second-order spin-orbit effects, is large in the $A^6\Sigma^+$ state because of the high-density of electronic states, giving rise to six spectrally distinct intense P and R branches. Each of these branch features exhibits a small, proton, magnetic hyperfine splitting, heretofore not resolved. The most abundant (84%) ^{52}Cr isotope has no nuclear spin. There have been no previous sub-Doppler field-free or Zeeman optical studies of the $A^6\Sigma^+-X^6\Sigma^+$ electronic transition and thus no analysis of the magnetic tuning or proton magnetic hyperfine splitting of the optical lines.

Modelling the $A^6\Sigma^+-X^6\Sigma^+$ spectra with an effective Hamiltonian has been difficult because of strong perturbations in the $A^6\Sigma^+$ state by, primarily, the $A^4\Sigma^+$ state. The $A^4\Sigma^+$ ($v = 0$) vibronic state has been experimentally determined [160] to lie only 367 cm^{-1} below the $A^6\Sigma^+$ ($v = 0$) state and causes local perturbations that maximize near $N \approx 9$ and $N \approx 21$ in the $A^6\Sigma^+$ ($v = 0$) vibronic state. The $A^6\Sigma^+$ ($v = 1$) vibronic state exhibits more extensive local perturbations from the $A^4\Sigma^+$ ($v = 1$) vibronic state that affect even lower ($N = 1$) rotational levels [159]. In addition to the local perturbations, the $A^6\Sigma^+$ state exhibits homogeneous perturbations that contaminate the integrity of the $^6\Sigma^+$ state designation. *Ab initio* electronic structure calculations [161, 162, 163] predict that in addition to the $A^4\Sigma^+$ and $A^6\Sigma^+$ states, which correlate to the same dissociation limit of Cr(^{5}S ($3d^54s^1$)) + H(^{2}S), there are $^{4,6}\Delta$, $^{4,6}\Gamma$ and $^{4,6}\Sigma^+$ states that correlate in the

dissociation limit to $\text{Cr}(^5\text{D}\ (3\text{d}^4 4\text{s}^2)) + \text{H}(^2\text{S})$ with similar energy. The recently discovered $\text{B}^6\Pi$ state near the $\text{A}^6\Sigma^+$ ($v = 1$) vibronic state [159] is likely a member of this latter group.

To a first approximation, the magnetic tuning of a level can be predicted from the associated $^{2S+1}\Lambda$ term symbol and the eigenvalues and eigenvectors as derived from field-free parameters. Specifically, if it is assumed that $\text{X}^6\Sigma^+$ and $\text{A}^6\Sigma^+$ states are isolated Born-Oppenheimer states in the Hund's case (b) limit (*i.e.* the electron spin is not coupled to the molecular axis) then upon application of a magnetic field each rotational level, N, splits into six ($= 2S + 1$) degenerate groups of $2N + 1$ levels. The tuning of each group is linear in magnetic field strength, B and is given by $g_S \mu_B B M_s$, where g_S is the electronic spin g-factor ($= 2.002$), μ_B is the Bohr magneton and m_S is the projection of the total electron spin on the quantization axis defined by the magnetic field. In reality the spin-rotation and spin-spin interactions in the $\text{X}^6\Sigma^+$ and $\text{A}^6\Sigma^+$ states of CrH are significant and the electron spin is not completely decoupled from the molecular axis even at high trapping fields (~ 2 T). Modeling the Zeeman effect is still, in principle, a straightforward process of accounting for the decoupling of the electron spin from the molecular frame and re-coupling to the laboratory frame. Unfortunately, the fact that the spin-rotation and spin-spin interactions in the $\text{X}^6\Sigma^+$ and $\text{A}^6\Sigma^+$ states are large indicates that the "goodness"of the Λ and Σ quantum numbers implied by the $^{2S+1}\Lambda$ term symbol is diminished from that of an isolated Born-Oppenheimer vibronic state. Born-Oppenheimer breakdown is particularly large for the eight nearly degenerate excited electronic states making an *a priori* prediction of the magnetic tuning of the $\text{A}^6\Sigma^+ - \text{X}^6\Sigma^+$ spectral features impossible. Thus, an experimental measurement is required for determination of the optical Zeeman effect, the analysis of which gives insight into the nature of the multitude of interacting states.

The character of an electronic state may also be deduced from the analysis of the magnetic hyperfine interactions because these interactions depend upon the spatial distribution and spin density of the valence electrons at the proton. The determinable Fermi-contact, b_F, and dipolar,

c, parameters are related to the coordinates of the electron by:

$$b_F = \left(\frac{\mu_0}{4\pi h}\right)\left(\frac{8\pi}{3}\right)g_e g_N \mu_B \mu_N \frac{1}{S} \times \langle \Lambda\Sigma = S| \sum_i \hat{s}_{zi}\delta_i(r)|\Lambda\Sigma = S\rangle_S$$

(B.1)

$$c = \left(\frac{\mu_0}{4\pi h}\right)\frac{3}{2}g_e g_N \mu_B \mu_N \frac{1}{S} \times \langle \Lambda\Sigma = S| \sum_i \hat{s}_{zi}\frac{3\cos^2\theta_i - 1}{r_i^3}|\Lambda\Sigma = S\rangle_S$$

(B.2)

In Equations B.1 and B.2 Λ and Σ are the projection of total electronic orbital, $\mathbf{L}$, and spin, $\mathbf{S}$, angular momenta, respectively, on the internuclear axis. $\delta(r)$ is the Dirac delta function and r_i and θ_i are spherical polar coordinates of the electron relative to the proton. The proton b_F (-34.8 MHz) and c (42.3 MHz) parameters are small for the $X^6\Sigma^+$ state [121, 157] because the unpaired electrons are primarily centered on the Cr nucleus. The negative value of b_F for the $X^6\Sigma^+$ state indicates that this term is dominated by spin-polarization of the CrH σ-bond and not direct spin density of the Cr-centered valence electrons at the proton. Changes to b_F and c upon excitation to the $A^6\Sigma^+$ state reflect subtle modifications to the electron distribution in the vicinity of the proton due to an alteration of the Cr-centered electrons.

B.2 Measurements

The measurements were not performed in our cryogenic setup, but in in a molecular beam machine. This apparatus consists of several differentially pumped beam chambers. In this machine, a cold sample of chromium monohydride was generated by laser ablating a solid chromium metal rod in a supersonic expansion, where pure hydrogen gas instead of an argon/methane mixture was used as the reacting expanding gas. The typical conditions were 20 atm backing pressure, and 5 mJ of loosely focused 355 nm radiation from a Q-switched Nd:YAG laser. The supersonic free jet expansion was skimmed to produce a collimated molecular beam. Approximately 30 mW of lightly focused power derived from a

Table B.2: Field-free transition wavenumbers for the $A^6\Sigma^+ - X^6\Sigma^+$ bands of CrH (in cm^{-1})

single longitudinal mode cw-Ti:sapphire laser was used to excite the (0, 0) and (1, 0) bands of the $A^6\Sigma^+ - X^6\Sigma^+$ transition near 866 and 767 nm, respectively. The resulting laser induced fluorescence (LIF) was collected through a 870 ± 10 nm band pass filter and detected with a cooled GaAs photomultiplier tube. Photon counting techniques were used to process the signal.

Static homogeneous magnetic fields up to 1100 Gauss were generated using a homemade electromagnet. This consisted of a pair of Helmholtz coils with ferromagnetic poles through which 12 mm holes were drilled to allow for the passage of the molecular beam [164]. The field was calibrated using a commercial Gauss meter. A polarization rotator and polarizing filter were used to orient the electric field vector of the linearly polarized laser radiation either parallel or perpendicular to the static magnetic field resulting in $\Delta m_J = 0$ or $\Delta m_J = \pm 1$ selection rules, respectively. The Zeeman-induced shifts and splittings were determined by simultaneously recording the transmission of the excitation laser through a temperature and pressure stabilized confocal etalon with a free spectral range of 753.58 MHz [164].

B.3   Observations

The various spin fine structure components having identical parity and space fixed projection quantum numbers are mixed by the application of a magnetic field because the Zeeman Hamiltonian operator does not commute with the total angular momentum operator. Accordingly, the field-free spectra of numerous low-N branch features in the (0, 0) and (1, 0) bands of the $A^6\Sigma^+ - X^6\Sigma^+$ transition were recorded and analyzed to obtain the field-free relative energies of the fine structure components. Ten and fourteen of the possible 18 branch features in the $A^6\Sigma^+ - X^6\Sigma^+$(0, 0) and $A^6\Sigma^+ - X^6\Sigma^+$(1, 0) band, respectively, that have either $N'' = 0$ or 1 were precisely measured field-free and are listed in Table B.2. The branch labeling scheme is $^{\Delta N}\Delta J_{F_i' F_i''}(N'')$ which is identical to that used

Assignment			(0,0)		(1,0)	
	F″	F′	Observed[1]	Obs-calc	Observed[2]	Obs-calc
$^PQ_{12}(1)$	2	2			18.6490	-0.0303
	3	2			18.6507	-0.0305
	2	3			18.6507	-0.0303
	3	2			18.6526	-0.0303
$P_1(1)$	3	2	38.6635	-0.0004	19.7840	-0.0265
	3	3	38.6649	-0.0005	19.7856	-0.0267
	4	3	38.6691	-0.0002	19.7897	-0.0264
$^PR_{13}(1)$	1	2			20.6322	-0.0243
	2	2			20.6358	-0.0245
	2	3			20.6379	-0.0241
$^RP_{31}(0)$	2	1	52.5663	-0.0347	33.6034	0.0789
	2	2	52.5677	-0.0346	33.6050	0.0788
	3	2	52.5712	-0.0347	33.6086	0.0788
$^RP_{53}(1)$	1	0	55.6380	0.0286	35.9234	-0.2664
	2	1	55.6425	0.0283	35.9278	-0.2670
$^RP_{42}(1)$	2	1			41.5052	0.1107
	3	2			41.5087	0.1106
$^RQ_{43}(1)$	1	1	62.8942	0.0088	43.4766	0.1049
	1	2			43.4782	0.1048
	2	1			43.4804	0.1049
	2	2	62.8996	0.0088	43.4820	0.1048
$R_1(0)$	2	3	63.4162	0.00283	44.3863	0.0513
	3	3	63.4201	0.00318	44.3899	0.0513
	3	4	63.4213	0.00317	44.3914	0.0513
$^RQ_{21}(0)$	2	2	67.7888	0.0256	49.7317[3]	1.1784
	2	3	67.7910	0.0255	49.7348[3]	1.1789
	3	2	67.7918	0.0251	49.7348[3]	1.1779
	3	3	67.7948	0.0257	49.7378[3]	1.1784
$^RP_{31}(1)$	2	2			52.1500	0.0099
	3	2			52.1521	0.0100
	2	3			52.1521	0.0096
	3	3			52.1542	0.0098
$R_3(1)$	1	2			54.1027	-0.0146
	2	2			54.1065	-0.0146
	2	3			54.1090	-0.0145
$^RQ_{32}(1)$	2	2	71.7568	-0.0414		
	3	3	71.7610	-0.0415		
$R_1(1)$	3	4	75.1370	0.0083	55.5957	0.0212
	4	4	75.1411	0.0086	55.5999	0.0215
	4	5	75.1421	0.0085	55.6014	0.0216
$R_2(1)$	2	3	76.1446	-0.0230	56.4570	-0.0432
	3	3	76.1467	-0.0228	56.4591	-0.0430
	3	4	76.1483	-0.0230	56.4611	-0.0429
$^RQ_{21}(1)$	3	3	77.3014	0.0025	57.5928	-0.0387
	3	4			57.5946	-0.0388
	4	3			57.5966	-0.0387
	4	4	77.3071	0.0026	57.5987	-0.0386

| Std. dev. of fit: | 0.0216 cm^{-1} | 0.084 cm^{-1} |

[1] Observed transition wave number – 11500.0000 cm^{-1}.
[2] Observed transition wave number – 13000.0000 cm^{-1}.
[3] Strongly perturbed and not included in fit.

in Ref. [159]. The "F_i"subscript takes on values of 1 to 6 for $J = N + S$ through $N - S$, respectively. Of the current set of spectral lines, only the $R_1(0)$, $R_1(1)$ and $R_2(1)$ features of the $A^6\Sigma^+ - X^6\Sigma^+(0, 0)$ band had been measured previously in the Doppler-limited recording [160]. In the $A^6\Sigma^+ - X^6\Sigma^+(1, 0)$ band all but the $^RQ_{32}(1)$ branch feature had been measured previously [159], but at somewhat lower precision and resolution.

The observed and predicted spectra of the $^RQ_{21}(0)$ $A^6\Sigma^+ - X^6\Sigma^+(0, 0)$ branch feature are presented in Figure B.3 along with the energy level pattern and quantum number assignment. The spectrum consists of two intense $\Delta F = \Delta J$ transitions and weaker $\Delta F \neq \Delta J$ features, where F is the total angular momentum. The field-free spectra were recorded from which proton magnetic hyperfine spitting in the $N = 0$ and 1 levels of the $A^6\Sigma^+(v = 0$ and 1) vibronic states were obtained by combination/difference and using the known splittings for the $X^6\Sigma^+(v = 0)$ state [157]. The determined splittings and quantum number assignments are given in Table B.4.

The $P_1(1)$, $^RP_{31}(0)$, $^RQ_{21}(0)$, and $R_1(0)$ lines of the $A^6\Sigma^+ - X^6\Sigma^+(0, 0)$ band system and the $P_1(1)$, $^PQ_{12}(1)$, $^PR_{13}(1)$, $^RP_{31}(0)$, $^RQ_{21}(0)$ and $R_1(0)$ lines of the $A^6\Sigma^+ - X^6\Sigma^+$ (1, 0) band system were selected for Zeeman measurements because these features probe all of the spin components (F_1, F_2 and F_3) of the $N = 0$ and 1 rotational levels in the $A^6\Sigma^+$ vibronic states. The $R_1(0)$ branch feature of the $A^6\Sigma^+ - X^6\Sigma^+$ (1, 0) band is the most ideally suited for monitoring CrH in magnetic traps because it is associated with the lowest energy level, has the largest line strength factor and fluoresces off-resonant at 874 nm. Spectra of the $P_1(1)$ line in the $A^6\Sigma^+ - X^6\Sigma^+$ (0, 0) and (1, 0) band systems observed field-free and in the presence of a magnetic field oriented parallel ($\Delta m_J = 0$) to the laser field are presented in Figure B.5. The assignments of the Zeeman spectral features of Fig. B.5 are presented in Fig. B.6 as are the energy levels as a function of magnetic field strength. The intense low wavenumber feature of the field-free spectra in Fig. B.5 is the $F'' = 3 \rightarrow F' = 2$ transition and the intense high wavenumber feature is the $F'' = 4 \rightarrow F' = 3$ transition. The weak, partially resolved, shoulder on the low wavenumber feature is the $F'' = 3 \rightarrow F' = 3$ transition. The hyperfine splitting is too small to discern in the energy level plots of
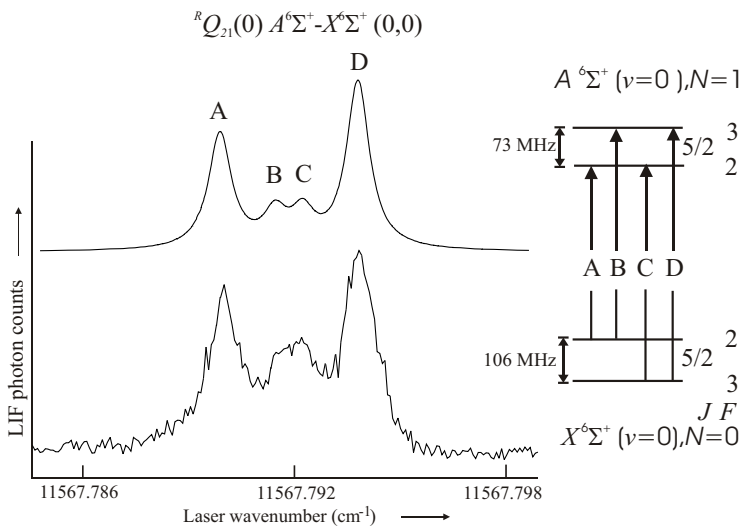
Figure B.3: The observed (lower) and predicted (upper) field-free spectra for the $^{R}Q_{21}(0)$ branch feature of the $A^6\Sigma^+ - X^6\Sigma^+(0, 0)$ band along with the energy level pattern and quantum number assignment. The predicted spectrum has been shifted by -0.0255 cm^{-1}, to correct for a small local perturbation (see Table B.2).

Fig. B.6. As is evident from Fig. B.5 and B.6, the Zeeman tuning of the $N = 0$, $J = 5/2$ (F_1) levels of $A^6\Sigma^+(v = 0)$ and $A^6\Sigma^+$ ($v = 1$) is significantly different. Also evident from Fig. B.6 is that the electron spin in the $A^6\Sigma^+(v = 0)$, $A^6\Sigma^+(v = 1)$ and $X^6\Sigma^+(v = 0)$ states is still coupled to the molecular axis even at 4000 G and the approximately good quantum numbers are m_J and m_I, but not m_S. The uncoupling of the electron spin from the molecular axis results in a re-ordering into a pattern of six ($= 2m_S + 1$) distinct groups of levels [130] which is not evident in Fig. B.6.

A total of 398 Zeeman shifted components were recorded at field strengths ranging from 424 to 1095 Gauss for the $A^6\Sigma^+ - X^6\Sigma^+(0, 0)$ band system. Similarly, at numerous field strengths ranging from 315 to

N	J	$A^6\Sigma^+(v=0)$ Obs.[a]	Obs-calc	$A^6\Sigma^+(v=1)$ Obs.	Obs-calc
0	5/2	40	-3	51	-4
1	3/2	42	4	45	-4
1	5/2	74	3	78	2
1	7/2	35	-1	47	-1
2	1/2	23	-6		
2	3/2	47	0	46	-4
2	5/2	66	-3	72	1
2	7/2	54	1	60	1
2	9/2	35	4	52	7
σ:		4 MHz		5 MHz	
Parameters		b_F=19(2)MHz; c=34(7)MHz		b_F=22(2)MHz; c=28(8)MHz	

Table B.4: The proton magnetic hyperfine splitting in the $A^6\Sigma^+$ state of CrH (in MHz).
[a] The upper energy level has total angular momentum $F = J + 1/2$.

983 Gauss, the Zeeman shifted components corresponding to the spectral features in the $A^6\Sigma^+ - X^6\Sigma^+(1, 0)$ band system were measured. This data consisted of 362 features associated with the $N = 0$, $J = 5/2$ (F_1), 80 associated with the $N = 1$, $J = 3/2$ (F_3), 165 associated with the $N = 1$, $J = 5/2$ (F_2), and 216 associated with the $N = 1$, $J = 7/2$ (F_1), spin components of the $A^6\Sigma^+(v = 1)$ state.

B.4 Analysis

B.4.1 Field-free energies

The Zeeman operator mixes the fine structure components. Therefore, accurately modeling the relative field-free energy spacing is a prerequisite for the analysis of the Zeeman effect. The field-free energy levels of the $A^6\Sigma^+$ ($v = 0$ and 1) and $X^6\Sigma^+$ ($v = 0$) vibronic states were modeled using an effective Hamiltonian operator identical to that
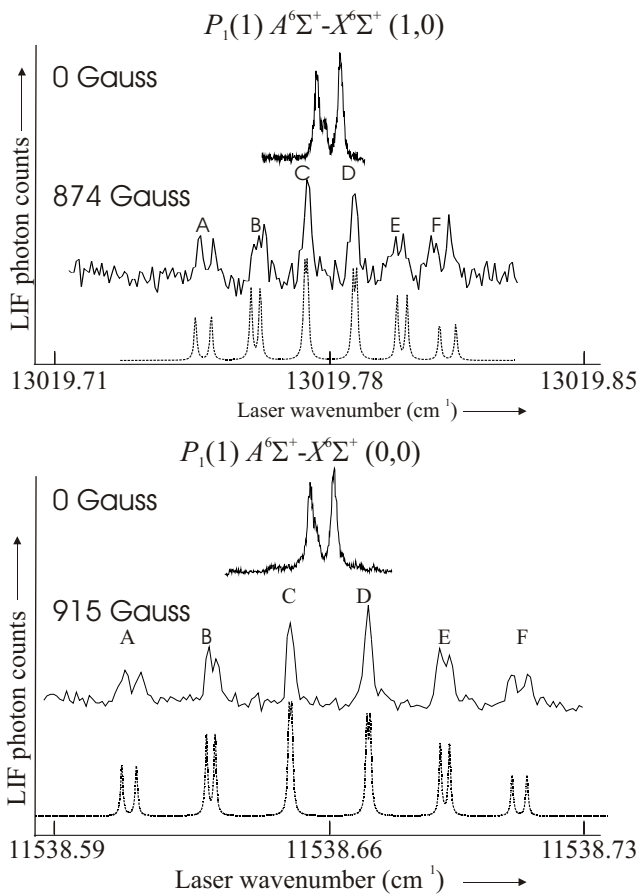
Figure B.5: The $P_1(1)$ line in the $A^6\Sigma^+ - X^6\Sigma^+$ (1, 0) and (0, 0) band systems observed field-free and in the presence of a magnetic field oriented parallel ($\Delta m_J = 0$) to the laser field. The dotted lines are predicted spectra generated using optimized field-free parameters and g_S-factors for the $A^6\Sigma^+$ state given in Tables B.7 and B.8. The spectroscopic parameters for the $X^6\Sigma^+$ ($v = 0$) state were constrained to those of Ref. [9]. The predicted spectrum of the $P_1(1)$ line in the $A^6\Sigma^+ - X^6\Sigma^+$ (1, 0) branch has been shifted by 0.0267 cm^{-1}, to correct for a small local perturbation (see Table B.2).
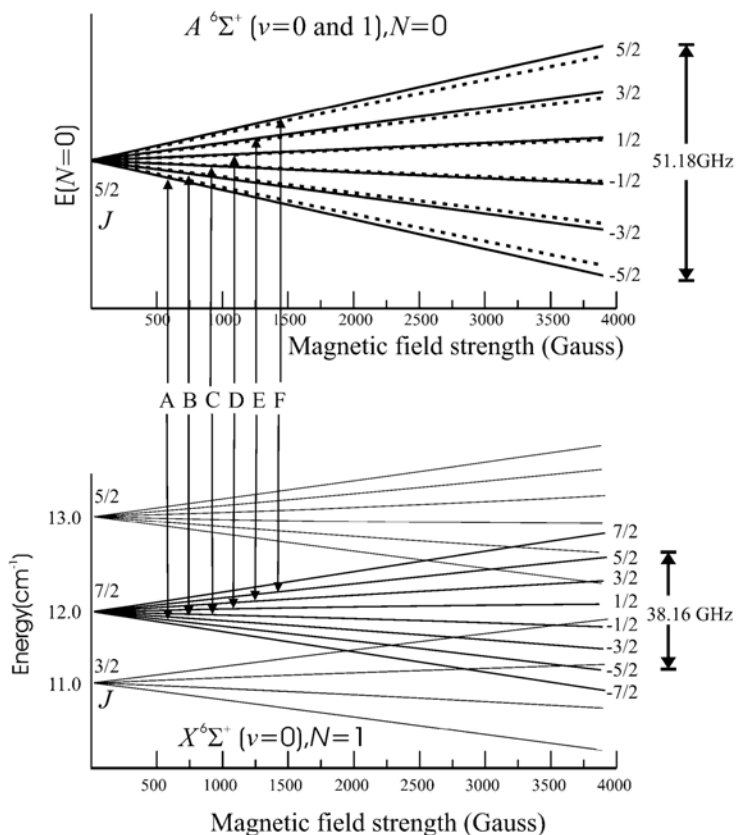
Figure B.6: The predicted energy levels as a function of magnetic field strength and the quantum number assignment of the spectral features presented in Fig. B.5. The solid lines are levels of the $A^6\Sigma^+$ $(v = 0)$ vibronic state and dotted lines are for levels of the $A^6\Sigma^+$ $(v = 1)$ vibronic state. The field-free energies, $E(N = 0)$, of the $A^6\Sigma^+$ $(v = 0)$ of the $A^6\Sigma^+$ $(v = 1)$ vibronic states are 11552.64 and 13031.87 cm^{-1}, respectively. The magnetic tuning in the $A^6\Sigma^+$ $(v = 1)$ state is considerably less than that of the $A^6\Sigma^+$ $(v = 0)$ state because of mixing with the a $^4\Sigma^+$ state.

of Ref. [121] and [157]. This operator is

$$\mathbf{H_{eff}}(^6\Sigma^+) = B\mathbf{N}^2 - D\mathbf{N}^4 + \gamma\mathbf{N}\cdot\mathbf{S} + \frac{1}{2}\gamma_D[\mathbf{N}\cdot\mathbf{S},\mathbf{N}^2]_+$$
$$+10\gamma_S T^3(\mathbf{L}^2,\mathbf{N})\cdot T^3(\mathbf{S},\mathbf{S},\mathbf{S})/[\sqrt{6}\langle\Lambda|T_0^2(\mathbf{L}^2)|\Lambda\rangle]$$
$$+\frac{2}{3}\lambda(3S_z^2 - \mathbf{S}^2) + \frac{1}{3}\lambda_D[3S_z^2 - \mathbf{S}^2,\mathbf{N}^2]_+ \qquad (\text{B.3})$$
$$+\frac{1}{12}\Theta[35S_z^4 - 30\mathbf{S}^2 S_z^2 + 25S_z^2 - 6\mathbf{S}^2 + 3\mathbf{S}^4]b_F(H)\mathbf{I}\cdot\mathbf{S}$$
$$+c(H)(\mathbf{I}_z\mathbf{S}_z - \frac{1}{3}\mathbf{I}\cdot\mathbf{S})$$

In this equation, γ and λ are the spin-rotation and spin-spin parameters, respectively and associate centrifugal distortion correction to these parameters are γ_D and λ_D. The parameter Θ multiplies the operator that accounts for the diagonal terms of the fourth-order spin-orbit interaction and the γ_S parameter multiplies the operator that accounts for third order spin rotation. The high-order Θ and γ_S parameters are orders of magnitude smaller than γ and λ.

The eigenvalues and vectors for the X$^6\Sigma^+$ ($v = 0$) and A$^6\Sigma^+$ ($v = 0$ and 1) states were obtained by a numerical diagonalization of a 12 × 12 matrix representation of the $\mathbf{H^{eff}}$, constructed using a Hunds case (a$_{\beta J}$), non-parity basis set, $\Psi = |n\Lambda; S\Sigma; J\Omega IF M_F\rangle$. The predicted pure rotational transition frequencies given in Ref. [157] for the X$^6\Sigma^+$ ($v = 0$) state were reproduced using the previously published spectroscopic parameters as a check of the procedure. Determination of an optimum set of field-free parameters for the X$^6\Sigma^+$ ($v = 0$ and 1) states was achieved in a two step procedure. First, the proton hyperfine structure parameters ($b_F(H)$ and $c(H)$) for the A$^6\Sigma^+$ ($v = 0$ and 1) states were obtained using the measured splittings given in Table B.4 as input into a nonlinear least squares fitting program. The magnetic hyperfine splittings are relatively insensitive to the fine structure parameters. Therefore, in this step the fine structure parameters (B, γ, γ_S, λ,) were constrained to the previously published [159, 160] values. In the second step, these fine structure parameters and the origin, T_v, for the A$^6\Sigma^+$ ($v = 0$ and 1) states were optimized using a non-linear least squares fit of the measured

optical transitions given in Table B.2, excluding the strongly perturbed $^RQ_{21}(0)$ line of the (1, 0) band. In this fit all the ground state parameters were held fixed to those of Ref. [157] and the excited state magnetic hyperfine parameters were held fixed to those derived in the first step. The data set was too restricted for the determination of g_S and it was constrained to zero. The final set of optimized parameters and those previously obtained [159, 160] are given in Table B.7.

	$A^6\Sigma^+(v=0)$		$A^6\Sigma^+(v=1)$	
Parameter	Present[a]	Ref. 17	Present[b]	Ref. 16
T_v	11552.635(13)	11552.68416(75)	13032.9233(99)	13034.045(203)
B	5.2831(28)	5.272000(18)	5.1629(94)	5.1131(154)
γ	1.2974(19)	1.302067(70)	1.2931(66)	1.2870(315)
λ	1.5782(22)	1.57553(22)	1.5524(81)	1.5496(414)

Table B.7: Optimized spectroscopic parameters for the $A^6\Sigma^+$ state of CrH (in cm^{-1}).
[a] From a least squares fit of the transition wave numbers for the (0,0) band listed in Table B.2.
[b] From a least squares fit of the transition wave numbers for the (1,0) band listed in Table B.2 except for the $^RQ_{21}(0)$ line.

As is evident from Table B.2, all but the $N = 1$, $J = 5/2$ (F_2) energy level, which is the upper energy terminus of the $^RQ_{21}(0)$ branch feature, are fairly accurately predicted using the effective Hamiltonian approach. Except for, possibly, this energy level, the small discrepancies associated with using the derived effective parameters for the $A^6\Sigma^+$ ($v = 0$ and 1) states will not affect modeling the observed Zeeman effect. Note that the determined parameters only serve as a convenient method for modeling the field-free eigenvalues and eigenvectors as required for the analysis of the Zeeman effect and should not be used to extract other properties (*e.g.* bond distance) of the $A^6\Sigma^+$ ($v = 0$ and 1) states.

B.4.2 The Zeeman effect

The effective Hamiltonian operator for the Zeeman effect in the $A^6\Sigma^+$ ($v = 0$ and 1) and $X^6\Sigma^+$ ($v = 0$) vibronic states was taken as [165, 166]:

$$\mathbf{H_{Zeeman}}(^6\Sigma) = g_S\mu_B\mathbf{S}\cdot\mathbf{B} + g_l\mu_B(S_xB_x + S_yB_y) - g_R\mathbf{N}\cdot\mathbf{B} \quad \text{(B.4)}$$

In the effective Hamiltonian model, g_S is allowed to deviate from 2.002 to account for non-adiabatic contributions. The other Zeeman parameters in Equation B.4, are the anisotropic g-factor, g_l and the rotational g-factor, g_R. The small magnetic contribution due to the proton nuclear spin has been ignored. Whereas there is no *a priori* method for estimating g_R, g_l can often be adequately approximated for a Σ state by the Curl relationship [166]:

$$g_l \approx -\gamma/2B \quad \text{(B.5)}$$

where B and γ are the rotation and spin-rotation parameters, respectively. The combined analysis of the mm-wave and LMR spectra [121, 157] yielded values 2.001623(31), -4.118(41) $\times$ 10^{-3} and -1.247(18) $\times$ 10^{-3} for g_S, g_l and g_R, respectively, in the $X^6\Sigma^+$ ($v = 0$) vibronic state. The Curl relationship predicts a value for g_l of -4.10 $\times$ 10^{-3} and supports the use of this approximate relationship for CrH.

The matrix representation of $\mathbf{H_{Zeeman}}$ is of infinite dimension and block diagonal in total angular momentum projection quantum number, M_F. The Zeeman effect in the $N = 0$ and 1 levels of the $X^6\Sigma^+$ ($v = 0$) and $A^6\Sigma^+$ ($v = 0$ and 1) vibronic states were accurately modeled by truncating the dimension of the representation to include only the $F = 0$, 1, 2, 3 and 4 field-free states which results in a 60×60 non-parity case ($a_{\beta J}$) matrix representation. The transition wavenumbers were calculated field-free and in the presence of the magnetic field strength by taking the difference of appropriate eigenvalues obtained by numerical diagonalization of the 60×60 matrices for the $X^6\Sigma^+$ and $A^6\Sigma^+$ states. Zeeman shifts of the optical spectra were predicted and used as input into a non-linear least squares fitting procedure. In the end, the non-adiabatic parameters, γ_l, were held fixed to the values predicted by the Curl relationship: -0.1235 and -0.1238 for the $A^6\Sigma^+$ ($v = 0$) and $A^6\Sigma^+$ ($v = 1$) states, respectively. The rotational term, γ_R, was constrained to zero. The final optimized set of γ_S-factors for the $A^6\Sigma^+$ ($v = 0$ and 1) states is presented in Table B.8.

$A^6\Sigma^+(v=0)$			$A^6\Sigma^+(v=1)$	
g_s[a]	σ(MHz)[b]		g_s[c]	σ(MHz)[b]
2.0081(20)	40	$N=0, J=5/2$	1.7468(17)	38
		$N=1, J=3/2$	1.8760(30)	25
		$N=1, J=5/2$	1.7208(28)	31
		$N=1, J=7/2$	1.9123(25)	31

Table B.8: Optimized magnetic g_S-factors for the $A^6\Sigma^+$ state of CrH.
[a] A simultaneous fit of the Zeeman shifts for the $P_1(1)$, $^RP_{31}(0)$, $^RQ_{21}(0)$, and $R_1(0)$ lines of the $A^6\Sigma^+-X^6\Sigma^+$ (0,0) band.
[b] Standard deviation of the fit.
[c] Individual fits of the Zeeman shifts. The $P_1(1)$, $^PQ_{12}(1)$, $^PR_{13}(1)$ lines for the $N = 0$, $J = 5/2$ level; the $^RP_{31}(0)$ line for the $N = 1$, $J = 3/2$ level; the $^RQ_{21}(0)$ line for the $N = 1$, $J = 5/2$ level; the $R_1(0)$ line for the $N = 1$, $J = 7/2$ level.

B.5   Discussion

A primary objective was to characterize the Zeeman tuning of the optical transitions that are used for monitoring CrH in buffer-gas cooling and magnetostatic trapping experiments as described in Chapter 6. The predicted intense $R_1(0)$ branch features of the $A^6\Sigma^+-X^6\Sigma^+$ (0, 0) and (1, 0) band systems are most ideally suited for monitoring CrH in magnetic traps. The predicted spectra of the $R_1(0)$ branch feature of the $A^6\Sigma^+-X^6\Sigma^+$ (1, 0) band system over a range of magnetic field strengths from 0 to 0.8 T and with an orientation parallel ($\Delta m_J = 0$) to the laser field are presented in Fig. B.9. The observed spectra recorded field-free and in the presence of a 0.09 T field are also presented. The optimized parameters for the $A^6\Sigma^+$ state given in Tables B.7 and B.8 and the ground state parameter of Ref. [157] were used for these predictions. Upon the application of only a modest magnetic field, the $R_1(0)$ spectrum splits into six ($= 2J'' + 1$) sets of closely spaced doublets because the proton nuclear spin is easily de-coupled from the molecular axis and hence m_J and m_I become the approximately good quantum numbers. The tuning of the six components, labeled "A" through "F" in Fig. B.9, over the 0.1 to 0.8 T range, are plotted on the right hand side of Fig. B.9. They exhibit significant non-linearity because the electron spin, S, is decoupling from the molecular axis at different rates in the $N = 1$,

$J = 7/2$ (F_1) level of the $A^6\Sigma^+$ $(v = 1)$ state and the $N = 0$, $J = 5/2$ (F_1) level of the $X^6\Sigma^+$ states upon application of the magnetic field. The predicted tuning of each of the six spectral features of the $R_1(0)$ branch feature of the $A^6\Sigma^+$-$X^6\Sigma^+$ (0, 0) and (1, 0) band systems were fit to a second-order polynomial, the results of which are presented in Table B.10. These parameters should reliably predict the magnetic tuning over the fields that are typically used in a magnetic trap.

The Zeeman tuning of all the probed levels in the $A^6\Sigma^+$ $(v = 1)$ state is slower than that expected for a state of pure $^6\Sigma^+$ character and accordingly the determined effective g_S-factors are less than 2.002. The largest deviation of the determined g_S-factor from the expected value of 2.002 is for the $N = 1$, $J = 5/2$ (F_2) level of the $A^6\Sigma^+$ $(v = 1)$ state which is the level that also exhibits the strongest field-free energy perturbation (see Table B.2 and Ref. [161]) suggesting that mixing with the $a^4\Sigma^+$ state is responsible for the slower than expected tuning. The determined relative magnitudes of the deviations from 2.002 for the four levels of the $^6\Sigma^+$ $(v = 1)$ state probed can be used to identify the nature of the perturbing states. The appropriate perturbation selection rules for the change in angular momentum is $\Delta J = 0$, because the magnetic hyperfine interaction is very small. The selection rule for parity is $\pm \leftrightarrow \pm$. For the case of a $^6\Sigma^+ \sim^4 \Sigma^+$ interaction, the additional selection rules are $\Delta N = 0, 2$ and 4 [160]. Thus the $N = 1$, $J = 5/2$ (F_2) level of the nominal $^6\Sigma^+$ $(v = 1)$ state can interact with the $N = 1$, $J = 5/2$ (F_1) and $N = 3$, $J = 5/2$ (F_3) levels of the nominal $a^4\Sigma^+$ state. Evidently the $N = 1$, $J = 5/2$ (F_1) and $N = 3$, $J = 5/2$ (F_3) levels of the nominal $a^4\Sigma^+$ state tune more slowly than those of the $N = 1$, $J = 5/2$ (F_2) level of the nominal $^6\Sigma^+$ $(v = 1)$ state. The tuning of these three levels will be given approximately by the expectation value of $\mathbf{H_{Zeeman}}$ in a Hunds case b wavefunction. Using the expression for the matrix elements of Ref. [166] this expectation value is:

$$\langle Case\, b|\mathbf{H_{Zeeman}}(^6\Sigma^+)|Case\, b\rangle = g_J\mu_B B_z m_J$$
$$= g_S\frac{S(S+1) + J(J+1) - N(N+1)}{2J(J+1)}\mu_B B_z m_J \qquad \text{(B.6)}$$

Effective g_J-factors predicted by this equation for the $N = 1$, $J = 5/2$ (F_2) level of a $^6\Sigma^+$ state and the $N = 1$, $J = 5/2$ (F_1) and $N =$
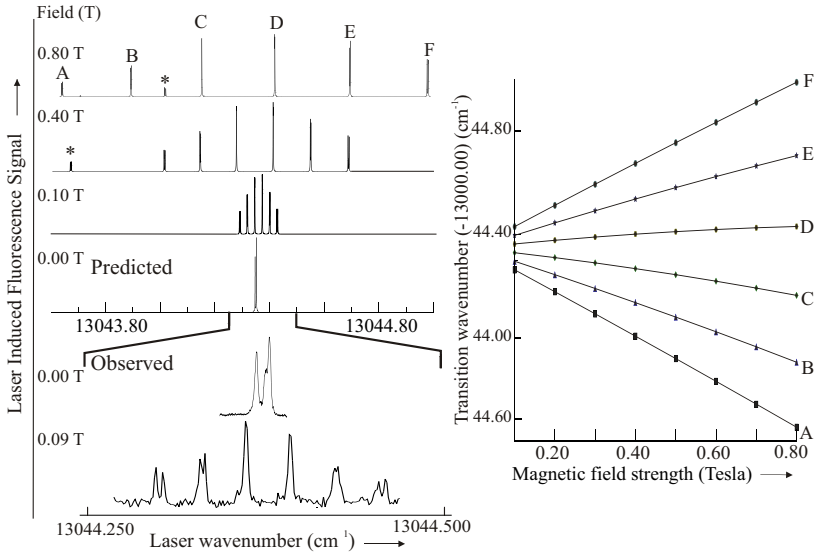
Figure B.9: The observed and predicted $R_1(0)$ line of the A$^6\Sigma^+$−X$^6\Sigma^+$ (1, 0) band system for parallel polarization as a function magnetic field strength (left panel). On the right hand side is a plot of the tuning character of spectral feature "A" through "F" over the range 0.1 T to 0.8 T. The solid lines are the tuning curves predicted from the second order polynomial fit of the predicted shifts. The fitted polynomial parameters are presented in Table B.10. The quantum number assignment for "A" through "F" are $m_J = -5/2$ through $+5/2$, respectively. The feature marked with an asterisk is a component of the $^RQ_{43}(1)$ line.

3, $J = 5/2$ (F_3) levels of a $^4\Sigma^+$ state are 1.7735, 1.2014 and 0.0572, respectively. Both of the levels of the Hunds *case b* $^4\Sigma^+$ state tune more slowly than the $N = 1$, $J = 5/2$ (F_2) level of the Hunds *case b* $^6\Sigma^+$ state. If it is assumed that as in the case of the $^6\Sigma^+$ ($v = 0$) state [160] the $\Delta N = 2$ interaction dominates, then the sole perturbing level (*i.e.* the $N = 3$, $J = 5/2$ (F_3) level of the a $^4\Sigma^+$ state) tunes approximately 31 times slower than the $N = 1$, $J = 5/2$ (F_2) level of the nominal $^6\Sigma^+$ ($v = 1$) state. The ratio of the observed to expected g_S-factor (=1.721/2.002=0.860) and the Hunds *case b* tuning rate for a $N = 3$, $J = 5/2$ (F_3) level of a $^4\Sigma^+$ state and a $N = 1$, $J = 5/2$ (F_2) level of a $^6\Sigma^+$ state predicts that $N = 1$, $J = 5/2$ (F_2) level of the A$^6\Sigma^+$ ($v = 1$) state is an admixture of approximately 14.5 % (= $100\% \times (1 - 0.860) \times 31/30$) of the $N = 3$, $J = 5/2$ (F_3) level of the a$^4\Sigma^+$ state. The $N = 1$, $J = 7/2$ (F_1) level of the A$^6\Sigma^+$ ($v = 1$) state interacts with the $N = 3$, $J = 7/2$ (F_2) level of the a$^4\Sigma^+$ state, which in the Hunds *case b* limit has a g_J-factor of 0.4767. Thus it is expected that the effective g_S-factor for the $N = 1$, $J = 7/2$ (F_1) level of the A$^6\Sigma^+$ ($v = 1$) state will be larger than that of the $N = 1$, $J = 5/2$ (F_2) level of the $^6\Sigma^+$ ($v = 1$) state, in agreement with the observation.

Feature[a]	$A^6\Sigma^+$-$X^6\Sigma^+$ (0,0)			$A^6\Sigma^+$-$X^6\Sigma^+$ (1,0)		
	a[b]	b	c	a	b	c
	(cm^{-1})	(cm^{-1}/Tesla)	(cm^{-1}/T^2)	(cm^{-1})	(cm^{-1}/T)	(cm^{-1}/T^2)
A	11563.4134	-0.7577	-0.03756	13044.3470	-0.8386	-0.03610
B	11563.4138	-0.4581	-0.06149	13044.3470	-0.5032	-0.06158
C	11563.4132	-0.1535	-0.07226	13044.3470	-0.1682	-0.07595
D	11563.4138	0.1488	-0.08101	13044.3471	0.1665	-0.07720
E	11563.4132	0.4554	-0.07411	13044.3468	0.5035	-0.06878
F	11563.4134	0.7571	-0.04577	13044.3466	0.8406	-0.04586

Table B.10: Second-order polynomial fit of the magnetic tuning of the $R_1(0)$ line.
[a] The six spectral features of Fig. B.9 or the equivalent for the (0,0) band.
[b] Transition wavenumber (cm^{-1})= $a + bB + cB^2$ with B = magnetic field strength in Tesla.

As expected, the proton magnetic hyperfine parameters are two orders of magnitude smaller than that of the free H-atom because the unpaired electrons remain metal centered in both the A$^6\Sigma^+$ and X$^6\Sigma^+$ states. The magnetic hyperfine interaction in the A$^6\Sigma^+$ ($v = 1$) state

does not exhibit the same strong rotational dependence as the Zeeman effect. This suggests that the $A^6\Sigma^+$ and the perturbing $^4\Sigma^+$ state arise from similar molecular orbital configurations. A simple picture for bonding in the low-lying group of excited states [162] is that the Cr atom in the ^5D $(3d^44s^2)$ state approaches the ground state hydrogen atom and a 4s/4p hybrid orbital is formed. The hybrid orbit directed towards the H-atom forms a σ-type bond, whereas the hybrid orbit pointing away from the bond remains singly occupied. In the $A^6\Sigma^+$ state the electron in this back-polarized 4s/4p hybrid orbital is high-spin coupled to four high-spin coupled unpaired electrons in the 3d orbitals. In the $^4\Sigma^+$ state the electron in this back-polarized 4s/4p hybrid orbital is low-spin coupled. The nature of the electron in this back-polarized 4s/4p hybrid orbital has a negligible effect on the electron density in the spatially removed region of the proton and thus the hyperfine interaction in the $A^6\Sigma^+$ and $^4\Sigma^+$ state, or any admixture thereof, will be similar. The Fermi contact parameter, b_F, for the $A^6\Sigma^+$ state is determined to be positive whereas it is negative for the $X^6\Sigma^+$ state [157]. Evidently in the $X^6\Sigma^+$ state, the direct contribution to the spin density at the proton is larger than the spin-polarization effects which contribute with opposite sign [165]. Upon excitation to the $A^6\Sigma^+$ state a portion of the metal centered spin density is shifted away from the Cr-H bond via the occupation of the back-polarized 4s/4p hybrid orbital. This reduces the spin-polarization of the electrons in the σ-type bond resulting in the domination of the direct spin density contribution. A similar change in sign of b_F has been observed in excitation from the $X^7\Sigma^+$ state to the $A^7\Pi$ state of MnH [138].

B.6   Conclusions

A pulsed molecular beam of cold ^{52}CrH has been generated by laser ablation techniques and detected by near natural line width limited laser induced fluorescence spectroscopy. The magnetic tuning of the low-N lines of the $A^6\Sigma^+$-$X^6\Sigma^+$ (0, 0) and (1, 0) bands has been experimentally characterized and modeled using an effective Hamiltonian. The magnetic g-factors for the $A^6\Sigma^+$ $(v = 1)$ state deviate significantly from those expected for an isolated state $^6\Sigma^+$ state. Interaction with the nearly

degenerate $a^4\Sigma^+$ provides a qualitative explanation of the deviation of the g_S-factors and the observed proton magnetic hyperfine interactions. The experimentally determined magnetic tuning characteristics of the $R_1(0)$ branch feature of the $A^6\Sigma^+$-$X^6\Sigma^+$ (1, 0) band system is found to be ideal for monitoring CrH molecules in the buffer gas cooling and magnetic trapping experiments.

Bibliography

[1] M.H. Anderson, J.R. Ensher, M.R. Matthews, C.E. Wieman and E.A. Cornell, *Science* **269**, 198 (1995).

[2] K.B. Davis, M.O. Mewes, M.R. Andrews, N.J. van Druten, D.S. Durfee, D.M. Kurn and W. Ketterle, *Phys. Rev. Lett.* **75**, 3969 (1995).

[3] C.C. Bradley, C.A. Sackett, J.J. Tollett and R.G. Hulet, *Phys. Rev. Lett.* **75**, 1687 (1995).

[4] B. DeMarco and D.S. Jin, *Science* **285**, 1703 (1999).

[5] M.O. Mewes, M.R. Andrews, D.M. Kurn, D.S. Durfee, C.G. Townsend and W. Ketterle, *Phys. Rev. Lett.* **78**, 582 (1997).

[6] B.P. Anderson and M.A. Kasevich, *Science* **282**, 1686 (1998).

[7] I. Bloch, T.W. Hänsch and T. Esslinger, *Phys. Rev. Lett.* **82**, 3008 (1999).

[8] E.W. Hagley, L. Deng, M. Kozuma, J. Wen, K. Helmerson, S.L. Rolston and W.D. Phillips, *Science* **283**, 1706 (1999).

[9] H.L. Bethlem and G. Meijer, *Int. Rev. Phys. Chem.* **22**, 73 (2003).

[10] R.V. Krems, *Int. Rev. Phys. Chem.* **24**, 99 (2005).

[11] Special Issue "Ultracold Polar Molecules", *Eur. Phys. J. D* **31**, 149 (2004).

[12] L.R. Hunter, *Science* **252**, 73 (1991).

[13] M.G. Kozlov and A. Derevianko, *Phys. Rev. Lett.* **97**, 063001 (2006).

[14] J.J. Hudson, B.E. Sauer, M.R. Tarbutt and E.A. Hinds, *Phys. Rev. Lett.* **89**, 023003 (2002).

[15] D. Kawall, F. Bay, S. Bickman, Y. Jiang and D. DeMille, *Phys. Rev. Lett.* **92**, 133007 (2004).

[16] M. de Angelis, G. Gagliardi, L. Gianfrani and G.M. Tino, *Phys. Rev. Lett.* **76**, 2840 (1996).

[17] V.V. Flambaum and M.G. Kozlov, *Phys. Rev. Lett.* **98**, 240801 (2007).

[18] M.G. Kozlov and L.N. Labzowsky, *J. Phys. B* **28**, 1933 (1995).

[19] S.Y.T. van de Meerakker, N. Vanhaecke, M.P.J. van der Loo, G.C. Groenenboom and G. Meijer, *Phys. Rev. Lett.* **95**, 013003 (2005).

[20] W.C. Campbell, G.C. Groenenboom, H.I. Lu, E. Tsikata and J.M. Doyle, *Phys. Rev. Lett.* **100**, 083003 (2008).

[21] M. Greiner, C.A. Regal and D.S. Jin, *Nature* **426**, 537 (2003).

[22] S. Jochim, M. Bartenstein, A. Altmeyer, G. Hendl, S. Riedl, C. Chin, J. Hecker Denschlag and R. Grimm, *Science* **302**, 2101 (2003).

[23] M.W. Zwierlein, C.A. Stan, C.H. Schunck, S.M.F. Raupach, S. Gupta, Z. Hadzibabic and W. Ketterle, *Phys. Rev. Lett.* **91**, 250401 (2003).

[24] T. Lahaye, T. Koch, B. Fröhlich, M. Fattori, J. Metz, A. Griesmaier, S. Giovanazzi and T. Pfau, *Nature* **448**, 672 (2007).

[25] T. Koch, T. Lahaye, J. Metz, B. Fröhlich, A. Griesmayer and T. Pfau, *Nature Phys.* **4**, 218 (2008).

[26] N. Balakrishnan and A. Dalgarno, *J. Chem. Phys.* **113**, 621 (2000).

[27] J.J. Gilijamse, S. Hoekstra, S.Y.T. van de Meerakker, G.C. Groeneboom and G. Meijer, *Science* **313**, 1617 (2006).

[28] D. Herschbach, *Rev. Mod. Phys.* **71**, S411 (1999).

[29] N. Balakrishnan and A. Dalgarno, *Chem. Phys. Lett.* **341**, 652 (2001).

[30] A. André, D. DeMille, J.M. Doyle, M.D. Lukin, S.E. Maxwell, P. Rabl, R.J. Schoelkopf and P. Zoller, *Nature Phys.* **2**, 636 (2006).

[31] D. DeMille, *Phys. Rev. Lett.* **88**, 067901 (2002).

[32] P. Rabl, D. DeMille, J.M. Doyle, M.D. Lukin, R.J. Schoelkopf and P. Zoller, *Phys. Rev. Lett.* **97**, 033003 (2006).

[33] A. Fioretti, D. Comparat, A. Crubellier, O. Dulieu, F. Masnou-Seeuws and P. Pillet, *Phys. Rev. Lett.* **80**, 4402 (1998).

[34] C. Gabbanini, A. Fioretti, A. Lucchesini, S. Gozzini and M. Mazzoni, *Phys. Rev. Lett.* **84**, 2814 (2000).

[35] A. Kerman, J. Sage, S. Sainis, T. Bergeman and D. DeMille, *Phys. Rev. Lett.* **92**, 153001 (2004).

[36] C. Haimberger, J. Kleinert, M. Bhattacharya and N.P. Bigelow, *Phys. Rev. A* **70**, 021402 (2004).

[37] M. Mancini, G. Telles, A. Caires, V. Bagnato and L. Marcassa, *Phys. Rev. Lett.* **92**, 133203 (2004).

[38] D. Wang, J. Qi, M. Stone, O. Nikolayeva, B. Hattaway, S. Gensemer, H. Wang, W. Zemke, P. Gould, E. Eyler and W. Stwalley, *Eur. Phys. J. D* **31**, 165 (2004).

[39] S. Kraft, P. Staanum, J. Lange, L. Vogel, R. Wester and M. Weidemüller, *J. Phys. B* **39**, 993 (2006).

[40] J.M. Sage, S. Sainis, T. Bergeman and D. DeMille, *Phys. Rev. Lett.* **94**, 203001 (2005).

[41] H.L. Bethlem, G. Berden and G. Meijer, *Phys. Rev. Lett.* **83**, 1558 (1999).

[42] H.L. Bethlem, G. Berden, F.M.H. Crompvoets, R.T. Jongma, A.J.A. van Roij and G. Meijer, *Nature* **406**, 491 (2000).

[43] H.L. Bethlem, F.M.H. Crompvoets, R.T. Jongma, S.Y.T. van de Meerakker and G. Meijer, *Phys. Rev. A* **65**, 053416 (2002).

[44] J.R. Bochinski, E.R. Hudson, H.J. Lewandowski, G. Meijer and J. Ye, *Phys. Rev. Lett.* **91**, 243001 (2003).

[45] S.Y.T. van de Meerakker, P.H.M. Smeets, N. Vanhaecke, R.T. Jongma and G. Meijer, *Phys. Rev. Lett.* **94**, 023004 (2005).

[46] E.R. Hudson, C. Ticknor, B.C. Sawyer, C.A. Taatjes, H.J. Lewandowski, J.R. Bochinski, J.L. Bohn and J. Ye, *Phys. Rev. A* **73**, 063404 (2006).

[47] S. Hoekstra, M. Metsälä, P.C. Zieger, L. Scharfenberg, J.J. Gilijamse, G. Meijer and S.Y.T. van de Meerakker, *Phys. Rev. A* **76**, 063408 (2007).

[48] S. Jung, E. Tiemann and C. Lisdat, *Phys. Rev. A* **74**, 040701 (2006).

[49] F.M.H. Crompvoets, H.L. Bethlem, R.T. Jongma and G. Meijer, *Nature* **411**, 174 (2001).

[50] F.M.H. Crompvoets, H.L. Bethlem, J. Küpper, A.J.A. van Roij and G. Meijer, *Phys. Rev. A* **69**, 063406 (2004).

[51] C.E. Heiner, D. Carty, G. Meijer and B.H. L., *Nature Phys.* **3**, 115 (2007).

[52] H.L. Bethlem, A.J.A. van Roij, R.T. Jongma and G. Meijer, *Phys. Rev. Lett.* **88**, 133003 (2002).

[53] K. Wohlfart, F. Filsinger, F. Grätz, H. Haak, J. Küpper and G. Meijer. *Decoupling of longitudinal and transverse motion in the Stark decelerator using alternating gradient focusing.* In preparation.

[54] M.R. Tarbutt, H.L. Bethlem, J.J. Hudson, V.L. Ryabov, V.A. Ryzhov, B.E. Sauer, G. Meijer and E.A. Hinds, *Phys. Rev. Lett.* **92**, 173002 (2004).

[55] K. Wohlfart, F. Grätz, F. Filsinger, H. Haak, G. Meijer and J. Küpper, *Phys. Rev. A* **77** (2008).

[56] S.A. Rangwala, T. Junglen, T. Rieger, P.W.H. Pinkse and G. Rempe, *Phys. Rev. A* **67**, 043406 (2003).

[57] T. Junglen, T. Rieger, P.W.H. Pinkse and G. Rempe, *Phys. Rev. Lett.* **92**, 223001 (2004).

[58] J.D. Weinstein, R. deCarvalho, T. Guillet, B. Friedrich and J.M. Doyle, *Nature* **395**, 148 (1998).

[59] J.J. Gilijamse, S. Hoekstra, S. Meek, M. Metsälä, S.Y.T. van de Meerakker, G.C. Groeneboom and G. Meijer, *J. Chem. Phys.* **127**, 221102 (2007).

[60] J.D. Weinstein, R. deCarvalho, J. Kim, D. Patterson, B. Friedrich and J.M. Doyle, *Phys. Rev. A* **57**, R3173 (1998).

[61] J. Kim, B. Friedrich, D.P. Katz, D. Patterson, J.D. Weinstein, R. deCarvalho and J.M. Doyle, *Phys. Rev. Lett.* **78**, 3665 (1997).

[62] C.I. Hancox, M.T. Hummon, S.V. Nguyen and J.M. Doyle, *Phys. Rev. A* **71**, 031402 (2005).

[63] C.I. Hancox, S.C. Doret, M.T. Hummon, L.J. Luo and J.M. Doyle, *Nature* **431**, 281 (2004).

[64] B.C. Sawyer, B.L. Lev, E.R. Hudson, B.K. Stuhl, M. Lara, J.L. Bohn and J. Ye, *Phys. Rev. Lett.* **98**, 253002 (2007).

[65] W.H. Wing, *Prog. Quant. Electr.* **8**, 181 (1984).

[66] W. Ketterle and D.E. Pritchard, *Appl. Phys. B* **54**, 403 (1992).

[67] S. Chu, J.E. Bjorkholm, A. Ashkin and A. Cable, *Phys. Rev. Lett.* **57**, 314 (1986).

[68] R. Grimm, M. Weidemüller and Y. Ovchinnikov, *Adv. Atom. Mol. Opt. Phys.* **42**, 95 (1999).

[69] T. Takekoshi, B.M. Patterson and R.J. Knize, *Phys. Rev. Lett.* **81**, 5105 (1998).

[70] R.J.C. Spreeuw, C. Gerz, L.S. Goldner, W.D. Phillips, S.L. Rolston, C.I. Westbrook, M.W. Reynolds and I.F. Silvera, *Phys. Rev. Lett.* **72**, 3162 (1994).

[71] D. DeMille, D.R. Glenn and J. Petricka, *Eur. Phys. J. D* **31**, 375 (2004).

[72] J. van Veldhoven, H.L. Bethlem and G. Meijer, *Phys. Rev. Lett.* **94**, 083001 (2005).

[73] M. Schnell, P. Lützow, J. van Veldhoven, H.L. Bethlem, J. Küpper, B. Friedrich, M. Schleier-Smith, H. Haak and G. Meijer, *J. Phys. Chem. A* **111**, 7411 (2007).

[74] H.L. Bethlem, J. van Veldhoven, M. Schnell and G. Meijer, *Phys. Rev. A* **74**, 063403 (2006).

[75] S. Schlunk, A. Marian, P. Geng, A. Mosk, G. Meijer and W. Schöllkopf, *Phys. Rev. Lett.* **98**, 223002 (2007).

[76] T. Kishimoto, H. Hachisu, J. Fujiki, K. Nagato, M. Yasuda and H. Katori, *Phys. Rev. Lett.* **96**, 123001 (2006).

[77] J.M. Doyle, B. Friedrich, J. Kim and D. Patterson, *Phys. Rev. A* **52**, R2515 (1995).

[78] J.D. Weinstein, R. deCarvalho, C.I. Hancox and J.M. Doyle, *Phys. Rev. A* **65**, 021604 (2002).

[79] S.V. Scott V. Nguyen, S.C. Doret, C.B. Connolly, R.A. Michniak, W. Ketterle and J.M. Doyle, *Phys. Rev. A* **72**, 060703 (2005).

[80] W.C. Campbell, E. Tsikata, H.I. Lu, L.D. van Buuren and J.M. Doyle, *Phys. Rev. Lett.* **98**, 213001 (2007).

[81] J.D. Weinstein, R. deCarvalho, K. Amar, A. Boca, B.C. Odom, B. Friedrich and J.M. Doyle, *J. Chem. Phys.* **109**, 2656 (1998).

[82] J.G.E. Harris, R.A. Michniak, S.V. Nguyen, N. Brahms, W. Ketterle and J.M. Doyle, *Europhys. Lett.* **67**, 198 (2004).

[83] R.V. Krems, D. Egorov, J.S. Helton, K. Maussang, S.V. Nguyen and J.M. Doyle, *J. Chem. Phys.* **121**, 11639 (2004).

[84] R.V. Krems and A. Dalgarno, *J. Chem. Phys.* **120**, 2296 (2004).

[85] R.V. Krems, H.R. Sadeghpour, A. Dalgarno, D. Zgid, J. Klos and G. Chalasinski, *Phys. Rev. A* **68**, 051401 (2003).

[86] T. Mayer-Kuckuck: *Atomphysik*. Teubner Studienbcher, 1985.

[87] W. Demtröder: *Molecular Physics*. John Wiley & Sons, 2004.

[88] T.G. Walker and W. Happer, *Rev. Mod. Phys.* **69**, 629 (1997).

[89] J.D. Weinstein: *Magnetic Trapping of Atomic Chromium and Molecular Calcium Monohydride*. Cambridge, MA, United States, Harvard University, Dissertation, 2001.

[90] W. Ketterle and N.J. van Druten, *Adv. Atom. Mol. Opt. Phys.* **37**, 181 (1996).

[91] E. Tiesinga, S.J.M. Kuppens, B.J. Verhaar and H.T.C. Stoof, *Phys. Rev. A* **43**, 5188 (1991).

[92] J.G.E. Harris, R.A. Michniak, S.V. Nguyen, N. Brahms, W. Ketterle and J.M. Doyle, *Phys. Rev. Lett.* **99**, 223201 (2007).

[93] P.J. Leo, E. Tiesinga, P.S. Julienne, D.K. Walter and S. Kadlecek, *Phys. Rev. Lett.* **81**, 13891392 (1998).

[94] F.H. Mies, C.J. Williams, P.S. Julienne and M. Krauss., *Journal of Research of the National Institute of Standards and Technology* **101**, 521535 (1996).

[95] R.V. Krems, G.C. Groenenboom and A. Dalgarno, *J. Phys. Chem. A* **108**, 8941 (2004).

[96] C.I. Hancox, S.C. Doret, M.T. Hummon, R.V. Krems and J.M. Doyle, *Phys. Rev. Lett.* **94**, 013201 (2005).

[97] K. Maussang, D. Egorov, J.S. Helton, S.V. Nguyen and J.M. Doyle, *Phys. Rev. Lett.* **94**, 123002 (2005).

[98] H. Cybulski, R.V. Krems, H.R. Sadeghpour, A. Dalgarno, J. Klos, G.C. Groenenboom, A. van der Avoird, D. Zgid and G. Chalasinski, *J. Chem. Phys.* **122**, 094307 (2005).

[99] B. Friedrich, R. deCarvalho, J. Kim, D. Patterson, J.D. Weinstein and J.M. Doyle, *J. Chem. Soc. – Faraday Trans.* **94**, 1783 (1998).

[100] F. Pobell, Ed. *Matter and Methods at Low Temperatures.* Springer, Berlin Heidelberg New York, 1995.

[101] D. Egorov, W.C. Campbell, B. Friedrich, S.E. Maxwell, E. Tsikata, L.D. van Buuren and J.M. Doyle, *Eur. Phys. J. D* **31**, 307 (2004).

[102] D.R. Willey, R.L. Crownover, D.N. Bittner and F.C. DeLucia, *J. Chem. Phys.* **89**, 1923 (1988).

[103] D.R. Willey, D.N. Bittner and F.C. DeLucia, *Mol. Phys.* **67**, 455 (1989).

[104] C.D. Ball and F.C. DeLucia, *Phys. Rev. Lett.* **81**, 305 (1998).

[105] T.J. Ronningen and F.C. DeLucia, *J. Chem. Phys.* **122**, 184319 (2005).

[106] D. DeMille. *Cold beam of SrO for trapping studies.* In preparation.

[107] J. Kim: *Buffer-gas Loading and Magnetic Trapping of Atomic Europium.* Boston, Harvard University, Dissertation, 1997.

[108] R. deCarvalho, J.M. Doyle, B. Friedrich, T. Guillet, J. Kim, D. Patterson and J.D. Weinstein, **7**, 289 (1999).

[109] J.J. Sakurai: *Modern Quantum Mechanics.* Addison-Wesley, 1993.

[110] W. Petrich, M.H. Anderson, J.R. Ensher and E.A. Cornell, *Phys. Rev. Lett.* **74**, 3352 (1995).

[111] T. Bergeman, G. Erez and H.J. Metcalf, *Phys. Rev. A* **35**, 1535 (1987).

[112] M.O. Mewes, M.R. Andrews, N.J. van Druten, D.M. Kurn, D.S. Durfee and W. Ketterle, *Phys. Rev. Lett.* **77**, 416 (1996).

[113] I. Esslinger, I. Bloch and T. Hänsch, *Phys. Rev. A* **58**, R2667 (1998).

[114] R.C. Dunbar, *J. Chem. Phys.* **95**, 2537 (1991).

[115] D. Tholmann, D.S. Tonner and T.B. McMahon, *J. Phys. Chem.* **98**, 2002 (1994).

[116] S. Hoekstra, J.J. Gilijamse, B. Sartakov, N. Vanhaecke, L. Scharfenberg, S.Y.T. van de Meerakker and G. Meijer, *Phys. Rev. Lett.* **98**, 133001 (2007).

[117] L.A. Kaledin, M.G. Erickson and M.C. Heaven, *J. Mol. Spec.* **165**, 323 (1994).

[118] I.E. Gordon, D.R.T. Appadoo, A. Shayesteh, K.A. Walker and P.F. Bernath, *J. Mol. Spec.* **229**, 145 (2005).

[119] P.M. Sheridan and L.M. Ziurys, *Chem. Phys. Lett.* **380**, 632 (2003).

[120] D.T. Halfen and L.M. Ziurys, *J. Chem. Phys.* **122**, 054309 (2005).

[121] S.M. Corkery, J.M. Brown, S.P. Beaton and K.M. Evenson, *J. Mol. Spec.* **149**, 257 (1991).

[122] K. Namiki and S. Saito, *J. Chem. Phys.* **107**, 8848 (1997).

[123] K. Katoh, T. Okabayashi, M. Tanimoto, Y. Sumiyoshi and Y. Endo, *J. Chem. Phys.* **120**, 7927 (2004).

[124] J.M. Thompsen, M.A. Brewster and L.M. Ziurys, *J. Chem. Phys.* **116**, 10212 (2002).

[125] P.M. Sheridan, M.A. Brewster and L.M. Ziurys, *Astrophys. J.* **576**, 1108 (2002).

[126] A.S.C. Cheung, R.C. Hansen and A.J. Merer, *J. Mol. Spec.* **91**, 165 (1982).

[127] A.G. Adam, Y. Azuma, J.A. Barry, A.J. Merer, U. Sassenberg, J.O. Schroder, G. Cheval and J.L. Femenias, *J. Chem. Phys.* **100**, 6240 (1994).

[128] O. Launila and B. Lindgren, *J. Chem. Phys.* **104**, 6418 (1996).

[129] C.R. Brazier, R.S. Ram and P.F. Bernath, *J. Mol. Spec.* **120**, 381 (1986).

[130] G. Berden, R. Engeln, P.C.M. Christianen, J.C. Maan and G. Meijer, *Phys. Rev. A* **58**, 3114 (1998).

[131] W.L. Barclay, M.A. Anderson and L.M. Ziurys, *Astrophys. J.* **408**, L65 (1993).

[132] A.G. Gaydon and R.W.B. Pearse, *Nature* **140**, 110 (1937).

[133] R.W.B. Pearse and A.G. Gaydon, *Proc. Phys. Soc.* **50**, 201 (1938).

[134] J.D. Kirkpatrick, I.N. Reid, J. Liebert, R.M. Cutri, B. Nelson, C.A. Beichman, C.C. Dahn, D.G. Monet, J.E. Gizis and M.F. Skrutskie, *Astrophys. J.* **519**, 802 (1999).

[135] O. Engvold, H. Wöhl and J. Brault, *Astron.Astrophys.Suppl.Series* **42**, 209 (1980).

[136] T.D. Varberg, R.W. Field and A.J. Merer, *J. Chem. Phys.* **92**, 7123 (1990).

[137] T.D. Varberg, R.W. Field and A.J. Merer, *J. Chem. Phys.* **95**, 1563 (1991).

[138] T.D. Varberg, J.A. Gray, R.W. Field and A.J. Merer, *J. Mol. Spec.* **156**, 296 (1992).

[139] R.J. Vanzee, D.A. Garland and W. Weltner, *J. Chem. Phys.* **84**, 5968 (1986).

[140] R.J. Vanzee, D.A. Garland and W. Weltner, *J. Chem. Phys.* **85**, 3237 (1986).

[141] R. deCarvalho, J.M. Doyle, B. Friedrich, T. Guillet, J. Kim, D. Patterson and J.D. Weinstein, *Eur. Phys. J. D* **7**, 289 (1999).

[142] D. Weise: *Preparation and Highly Sensitive Detection of Ultracold Molecules.* Konstanz, Germany, Universität Konstanz, Dissertation, 2004.

[143] J.G.E. Harris, S.V. Nguyen, S.C. Doret, W. Ketterle and J.M. Doyle, *Rev. Sci. Instrum.* **75**, 17 (2004).

[144] R.W.P. Drever, J.L. Hall, F.V. Kowalski, J. Hough, G.M. Ford, A.J. Munley and H. Ward, *Appl. Phys. B* **31**, 97 (1983).

[145] O.J. Luiten, M.W. Reynolds and J.T.M. Walraven, *Phys. Rev. A* **53**, 381 (1996).

[146] R. deCarvalho, C.I. Hancox and J.M. Doyle, *J. Opt. Soc. Am. B* **20**, 1131 (2003).

[147] F. Reif: *Fundamentals of statistical and thermal physics.* International. edition. McGraw-Hill, Singapore, 1985.

[148] W.H. Press, B.P. Flannery, S.A. Teukolsky and W.T. Vetterling: *Numerical Recipes in C, second edition.* The International Series of Monographs on Physics. Cambridge University Press, 1992.

[149] S.T. Thornton and J.B. Marion: *Classical Dynamics of Particles and Systems.* Brooks/Cole-Thomson Learning, 10 Davis Drive, Belmont, CA 94002, 2004.

[150] N. Balakrishnan, G.C. Groenenboom, R.V. Krems and A. Dalgarno, *J. Chem. Phys.* **118**, 7386 (2003).

[151] S.Y.T. van de Meerakker, R.T. Jongma, H.L. Bethlem and G. Meijer, *Phys. Rev. A* **64**, 041401(R) (2001).

[152] *Gmelins Handbuch der anorganischen Chemie - Cr-Teil B.* Verlag Chemie, Weinheim, 1966.

[153] J. Chen, J.M. Bakker, A. Peters, M. Stoll, G. Meijer and T.C. Steimle, *Phys. Chem. Chem. Phys.,* **9**, 949 (2007).

[154] T.C. Steimle, H. Wang, J. Gengler, M. Stoll and G. Meijer, *J. Chem. Phys. The Zeeman effect in the (0,0) band of the $A^7\Pi$ - $X^7\Sigma^+$ transition of Manganese Monohydride, MnH*, submitted.

[155] J.B. Hasted: *Physics of Atomic Collisions.* American Elsevier, 1972.

[156] C.J. Foot: *Atomic Physics.* Oxford Master Series in Atomic, Optical and Laser Physics. Oxford University Press, 2005.

[157] J.J. Harrison, J.M. Brown, D.T. Halfen and L.M. Ziurys, *Astrophys. J.* **637**, 1143 (2006).

[158] A. Burrows, R.S. Ram, P. Bernath, C.M. Sharp and J.A. Milsom, *Astrophys. J.* **577**, 986 (2002).

[159] P.K. Chowdhurya, A.J. Merer, S.J. Rixon, P.F. Bernath and R.S. Ram, *Phys. Chem. Chem. Phys.* **8** (2006).

[160] R.S. Ram, C.N. Jarman and P.F. Bernath, *J. Mol. Spec.* **161**, 445 (1993).

[161] D.G. Dai and K. Balasubramanian, *J. Mol. Spec.* **161**, 455 (1993).

[162] C.W. Bauschlicher, R.S. Ram, P.F. Bernath, C.G. Parsons and D. Galehouse, *J. Chem. Phys.* **115**, 1312 (2001).

[163] G. Ghigo, B.O. Roos, P.C. Stancil and P.F. Weck, *J. Chem. Phys.* **121**, 8194 (2004).

[164] J. Chen, J. Gengler, T.C. Steimle and J.M. Brown, *Phys. Rev. A* **73**, 012502 (2006).

[165] W. Weltner, Ed. *Magnetic Atoms and Molecules.* Dover Publications, 1983.

[166] J.M. Brown and A. Carrington: *Rotational Spectroscopy of Diatomic Molecules.* Oxford University Press, 2003.

Lebenslauf

Michael Stoll, geboren am 26.12.1974
in Weiden i.d.Opf., Bayern, Deutschland

1994   Abitur am Keppler-Gymnasium in Weiden

1994 - 1995 Zivildienst
Betreuung körperlich schwerstbehinderter Studenten
in Regensburg

1996 - 1997 Studium der Rechtswissenschaften an der
Friedrich-Alexander Universität, Erlangen-Nürnberg

1997 - 2004 Physikstudium an der Technischen Universität, Berlin

2002 - 2003 Diplomarbeit am Institut für Festkörperphysik
bei Prof. Dr. Christian Thomsen mit dem Titel:
"Raman Spektroskopie an elektrochemisch dotierten
Kohlenstoff-Nanotubes"

2004 - 2008 Doktorarbeit in der Abteilung für Molekülphysik am
Fritz-Haber-Institut der Max-Planck Gesellschaft.
Das Projekt ist eine Kollaboration der Arbeitsgruppe
von Prof. Dr. Gerard Meijer (FHI)
und Prof. Dr. Achim Peters
von der Humboldt-Universität, Berlin

Publications

- Michael Stoll, Peter Rafailov and Christian Thomsen, *"Electrochemical and Raman Measurements on Single-Walled Carbon Nanotubes"*, *Chem. Phys. Lett.* **375**, 625-631 (2003)

- Peter Rafailov, Michael Stoll, and Christian Thomsen, *"Strain Determination in Electrochemically Doped Single-Walled Carbon Nanotubes via Raman Spectroscopy"*, *J. Phys. Chem. B* **108**, 19241-19245 (2004)

- Joost M. Bakker, Michael Stoll, Dennis R. Weise, Oliver Vogelsang, Gerard Meijer and Achim Peters, *"Magnetic trapping of buffer-gas-cooled chromium atoms and prospects for the extension to paramagnetic molecules"*, *J. Phys. B: At. Mol. Opt. Phys.* **39**, S1111-S1123 (2006)

- Jinhai Chen, Joost M. Bakker, Achim Peters, Michael Stoll, Gerard Meijer and Timothy C. Steimle, *"The Zeeman tuning of the $A^6\Sigma^+$-$X^6\Sigma^+$ transition of chromium monohydride"*, *Phys. Chem. Chem. Phys.* **9**, 949 - 957 (2007)

- Michael Stoll, Joost M. Bakker, Tim Steimle, Gerard Meijer and Achim Peters *"Cryogenic buffer-gas loading and magnetic trapping of CrH and MnH molecules"*, *Phys. Rev. A* **9**, 78, 032707 (2008)

- Timothy C. Steimle, H. Wang, Jamie Gengler, Michael Stoll and Gerard Meijer, *"The Zeeman effect in the (0,0) band of the $A^7\Pi$ - $X^7\Sigma^+$ transition of Manganese Monohydride, MnH"*, *J. Chem. Phys.*, *submitted*